# Functional photoreceptors regulating light-switchable adhesion of *Chlamydomonas* to surfaces

**Dissertation**
zur Erlangung des mathematisch-naturwissenschaftlichen
Doktorgrades
"Doctor rerum naturalium"
der
Georg-August-Universität Göttingen

im Promotionsprogramm Physics of Biological and Complex Systems
(PBCS)
der Georg-August University School of Science (GAUSS)

vorgelegt vom
**Rodrigo Esteban Catalán López**
aus Providencia, Santiago de Chile

Göttingen, June 2023

## Betreuungsausschuss

**Prof. Dr. Oliver Bäumchen**,
Research Group "Dynamics of Fluids and Biological Interfaces",
Department "Dynamics of Complex Fluids",
Max Planck Institute for Dynamics and Self-Organization
Lehrstuhl für Experimentalphysik V, Universität Bayreuth.

**Prof. Dr. Jörg Enderlein**,
Research Group "Single Molecule Spectroscopy and Imaging for Biophysics and Complex Systems",
Drittes Physikalisches Institut,
Georg-August-Universtiät Göttingen.

**Prof. Dr. Marcus Müller**,
Research Group "Computational Soft Matter and Biophysics"
Institut für Theoretische Physik,
Georg-August-Universtiät Göttingen.

## Mitglieder der Prüfungskommission

**Prof. Dr. Oliver Bäumchen (Referee)**,
Research Group "Dynamics of Fluids and Biological Interfaces",
Department "Dynamics of Complex Fluids",
Max Planck Institute for Dynamics and Self-Organization
Lehrstuhl für Experimentalphysik V, Universität Bayreuth.

**Prof. Dr. Jörg Enderlein (Referee)**,
Research Group "Single Molecule Spectroscopy and Imaging for Biophysics and Complex Systems",
Drittes Physikalisches Institut,
Georg-August-Universtiät Göttingen.

# Weitere Mitglieder des Prüfungsausschuss

**Prof. Dr. Marcus Müller**,
Research Group "Computational Soft Matter and Biophysics"
Institut für Theoretische Physik,
Georg-August-Universtiät Göttingen.

**Prof. Dr. Timo Betz**,
Research Group "BetzLab"
Drittes Physikalisches Institut,
Georg-August-Universtiät Göttingen.

**Prof. Dr. Stefan Klumpp**,
Research Group "Theoretische Biophysik"
Institut für Dynamik komplexer Systeme,
Georg-August-Universtiät Göttingen.

**Dr. David Zwicker**,
Research Group "Theory of biological fluids"
Max-Planck-Institut für Dynamik und Selbstorganisation,
Göttingen.

**Tag der mündlichen Prüfung: September 14$^{\text{th}}$ 2023**

# Abstract

The harnessing of light is one of the most remarkable evolutionary features of microalgae, allowing them to adapt and thrive in highly dynamic environments. In order to respond to environmental changes, these photoactive microorganisms have developed an intricate network of light-sensitive molecules, known as photoreceptors, that enables the cells to locate optimal areas for growth and photosynthetic performance. Under favorable conditions, microalgae colonize surfaces and form biofilms, which have substantial technological and medical implications. Notably, the adhesion of microalgae to surfaces can be triggered by light. However, the underlying mechanisms controlling the adhesion response to a light stimulus remain poorly understood. This thesis aims to identify the photoreceptor mediating light-switchable flagellar adhesion of the microalga *Chlamydomonas reinhardtii* to surfaces.

Using wild-type and genetically modified strains, I investigated the surface colonization kinetics of a population of motile *Chlamydomonas* cells in response to light. Complementary single-cell micropipette force spectroscopy measurements were conducted to quantify the flagellar adhesion forces. Using a time-delayed Langmuir-type kinetics model, I found that cell adsorption occurs significantly faster than desorption for all the strains exhibiting the phenotype. This difference is attributed to the protein-mediated adhesion mechanism of the cells. Furthermore, the adsorption kinetics are not affected by phototactic responses or by the disruption of most of the photoreceptors studied. Micropipette force measurements revealed similar adhesion forces between wild-type and mutant cells, allowing to rule out the most prominent photoreceptors: channelrhodopsins and phototropin.

Further characterization of the action spectrum of flagellar adhesion forces suggests that the photoreceptor mediating adhesion contains a flavin-based chromophore, which motivated the deletion of cryptochrome photoreceptors. Adsorption and force spectroscopy experiments showed that the deletion of both plant- and animal-cryptochromes is necessary to completely disrupt the adhesion phenotype of the wild-type strain. Interestingly, cryptochromes are known to be located in the nucleus of *Chlamydomonas* cells, where they function as transcription factors. I found that the time scale associated to light-switchable flagellar adhesion is about 15 s, which is significantly faster than that of gene transcription. This suggests that a so-far-unconsidered flavin-based photoreceptor exists in the flagella of *Chlamydomonas* and is the one directly mediating the switching of the adhesion, while the cryptochromes regulate the transcription of the unknown photoreceptor.

# Contents

# List of Figures

# List of Tables

# Chapter 1

# Introduction

## 1.1 Motivation

Uninviting, hostile, and hellish. That is how the Earth would certainly look like if we could travel back around 4.2 billion years to the dawn of what we now would dare to call *home*. Back then, the Earth was perhaps not too different from many of the giant rocks scattered around in the nascent Solar System, constantly blasted by other pieces of tinier rocks, in its course to become a planet.

The early cataclysm was a blessing in disguise. Countless fireballs bombarding here and there, followed by calmer days of obscurity and longstanding rains, laid the chemical groundwork for the emergence of the first forms of life around 3 billion years ago. These primitive inhabitants developed the early mechanisms that allowed them to find areas of higher nutrient content, where they could thrive and boost their chances to survive in the murky oceans of an Earth in half-light.

Later on, the skies progressively cleared and a solitary continental platform was caressed by the first beams of sunlight. After the perennial darkness came light and, with it, the evolution of some of the primitive organisms into a new type of living creature, which managed to harness light as their main source to accomplish practically every single task of their life. Their internal machinery, predominantly controlled by complex light-sensitive proteins, known as photoreceptors, provided these microorganisms with a sense of time and orientation, which, consequently, established a continuous exchange of information with their surroundings. Such forms of life have remarkably populated almost every wrinkle on the face of the Earth, and are referred to as photoactive microbes. One of the most relevant exemplars of such organisms are microalgae.

## 1.2 Microalgae: ecological and technological relevance

The term *algae* refers to a diverse group of photosynthetic, eukaryotic organisms, with fundamental relevance to sustaining life on Earth. They comprise species of unicellular microbes and also multicellular organisms that include simple colonies containing thousands of cells and the more familiar macroscopic algae. Macroalgae can grow to sizes of tens of meters and are commonly seen as seaweed and kelp in coastal regions.

Unlike macroscopic algae, which are found to a great extent in marine environments, unicellular microalgae can thrive in habitats scattered all over the world. They are abundant in rivers, lakes, and practically in all moist ecosystems of the terrestrial landscape that are exposed to light. Microalgae can even be found in all kinds of more extreme environments, such as in snow, sea ice, hot springs, and salt lakes; demonstrating their outstanding survival skills and a remarkable adaptation capacity that has enabled their existence for hundreds of millions of years [1].

Microalgae and cyanobacteria, a more ancient prokaryotic form of photosynthetic organisms, are classified as *phytoplankton*, and are considered primary producers of biomass. By transforming sunlight and carbon dioxide into organic compounds and oxygen via photosynthesis, microalgae sustain more complex forms of life. Photosynthetic microbes are responsible for nearly half of the annual primary production of organic matter on our planet, even though they account for only 0.2% of the Earth's photosynthetic biomass [2, 3]. The annual biomass output of all kinds of photosynthetic organisms on Earth provides a total of 104.9 gigatons of carbon, where 53.8% is contributed by terrestrial plants and 46.2% is provided by oceanic phytoplankton [3]. The astonishing biomass output provided by phytoplankton comes from a turnover rate that is more than 3 orders of magnitude faster for microalgae (2-6 days) than for terrestrial plants (average of 19 years) [3]. Consequently, microalgae play a vital role in nutrient cycling worldwide, as they serve as a nutritional source to other higher organisms [4]. Furthermore, they are also relevant in the transport of atmospheric carbon dioxide to the bottom of the ocean, making them an important factor in the control of $CO_2$ levels and climate change [4]. In addition to this, the quick output of biomass produced by microalgae makes them a highly valuable resource for the production of sustainable energy and other added-value compounds with a direct impact on human society. For instance, microalgae are cultivated in photobioreactors to produce alternative fuels [5], biopharmaceuticals [6], and nutritional supplements [7].

Despite the positive aspects that microalgae bring to the ecology of the planet, they can also be a source of threat in natural and even artificial settings. For example, in open water systems, such as lakes and oceans, an overabundance of nitrogen,

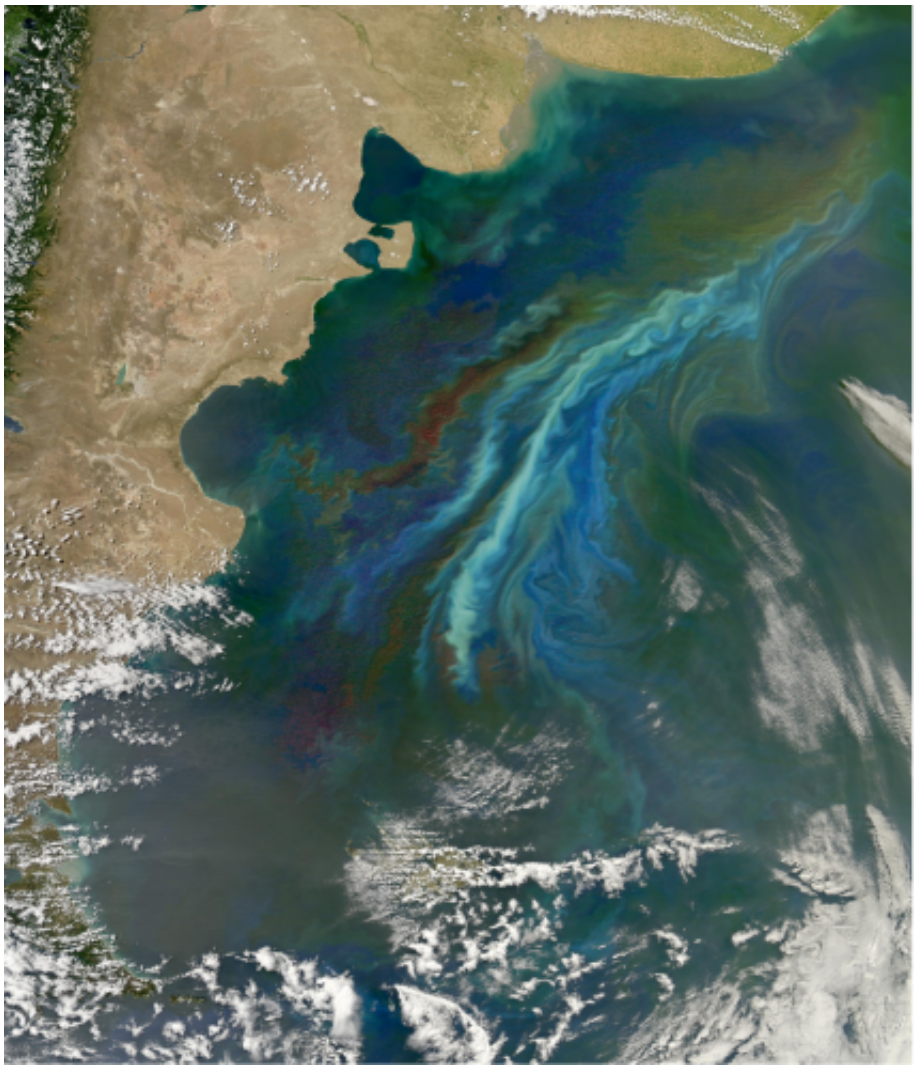

**Figure 1.1:** Microalgal bloom over the Atlantic Ocean, in front of the coasts of Argentinean Patagonia. The different colors exhibited in the bloom correspond to the different algal communities. Image Credit: NASA [13].

phosphorus, and iron can generate an uncontrolled proliferation of microalgae. This gives rise to a dense suspension of cells at the surface of the ocean, called *microalgal bloom* [8, 9]. Blooms can astonishingly cover massive extensions of several hundred or even more than a thousand kilometers over the ocean, as shown in Fig. 1.1. When this occurs, other photosynthetic microorganisms living in deeper areas of the ocean are deprived of sunlight and starve as the dominant algal species in the bloom take most of the light input [10]. Additionally, the release of toxins and secondary metabolites by algae at higher concentrations may cause harmful effects, such as oxygen depletion and water poisoning [11]. This, in turn, can potentially initiate the death of numerous aquatic organisms and the subsequent loss of biodiversity [12].

Besides open water systems, microalgae can also be dispersed and thrive in other habitats. Water currents, raindrops, wind, and other higher organisms can transport

microalgae to places where they may attach to light-exposed wet surfaces and form *biofilms*, see Sec. 1.3. Microalgae can form biofilms on rocks, wood, soil, and on other biotic surfaces, where they may establish complex communities even with microorganisms of different species. The ecological relevance of microalgal biofilms resides in the high metabolic rate of microalgae, which allows them to convert organic waste, that can be harmful to the environment, into less toxic compounds [14]. For this reason, microalgal biofilms have been largely used in bioremediation processes [15, 16], such as in wastewater treatment [17] and maintaining soil fertility [18]. Despite of these benefits, microalgal biofilms can cause biofouling, which can cause detrimental effects on moist artificial surfaces, such as ship hulls, marine equipment, and filtering membranes used in desalination plants [19].

## 1.3 Microbial adhesion to surfaces

The growth of microbial communities, known as biofilm, on biological and non-biological surfaces is a natural and ubiquitous phenomenon manifested by all sorts of microorganisms, namely bacteria [20], microalgae, and fungi. Examples of biofilms are numerous. Archaic types of microbial colonies, known as microbial mats, can be commonly seen near thermal vents or in salt lakes. Other everyday examples encompass gut microbiota, the development of microalgal films on rocks, or the lichen in trees. Biofilms can usually host multiple different species and are considered a dynamic and complex biological system with emergent properties that provide essential survival advantages to their community [21]. These clusters are often encased in an outer polymer layer that can be produced by the microorganism or by the defensive mechanisms of the colonized host.

Since microbial biofilms are so common in a myriad of highly dissimilar surfaces, increasing interest has emerged to understand the strategies that lead microbes to their association with substrates, and, subsequently, to the development of a biofilm. Some related aspects have been explored, with a strong focus on bacteria, given their abundance and relevant implication in biomedical contexts [22]. Most of such studies have been centered on probing the dependence of substrate properties on the emergence and the dynamics of biofilms [23–25]. Also, the steps of bacterial biofilm formation have been explored, based mostly on studies using the model bacterium *Pseudomonas aeruginosa*, from which a conceptual five-step model for biofilm development has been proposed [26]. An illustration and description of the steps are provided in Fig. 1.2.

The five steps identified by the model are the initial contact, where bacteria sense and attach to the surface using specialized appendages [22], namely pili and fimbriae, that have evolved to attach to host organisms and even to abiotic surfaces. This irreversible attachment is followed by growth and the production of extra-

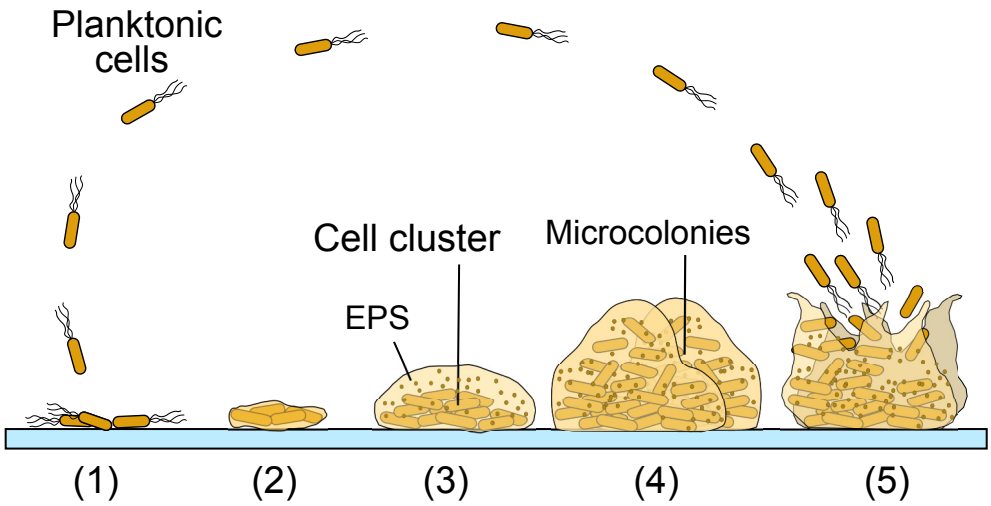


**Figure 1.2:** Conceptual model of five steps leading to biofilm formation. (1) The formation of a biofilm starts with the initial reversible attachment of planktonic cells to the substrate. (2) Subsequently the cells start to lose their flagella and to produce proteins that fix the cell body to the substrate. This stage is known as irreversible attachments. (3) The fixed cells proliferate and form a cluster that is several cells thick. The cells in the cluster produce extracellular polymeric substances (EPS), which are a source of nutrients and provide protection to the colony, which can become resistant to anti-microbial treatments. (4) The EPS allows the biofilm to fully mature into multiple microcolonies. (5) Finally, cells leaving the biofilm can be passively dispersed or can actively migrate to other locations, where they can form a new biofilm. Inspired by [27].

cellular polymeric substances that allow the microbes in the film to grow in three dimensions until the cells are dispersed to other areas. Although, the five-step model explains several general aspects of biofilm formation, the dynamics of biofilm development are much more complex in reality. For instance, it has been found that blue light can induce oxidative stress in *P. aeruginosa*, which prevents bacteria to form biofilms [28]. The opposite scenario, where blue light enhances cell-cell interaction of a bacterial biofilm, has also been reported [29]. After ten years since it was published, the five-step model has been extended to more plausible situations [27]. Yet, it does not cover the formation of biofilm of other important microorganisms, such as algae. Their behavior is strongly affected by light and, thus, microalgae might use other strategies or cues to attach to surfaces. In order to establish a broader understanding of microbial attachment to surfaces, the fundamental principles underlying microalgal surface colonization need to be elucidated.

Numerous studies on microalgal adhesion have been conducted, although with a particular focus on technological and commercial purposes, such as the ones mentioned in Sec. 1.2. Such studies discuss the dependence of microalgal adhesion and biofilm maturation on different types of materials [30], as well as on the substrate's properties [31, 32], such as roughness, hydrophobicity, charge and the presence of other microorganisms. Although these studies give important insights into how the physicochemical properties of a surface affect the formation and maturation of

biofilms of different microalgal species, they overlook the relevance that light has on microalgal adhesion.

### 1.3.1 The influence of light on microalgal adhesion

It is well-known that light controls many aspects of the life of photoactive microbes, see Sec. 2.4. Yet fundamental studies relating light and its influence on microalgae have focused primarily on understanding photosynthesis [33] and the regulation of cellular processes by the cells' circadian clock [34]. However, recent studies show that light has a relevant impact on the adhesion of microalgae to surfaces and the subsequent maturation of a biofilm. For example, it has been shown that distinct regions of the light spectrum have different results in the growth of the biofilm. A study showed that blue and red light affect the production of lipids and carbohydrates, as well as the photoprotective response of the microalgae within the biofilm [35]. Another study, using confocal microscopy showed that microalgal biofilms cultivated under red and blue light are more homogeneous and less porous, in comparison to cultivation under white light [36]. Other related studies focus on how the light intensity affects the composition of the biofilm [37]. In general, however, many of these studies employ a variety of strains that have not been well characterized or that are non-motile. Furthermore, most of the research on microalgal adhesion is focused on the maturation stage of the biofilms, leaving the first steps of its formation and the way in which single cells adhere to surfaces unexplored.

Just a few fundamental studies highlighting the importance of light on microalgal adhesion to surfaces have been conducted at the single-cell level. One example is the light-induced adhesion of the filamentous microalga *Spirogyra* on glass. *Spirogyra* was shown to adhere fast (about 3 minutes) under blue light and slow (about 60 minutes) under red light [38]. The author speculates that the adhesion is by a cementing substance or mucoprotein.

The most recent studies on microalgal adhesion to surfaces have been conducted by Kreis *et al.* using the green unicellular flagellated microalga *Chlamydomonas reinhardtii*, see Sec. 2.1. The magnitude of the adhesion forces of individual cells has been meticulously characterized on different substrates using a micropipette as a force sensor [39], see Sec. 3.2. Interestingly, it has been shown that the adhesion of *Chlamydomonas* to surfaces is induced by blue light and inhibited by red light [40], see Sec. 2.5. The results of Kreis *et al.* open a rich spectrum of possibilities to investigate the underlying principles of microalgal adhesion to surfaces. In fact, the use of *Chlamydomonas* as a case study seems a good starting point since it is a well-established model organism and its genome is known [41]. This opens up the possibility to design systematic studies on genetically modified *Chlamydomonas* strains with altered responses to their light-induced adhesion. In fact, it is known that there are 18 blue-light photoreceptors controlling the behavior of *Chlamydomonas*

[42], the question is: which one mediates light-induced flagellar adhesion?

## 1.4 Scope of the thesis

This thesis aims at unraveling the adhesion of the flagellated microalga *Chlamydomonas reinhardtii* to surfaces, which is mediated by blue-light sensitive photoreceptors [40]. The main goal is to identify the blue-light photoreceptor that mediates the light-switchable adhesion phenotype of *Chlamydomonas*. In order to achieve this goal, I performed adsorption experiments on the population level, as well as single-cell micropipette force spectroscopy experiments. The experiments are performed using a reference wild-type strain and genetically modified *Chlamydomonas* strains (mutants), for which one or two photoreceptors have been deleted. If a particular photoreceptor deletion mutant does not exhibit light-switchable adhesion, then the deleted photoreceptor is, somehow, involved in the manifestation of the adhesion phenotype. The main goal is then divided into three objectives:

1. Develop and establish a protocol to quantify the kinetics of light-induced adsorption of *Chlamydomonas reinhardtii* strains to surfaces.

2. Perform micropipette force measurements to quantify the differences in the magnitude of the adhesion forces between a wild-type strain and the photoreceptor deletion mutants.

3. Identify the roles that different photoreceptors have in the adsorption kinetics and the magnitude of adhesion forces involved in the adhesion of *Chlamydomonas* to surfaces.

The thesis is organized as follows. Chapter 2 is divided into three main sections. The first one provides an introduction to the biology of the model organism *Chlamydomonas reinhardtii*, as well as well-known light-induced responses controlling its motility. The second section presents a summary of the research of every studied blue-light photoreceptor in *Chlamydomonas*, highlighting the phenotypes that they might control. The third section introduces the light-switchable adhesion phenotype of *Chlamydomonas* and provides a summary of studies about the mechanisms underlying the adhesion of *Chlamydomonas* to substrates.

Chapter 3 introduces the strains used in this thesis, as well as the experimental protocols that I followed to perform adsorption experiments and micropipette force measurements. Both experimental techniques are used in a complementary fashion to address the main goal of this thesis.

Chapter 4 addresses the first objective provided in the list above. Adsorption experiments are performed using wild-type and a non-phototactic mutant strain. A

descriptive model is established in order to characterize the rate of adsorption and how fast *Chlamydomonas* cells switch their flagellar adhesiveness.

Chapter 5 presents results of adsorption and micropipette force measurements carried out using mutant strains lacking channelrhodopsins, i.e. the photoreceptors controlling the swimming motility of *Chlamydomonas* in response to gradients of light. In addition to this, results on cells lacking phototropin, a photoreceptor known to be located in the flagella of *Chlamydomonas*, are also presented. The results describe the role of two of the most well-studied photoreceptors in *Chlamydomonas*, which partially addresses the third objective.

The first part of Chapter 6, introduces an extended action spectrum of the flagellar adhesion forces and serves as a motivation to measure adsorption kinetics and flagellar forces using mutant strains that lack cryptochromes. In the second part of the chapter, the results of such experiments reveal the relation between cryptochromes and light-switchable adhesion, addressing the main question. The chapter closes with preliminary results obtained from early-morning adsorption experiments, as well as experiments performed using cryptochrome mutants of another widely-used *Chlamydomonas* wild-type strain.

Chapter 7 presents a conclusion based on the main results discussed in chapters 4 to 6. Finally, I provide an outlook highlighting future research directions aiming at unraveling the signaling pathway and flagellar structural differences driven by light-induced adhesion. Additionally, experiments on strains different than *Chlamydomonas* are suggested, in order to assess the extent of the adhesion phenotype in the evolutionary tree of life. Finally, examples of potential technological applications that stem from this thesis are also provided.

# Chapter 2

# State of the Art

## Meet *Chlamydomonas reinhardtii*

## 2.1 The genus *Chlamydomonas*

The genus *Chlamydomonas* describes unicellular green microalgae that are structurally characterized by two anterior flagella of the same length, a cell wall, and a single chloroplast. The genus was established by C. G. Ehrenberg between 1830 and 1838 [43] and the number of species assigned to it experienced a huge increment ever since. Nowadays, the genus *Chlamydomonas* is composed of more than 500 species that, over the course of time, have been described based on morphological characters. However, given that the characteristic traits defined by Ehrenberg are found in other taxa (e.g. in the genus *Chloromonas*) a more accurate revision of the genus, using molecular phylogenetics, was started by Pröschold in 2001 [44].

Although the genus *Chlamydomonas* is still under constant revision, there is a general consensus that the species *Chlamydomonas reinhardtii* (from now on *C. reinhardtii*), described by Dangeard in 1888, serves as the main reference to the genus [45]. There are indeed several reasons that led *C. reinhardtii* to stand out over other species of its genus and become both a reference species and a model organism to study several fundamental biological phenomena. Initially, one of the main reasons was that *C. reinhardtii* grows vegetatively[1] as a haploid[2], which enables immediate expression of mutant phenotypes and thus makes this species suitable for classical genetic studies [46]. Furthermore, *C. reinhardtii* anticipates changes in light conditions as it possesses a circadian clock, which makes it suitable for studying three fundamental biological phenomena: cell division, photosynthesis, and the biogenesis of cilia [47]. A comprehensive summary of further reasons to consider *C. reinhradtii* as a model organism has been written by Sasso and others [48]. As *C. reinhardtii*

[1]Vegetative cells are the ones that undergo asexual reproduction, i.e., mitotic division.

[2]Haploid cells contain a single set of chromosomes. If there are two sets of each chromosome of the haploid set, the cells are termed diploid.

is the most studied species of its genus, the use of the terms *C. reinhardtii* and *Chlamydomonas* will be used interchangeably, unless otherwise specified.

In the following sections, I describe the architecture and the biology of *C. reinhardtii* at a general level. Specific details can be found in the book *The Chlamydomonas Sourcebook, Volume 1,3* [45, 49] and other written sources that will be properly addressed.

## 2.2 Anatomy of *C. reinhardtii*

The architecture of *C.reinhardtii* roughly consists of two main parts: the cell body and two filaments, called *cilia* or *flagella*[3], that closely protrude from the cell body. In this section, I briefly describe the structures in the cell body, highlighting the functionalities of its most notable organelles and then I describe the flagella and their importance to the cell's locomotion and interaction with surfaces.

### 2.2.1 Cell body

The shape of the cell body of *Chlamydomonas* is slightly ellipsoidal with a typical diameter of around 5-10 µm. As any eukaryotic cell, the cell body contains the nucleus and the different organelles that sustain the cell's biological processes. Most of the species exhibit a clear polar structure, in which the chloroplast is localized at the base of the cell body, partially surrounding the nucleus, and the two flagella emerge from the anterior side of the cell body. A schematic of a typical *Chlamydomona* cell is shown in Figure 2.1.

The cell body is encased by the plasma membrane, which in turn is surrounded by a multilayered cell wall. Studies of the chemical composition of this cell wall in *C. reinhardtii* show that it is composed of glycoproteins rich in hydroxyproline and other sugars, such as mannose, galactose, and glucose [45]. Electron microscopy studies to elucidate its structure have been conducted by Roberts and others and show that the cell wall of vegetative *Chlamydomonas* is formed by seven layers, whose estimated thickness varies from 100 to 450 nm [51].

Within the cell body, the most prominent organelle is the chloroplast, which accounts for 40% of the cell's volume and typically occupies two-thirds of the basal body. Morphological studies show that the chloroplast is cup-shaped, partially surrounds the nucleus, and contains other organelles that drive the production of energy and structural sugars via photosynthesis [45]. One of those organelles is the pyrenoid, a liquid-like microcompartment that is involved in the fixation of atmospheric $CO_2$ [52].

[3]Historically, the term *flagellum* has been preferred when these structures are present singly or in small numbers. The term *cilium* is used when the structures are present in larger numbers [50].

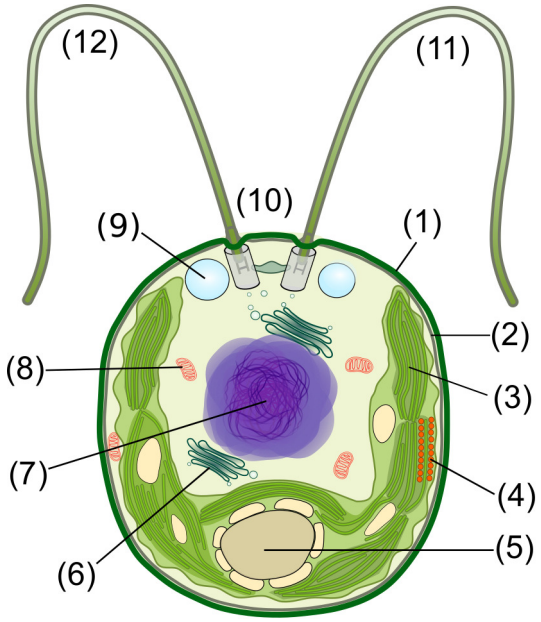


**Figure 2.1:** Representation of a typical *Chlamydomonas* cell. The cell body is enclosed by a multi-layered cell wall (1) and the plasma membrane (2) and it contains several organelles and structures, such as the chloroplast (3), the eyespot (4), a pyrenoid surrounded by granular starch reserves (5), Golgi apparatus (6), the cell nucleus (7), mitochondria (8), vacuoles (9) and the basal bodies (10). Each flagellum emerges from one basal body. The flagellum that is closer to the eyespot is referred to as the *cis*-flagellum (11) and the one farther is referred to as the *trans*-flagellum (12).

Another important organelle inside the chloroplast is the eyespot or stigma. The eyespot consists of a regular arrangement of granules with a diameter of 80 to 130 nm [46], located at the equator of the cell body, directly below the plasma membrane. The eyespot is visible under the microscope and it appears with a characteristic orange coloration, due to a high concentration of carotenoid pigments within the granules. In the late 1920s it was already proposed that the eyespot was somehow related to the motility of unicellular microorganisms [53]. A first hint to this relation came with the electron microscopy studies of Gruber and Rosario in 1974, which showed the presence of microtubules near the eyespot of *C. reinhardtii* [54]. Later in 1980, two independent studies finally connected photoreception and motility. On the one hand, freeze-fracture experiments established that there is a specific structural association between eyespot and *C. reinhardtii* flagella [55]. On the other hand, Foster and Smyth gave convincing arguments that the eyespot functions as an optical device in conjunction with photoreceptor proteins and the biochemical processes leading to the cell's reorientation upon light stimuli [56]. A more detailed description of the working principle of the eyespot and its relation to *Chlamydomonas* motility is presented in Section 2.4.1. In the following, I discuss about the flagella, their structure and composition, and their role with regard to the motility of *Chlamydomonas*.

### 2.2.2 Flagella

Flagella or cilia are structures found in an ample variety of organisms, including bacteria, protozoa, and animals [57]. In nature, flagella are important for a variety of reasons. Some species, such as bacteria or spermatozoa use them to propel themselves in liquid environments [58, 59] or to sense their surroundings [60]. More complex organisms, such as mammals, exhibit large arrangements of cilia that control the transport of fluids. For instance, cilia in the respiratory tract are used to remove debris by transport of mucus along the surface of the tract [61]. There are even complex arrangements of cilia in the cavities of the brain, which transport cerebrospinal fluids and can modify their beating to regulate the distribution of substances over the brain [62].

Cilia are also fundamental in the control of left-right asymmetry in the placement and patterning of the internal organs during morphogenesis [63]. Malfunctions in this highly complex system can lead to a variety of disorders known as cilipathies. Such disorders can affect the respiratory system, the kidneys, and other organs [64]. As the structure of cilia is highly conserved between microorganisms and mammals, the study of cilia in model organisms, such as *C. reinhardtii* have tremendously advanced our understanding of cilia malfunctions in humans [65, 66].

#### Structural components of the flagella

Studies of the flagellar structure started as early as 1950s with the use of electron microscopy. These studies allowed for a meticulous description of different structures of interest. Further information can be found in the review by David Ringo [67] and in the *Chlamydomonas Sourcebook, Volume 3*[49].

The flagella of *Chlamydomonas* consists of two hair-like filaments that protrude in proximity from the basal body, at the anterior pole of the cell, see Figure 2.1. The dimensions of the flagella are independent of the size of the cell body and exhibit a typical length between 10-14 µm, with a diameter of about 200 nm [68]. Each flagellum consists of a central cylindrical structure, called *axoneme*, that is surrounded by the flagellar membrane, which is a specialized extension of the cell's plasma membrane. As opposed to the plasma membrane, the flagellar membrane lacks a cell wall and therefore acts as a sensory apparatus that allows for direct interaction of membrane-bound proteins with the cell's environment.

#### The axoneme

The axoneme is a microtubule-based cytoskeleton that forms the core architecture of any flagella. The structure of the axoneme found in *Chlamydomonas* is similar to the one found in other flagellated algae and even similar to mammalian cilia. A schematic of this complex structure is shown in Figure 2.2a.

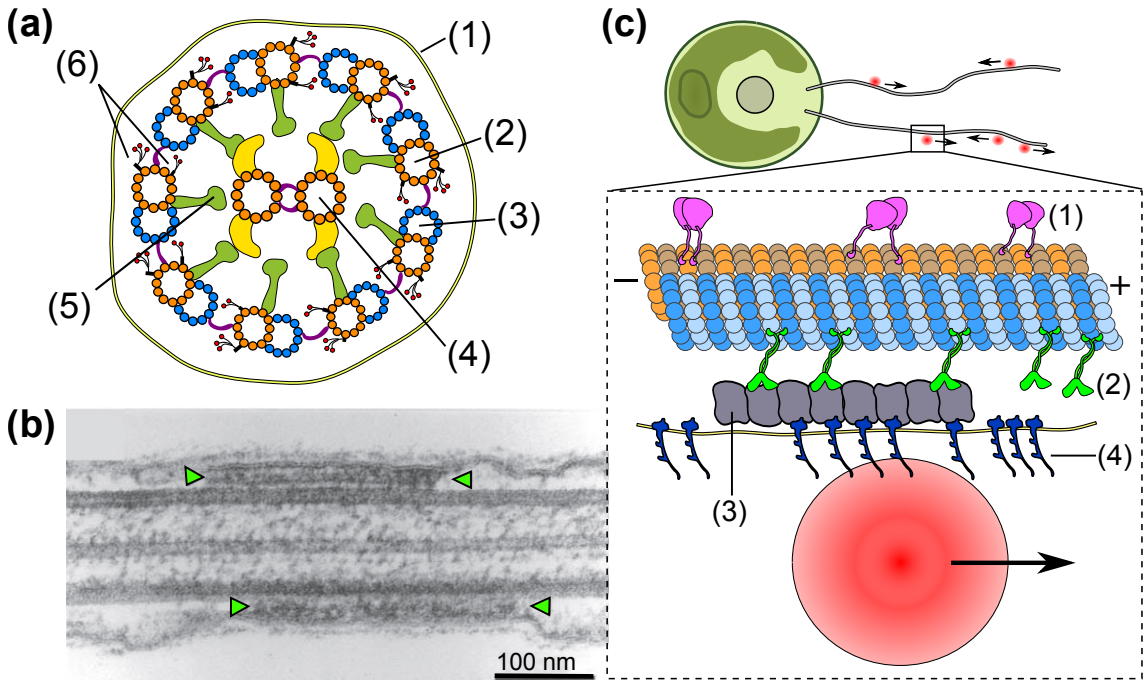


**Figure 2.2:** (a) Cross-section of a flagellum showing the axoneme enclosed by the flagellar membrane (1). The axoneme consists of a circular array of nine interconnected microtubule doublets, each of which is composed by an A-microtubule (2) and a B-microtubule (3). A-microtubules are connected to the central microtubule pair (4) by protein complexes called radial spokes (5). Inner and outer dynein arms (6) transit along A-microtubules. (b) Electron micrograph of a longitudinal section of a *C. reinhardtii* flagellum. Green arrows highlight IFT particles between one outer double microtubule and the flagellar membrane (reproduced from *The Chlamydomonas Sourcebook, Vol. 3* [49]). (c) Schematic of microbead translocation along the flagellar membrane [69]. The section of one flagellum (not to scale) shows two types of molecular motors transiting along one microtubule doublet. Retrograde dynein motors (1) transit along the A-microtubule towards the cell body (minus end) and anterograde kinesin motors (2) transit along the B-microtubule towards the tip of the flagellum (plus end). IFT particles (3) are shown to be associated in a linear array (IFT-train) and transported by kinesin motors. The main glycoprotein in the flagellar membrane, FMG-1B (4), is also shown associated with IFT particles. FMG-1B is known to promote flagellar adhesion to surfaces [70] and also mediate microbead translocation along the flagellar surface [71]. The arrow shows the direction of motion of the red microbead.

The structure of the axoneme is axisymmetric and consists of a central pair of microtubules, surrounded by nine *doublet* microtubules. This characteristic arrangement is sometimes referred to as the 9×2+2 axoneme. The doublets surrounding the central pair consist of paired tubules, designated as A and B. Tubules A and B are composed of 13 and 11 protofilaments[4] respectively, whereas each tubule conforming the central pair is composed of 13 protofilaments. External doublets are interconnected by flexible nexin filaments and radial spokes arise from type-A microtubules and can interact with projections of the central pair. Each outer microtubule has

[4]Protofilaments are the resultant structure of polymerized $\alpha/\beta$-tubulin dimers, which are globular proteins that form the single unit of microtubules.

associated either dynein [72, 73] or kinesin [74] molecular motors, which are specialized proteins that mediate the active transport of proteins along the axoneme. This process is called intraflagellar transport (IFT) [75] and the protein complexes that are translocated by flagellar motors are termed IFT particles, see Section 2.3.2.

### The flagellar membrane

I previously mentioned that the flagellar membrane covering the axoneme is a continuous specialized extension of the plasma membrane and thus exhibits several different features. The flagellar membrane, as opposed to the plasma membrane, is covered with a sheath of glycoproteins and glycolipids that constitute the so-called *glycocalyx*, which extends about 16-18 nm from the surface of the flagellar membrane [76]. The glycocalyx is composed of the glycoprotein FMG-1B, which is known to account for cell-surface interactions and specific types of motility that will be discussed later. Other structures of interest present in the glycocalyx are mastigonemes, and sexual agglutinins. The latter structures are found specifically *Chlamydomonas* cells undergoing sexual reproduction, namely gametes. The following sections provide an overview of these three important proteins in the flagellar membrane in light of their biological functions in *Chlamydomonas*.

### FMG-1B: the main glycoprotein in the flagellar membrane

The composition of the flagellar membrane of vegetative and gametic *Chlamydomonas* is dominated by the glycoprotein FMG-1B[5]. It is estimated that there are around 90000 copies of this protein uniformly distributed along the surface of the flagellar membrane [77]. It is not clear though whether the "*fuzziness*" of the glycocalyx, seen in electron micrographs, corresponds to the ectodomain[6] of FMG-1B or to a combination of ectodomains and chain-like covalent associations of few sugars to the N-domain of FMG-1B.

Early in 2000, the use of monoclonal antibodies provided insights into the possible peptide composition of FMG-1B [49]. The predicted composition matches the composition obtained by SDS-polyacrylamide-gel electrophoresis (SDS-PAGE)[7] and shows that FMG-1B is composed by 4149 amino acids.

At the structural level, FMG-1B possesses a long N-terminal domain, a single

[5]UniProt database: Q84X68. `https://www.uniprot.org/uniprotkb/Q84X68/entry` (retrieved on 20.04.2023)

[6]The ectodomain is a portion of a transmembrane protein that is projected out of the membrane.

[7]Polyachrilamide gel electrophoresis is a common technique to separate a mixture of proteins according to their molecular weight.

transmembrane domain and a short C-terminal cytoplasmic domain[8].

The C-terminal consists of 17 amino acids and, despite its short extension, it is believed to participate in the signal transduction and coupling of FMG-1B to transport proteins along the axoneme. The ectodomain of FMG-1B is composed of over 4100 amino acids over which there are 31 potential sites for N-glycosylation.

N-glycosylation is a common phenomenon in all pro- and eukaryotic organisms that consist of a covalent attachment of oligosaccharides[9] to the nitrogen atom in the amino acid asparagine [78]. The process of N-glycosylation occurs firstly at the endoplasmic reticulum, where a first group of simple sugars is linked to the amino acid asparagine. Usually, the first part of this structure is highly conserved across different domains of life and thus it is referred to as the *core* structure, see Figure 2.3. After the synthesis of the N-linked core structure, the process of adding more simple sugars then continues at the Golgi apparatus [79]. In *Chlamydomonas*, the core structure associated with asparagine is formed by N-acetylglucosamine and mannose, which can in turn be linked to the sugars xylose and fucose [80].

Recently, it was shown that FMG-1B can interact and couple to IFT trains and has direct support in both surface association and gliding motility [81], see Section 2.3.3. Furthermore, N-glycosylation also plays a role in flagellar adhesion of *C. reinhardtii* as the reduction of its N-glycan complexity hinders the adhesion force required to bind its flagella to the surface [82].

### Mastigonemes

Mastigonemes are fine flagellar appendages that extend from the flagellar membrane. They are only found on the flagella of protists and are especially common among biflagellate algae [49]. In *Chlamydomonas*, mastigonemes are distributed in two rows on opposite sites of each flagellum and cover around two-thirds of their distal portion. The shape of the mastigonemes is fibrous, as inferred from electron micrographs. The structural length is around 10 µm with a diameter of around 15 nm [67, 83, 84].

For a long time, it was widely hypothesized that the function of the mastigonemes was to increase the effective surface area of the flagellum in order to boost effective thrust as a result of the beating of the flagella [84, 85]. However, a recent analysis that uses optical tweezer-based velocimetry to study the hydrodynamics of mastigoneme-deficient *Chlamydomonas* mutants disproves this hypothesis [86]. The functionality provided by mastigonemes is thereafter still a mystery, provided that there is still a lack of evidence that shows their involvement in flagellar adhesion

[8]In molecular biology, a *protein domain* refers to a region of a protein that folds independently from other polypeptide chains in the protein. By convention, the description of any protein as a chain of amino acids is always reported starting from the amino-terminal end (or N-terminal) to the carboxyl-terminal end (or C-terminal). These are the extreme domains in the protein structure and between them there could be one or more domains.

[9]Oligosaccharides are polymers containing a few simple sugars or monosaccharides.

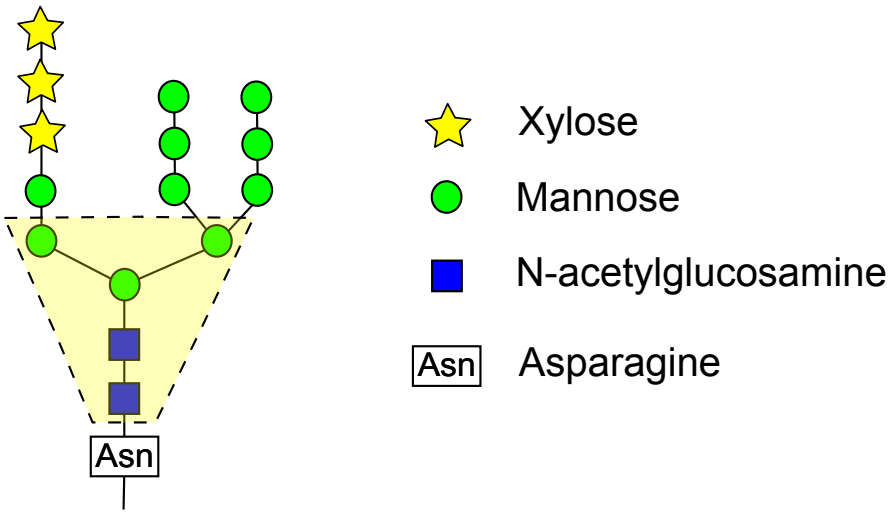


**Figure 2.3:** Schematic depicting a configuration in the N-glycosylation structure found in FMG-1B. The core structure, enclosed in yellow, is generated in the endoplasmic reticulum, and is composed by core N-acetylglucosamine and mannose. This core structure is highly conserved in land plants and also in humans. Addition of monosaccharides to the core structure, such as xylose and mannose, takes place in the Golgi apparatus. Glycosylated structures out of the core are not conserved, given that they depend on the enzyme repertoire in the Golgi apparatus of specific organisms. Inspired by Mathieu-Rivet *et al.* [79].

[87, 88] and other types of flagellar transport [69].

### Sexual agglutinins

*C. reinhardtii* exists either as a vegetative cell or as a gamete, see Section 2.3.1. In both states, mastigonemes and FMG-1B glycoproteins are present. However, only in the gametic state *Chlamydomonas* exhibits elongated glycoproteins in their flagella that enable sexual reproduction and are known as sexual agglutinins. There are two types of sexual agglutinins in *Chlamydomonas*: *plus* and *minus*. The expression of one of these agglutinins in a cell defines a corresponding *mating type*. A cell can thus be either of mating type *plus* (*mt+*) or *minus* (*mt-*).

Sexual agglutinins are peripheral proteins that do not have a transmembrane domain and bind a receptor in the glycocalyx of the flagella. The length of agglutinins is between 200-250 nm of which 90% stands out of the flagellar surface [49]. They are distributed along opposite ends of the flagella, just like mastigonemes.

Structurally, agglutinins have a characteristic cane shape with a globular end, called the *head*, and a long rod-like region that shows a kink or bend, termed *tail hook* [89, 90]. The tail hook is linked to receptor proteins in the flagellar membrane and the head domain is distal and interacts with the flagellar surface of a gamete of opposite mating type.

## 2.3 Physiological aspects of *C. reinhardtii*

Just like any living organism, *C. reinhardtii* require both energy and other nutrients in order to thrive and reproduce in their habitat. The optimal intake of both energy and inorganic nutrients is adjusted by internal feedback processes that induce changes in the cell motility (see phototaxis and chemotaxis in Section 2.3.4). Under optimal light conditions, most of the energy used by cells is obtained by means of photosynthesis, whereas other inorganic nutrients, such as nitrogen, are obtained via diffusion and assimilated by specific metabolic pathways [91]. When light conditions are unfavorable, *C. reinhardtii* can still acquire energy via aerobic respiration [45], where the cells fuel their metabolism and motility through oxygen consumption. In low light conditions, aerobic respiration prevails over photosynthesis and, therefore, the higher rate of oxygen consumption might result in very low oxygen concentration in the environment. Under dark anoxic conditions, where the cells are deprived of light and oxygen, the motility exhibited by *C. reinhardtii* is decreased by around 50% [92], but the cells can still sustain their metabolism by means of anaerobic respiration [93]. In this metabolic mode, *C. reinhardtii* cells activate several fermentation pathways that degrade endogenous carbohydrates (e.g. starch reserves) to produce acetate, from which ATP is generated for energy consumption [93]. Interestingly, among the byproducts of anaerobic respiration is hydrogen ($H_2$) [45]; a potential substitute for fossil fuels, for which *C. reinhardtii* is considered as one of the promising organisms for its bioproduction [94].

As for reproduction, *Chlamydomonas*, and microalgae in general, can undergo two pathways of division. In optimal environmental conditions, *Chlamydomonas* exists as haploid vegetative cells and can divide by mitosis several times per day. However, when conditions become harsher, for instance when inorganic nutrients in the environment are scarce, *Chlamydomonas* cells switch to a gametic state characterized by the translocation of agglutinins from the plasma membrane of the cell body to the flagellar surface [95].

In the following, I describe the two possible reproductive cycles in *Chlamydomonas*. A more detailed description can be found in the *Chlamydomonas Sourcebook, Volume 1* [45].

### 2.3.1 Life cycle

#### Vegetative reproduction

The life cycle of *Chlamydomonas* has been carefully studied in laboratory conditions using synchronous vegetative cultures, where the cells are exposed to alternating light and dark periods [96]. A schematic of this cycle is depicted in Figure 2.4. Cultures are typically grown on a 12:12 hour light-dark cycle with a temperature

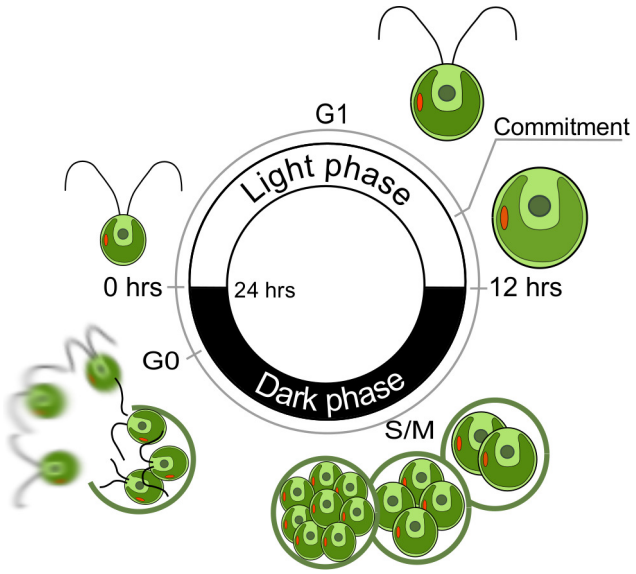


**Figure 2.4:** Vegetative reproduction of *Chlamydomonas* following a 12:12 hour light-dark cycle. A vegetative cell grows during the light phase (G1 phase) and undergoes multiple divisions during the night. The number of cell divisions depends on a minimal cell volume, which defines a control point, termed commitment point [102]. The division stages occur inside the cell wall of the mother cell and consist of an alternation of the synthesis phase (S) and mitosis (M). At the end of the dark phase, the cells regrow their flagella and leave the hatch to restart the cycle.

between 22-25°C. Under these conditions, the cells grow during the day and divide during the night.

The fact that cell divisions occur in synchrony with the occurrence of dark periods implies that the cells possess an accurate internal clock that allows them to track time by means of specific control points along their diurnal cycle. Control points have been hypothesized and modeled early in the 80s usually based on the cell's volume [97–100]. Although there is disagreement in the existence of several control points in the life cycle of *Chlamydomonas* [101], there is at least consensus in one, the so-called *commitment point* [98, 100]. The commitment point occurs during the cells' growth phase and is based on a minimal volume size, calculated by Umen and Goodenough to be 178 $\mu m^3$, though the cell might grow further until the start of the dark period [102].

The vegetative reproduction of *Chlamydomonas* is similar to other eukaryotic organisms. A typical cell cycle consists of a growth phase (G1 phase), a synthesis phase (S)[10], a second growth phase (G2) and mitosis (M), followed by cytokinesis [103]. This characteristic scheme can be modified in different organisms though. In the case of *Chlamydomonas*, a cell grows during the G1 phase, and when it reaches a minimal volume size it 'commits' to divide later. The cell can continue to grow, and over the course of 30 minutes before the start of the dark period, its flagella get shortened until no filament protrudes from the cell body [104]. Shortly after the start

[10]S phase consists in the duplication of DNA.

of the dark period, multiple alternations of the S and M phases occur with no visible occurrence of the G2 phase. Each division event occurs within the confinement of the cell wall of the mother cell, which gives rise to $2^n$ haploid daughter cells, $n$ being the number of division rounds. Shortly before the start of the day phase, the daughter cells regrow their flagella. The cell wall hatches by action of lytic enzymes and the daughter cells are released to the medium to restart the cycle once the day period is started.

#### Gametogenesis and sexual reproduction

Under unfavorable environmental conditions, such as lack of nutrients, *Chlamydomonas* cell undergo gametogenesis, characterized by the translocation of sexual agglutinins from a reservoir in the plasma membrane towards the cells' flagellar membrane [95]. In the laboratory, gametogenesis in *Chlamydomonas* is induced by nitrogen starvation [105]. An illustration of the sexual life cycle of *C. reinhardtii* is depicted in Figure 2.5.

When a cell encounters other individuals of opposite mating type, the cells interact with their flagella in a process called *agglutination*. After pair formation of opposite mating type occurs, the cell wall is degraded and the cell bodies fuse to form a diploid zygote with four flagella (or quadriflagellate cell, QFC) [106]. The four flagella subsequently become shorter until they disappear and the zygote is non-motile. The zygote can further develop into a highly resistant zygospore over the course of several days and can amazingly remain in a *dauer* (i.e. dormant) state for many years [46, 107]. When the environmental conditions become again favorable, the zygote germinates in the light period, generating four haploid cells via meiosis, which are then released from the zygospore to resume vegetative growth [46].

In nature, sexual reproduction can boost the rate of adaptation of *Chlamydomonas* to new or dynamic environmental conditions. This is enabled by the higher probability of mutations that result from sexual reproduction, provided that the genetic diversity in a population of mating-competent individuals is large [108].

### 2.3.2 Protein transport along the flagella

The flagella play a crucial role in the life of ciliated organisms. In the case of *Chlamydomonas*, the flagella serve as a means of locomotion, allowing the cells to look for areas of optimal light exposure and to stay away from harmful substances. Furthermore, flagella are used as sensory organelles as they are not surrounded by a cell wall, which allows the interaction of glycoproteins in the flagellar membrane with the outer environment or the specific recognition of cells of opposite mating type during sexual reproduction. Thus, in order to stay fit and survive in its environment, *Chlamydomonas* has evolved a series of molecular types of machinery

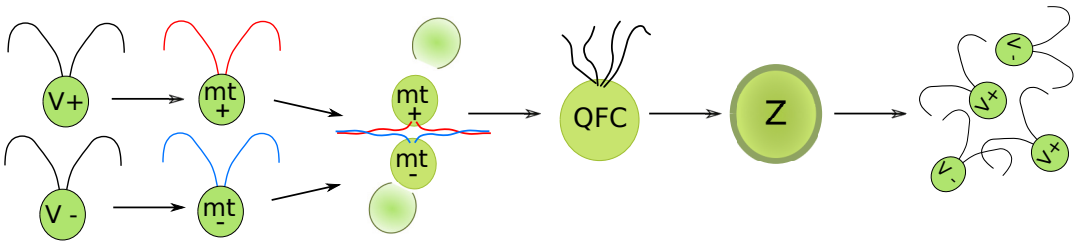


**Figure 2.5:** Sexual life cycle of *Chlamydomonas*. When environmental conditions get harsher, vegetative cells can become gametes of a distinct mating type (*mt+* or *mt-*) and they transfer specific sexual agglutinins to the surface of their flagella. Individuals of opposite mating types pair their flagella, lose their cell walls and then fuse together to form a diploid quadriflagellate cell (QFC). If conditions continue to be unfavorable, the QFC can become a zygospore Z that enters a dormant state that can last years. If the environmental conditions are suitable, the zygospore undergoes meiosis to release four haploid cells that can resume vegetative growth.

to keep their axoneme and flagellar membrane under constant and precise maintenance. As proteins are synthesized in the cell body, the maintenance of flagella should involve the transport of structural elements from the cell body to different parts of the flagella.

Hints of transport phenomena along *Chlamydomonas* flagella were first evidenced by a series of experiments by Bloodgood and others. In 1977, Bloodgood carefully studied the translocation of microbeads along the flagellar surface of *Chlamydomonas* [69]. An illustration of this phenomenon is depicted in Figure 2.2c. Microbeads of diverse surface chemistry were seen to move bidirectionally along the flagella with speeds of around 1.5-2.0 µm/s. The translocations were described by Bloodgood as "*saltatory*", as marker particles could stop and restart their transit along the flagella. The direction of motion of the microbeads could also be reversed but, nevertheless, it always occurred in straight lines, as if the microbeads were transported along tracks. Later on, Bloodgood and others studied a new flagellar-dependent type of motility in surface-associated *Chlamydomonas* cells, namely gliding motility. In this type of motion, *Chlamydomonas* cells have their flagella adhered to a surface, forming an angle of 180° with respect to each other, and one of the flagella pulls the cell body along. Further analysis revealed that the glycoprotein FMG-1B mediated the adhesion of both microspheres to the flagellar surface and the adhesion of flagella to surfaces [109]. However, the nature of mechanochemical events resulting in force being exerted at the flagellar surface was still unclear.

Partial elucidation to this enigma came when Kozminsky and others managed to visualize assemblies of proteins transiting along the axoneme and below the flagellar membrane of *C. moewusii* [75]. They suggested that the maintenance of the axoneme and the flagellar membrane is achieved by the translocation of structural elements that are carried as cargo along the flagella by protein complexes. This process was named intraflagellar transport (IFT) [110].

As the maintenance of flagellar structures needs to respond quickly and constantly to sudden changes in the environment, e.g., changes in pH or loss of one or both flagella by shear flows, one could expect IFT to be based on active transport rather than passive diffusion. Experiments using dynein- or kinesin-deletion mutants of *C. reinhardtii* show that, in fact, anterograde IFT of cargo proteins from the base of the flagella to the tip is mediated by kinesin-2 motors [111], whereas retrograde IFT is carried out by cytoplasmic dynein-1b motors [112]. Proteins carried by these motors form larger protein complexes, usually called IFT particles, which associate into linear arrays, known as IFT trains, see Figure 2.2b,c.

The composition of IFT particles has been studied using biochemical assays [113]. So far, 22 IFT particles have been identified and classified into two subcomplexes: IFT-A and IFT-B [114, 115]. Such complexes have been found to be well-conserved in most ciliated organisms. This discovery paved the way towards fundamental studies that finally related human disorders, such as polycystic kidney disease, blindness, and obesity, to ciliary dysfunctions [116].

The motion of motor proteins and IFT complexes has been studied rather recently and with great detail by Stepanek and Pigino using fluorescence and three-dimensional electron microscopy [117]. Their work remarkably explains the advantage that doublet microtubules in the axoneme structure provide to optimize IFT: one microtubule serves kinesin-mediated anterograde IFT, whereas the other microtubule allows dynein-based retrograde IFT. This enhances the flux of IFT particles in both directions and avoids collisions. The results of such experiments extraordinarily confirm the observations of microsphere translocation made by Bloodgood 40 years earlier.

Although video-enhanced differential interference contrast (DIC) remained the only technique to visualize IFT for several years [118], the use of more sophisticated and higher resolution techniques, such as cryo-electron tomography [119], has revealed the structural complexity of the IFT particles and how they are assembled and released along the flagella [120]. The details of such studies are beyond the scope of this work. Thus, I move on to the next section to discuss the role that protein transport along the flagella has in the two different forms of motility of *Chlamydomonas*.

### 2.3.3 Cell motility

Now that we know some of the proteins that dynamically coexist in the flagella, I will describe the origin of the two types of motility exhibited by *Chlamydomonas*: swimming and gliding motility.

### Swimming motility

Swimming is one of the most common types of motility found in flagellated organisms, which utilize one or more flagella to propel themselves through a fluid environment. The propulsion is the result of waves that transit along the flagella that generate a beating pattern that exerts a force in the surrounding liquid.

In nature, one can find different types of flagellar beating. For instance, the beating of prokaryotic microorganisms, such as bacteria, resembles a cork-screw type of motion [121], whereas flagellated eukaryotes, like microalgae, display different types of flagellar beating patterns [122].

Particularly in *Chlamydomonas*, the coordinated beating of their two flagella resembles a breaststroke-type of motion. This flagellar motion is known to arise from inner and outer dynein motors that transit along the axoneme structure, generating forces between adjacent microtubule doublets [123, 124]. The doublets slide periodically with respect to one another, which generates a periodical bending of the axoneme with a frequency of about 50 Hz. The periodical bending is characterized by a series of power- and recovery strokes that generate a symmetry-breaking pattern, which is fundamental for the propulsion of the cell through a high viscosity (i.e. low Reynolds number) fluid [125]. The swimming speeds of *Chlamydomonas* are typically 50-150 µm/s. High-speed cinematographic studies by Rüffer and Nultsch even showed that the flagellar beating motion, is not contained completely in a plane [126]. This three-dimensional beating makes the cell body rotate counterclockwise with a frequency of 1-2 Hz as it propels through its environment. Then, during synchronous beating, the resulting trajectory of a *Chlamydomonas* cell is helical [127]. We will see in Section 2.3.4 that helical motion is an evolutionary adaptation to track light sources [56].

More recently, Polin *et al.* have noted that forward swimming in *Chlamydomonas* is interrupted by sudden reorientations, or *tumbles*, that change the direction of the cell's trajectory as it swims forward [128]. This results in a well-known type of motion, called *run-and-tumble*, and it arises from transient de-synchronization of the flagellar beating. This motion is also exhibited by flagellated bacteria, such as *Escherichia coli* [129]. The average time between tumbles has been experimentally determined to be around 11.2 s [128]. At longer times, the repetitive changes in the swimming orientation turn the trajectory into a random walk, which overall results in a diffusive motion. The effective diffusivity of *Chlamydomonas* was experimentally measured to be $D \approx 0.7 \cdot 10^{-3}\mathrm{cm}^{-2}/\mathrm{s}$.

Swimming motility in *Chlamydomonas* is also affected by light stimuli. The flagellar beating can be modified when the cell is suddenly exposed to bright light. The change in the flagellar beat pattern is transient and results in backward swimming. We will address backward swimming in Section 2.3.4, when we discuss phototaxis and the photophobic response.

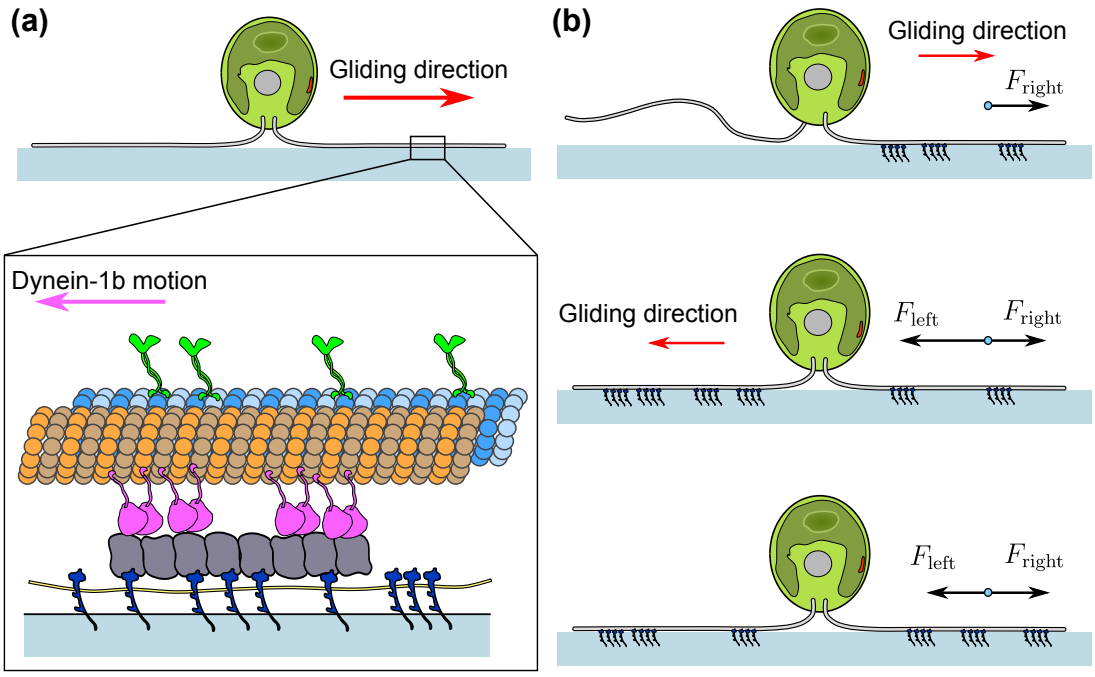


**Figure 2.6:** (a) Force transduction mechanism that generates gliding motility in *C. reinhardtii*. Retrograde dynein motors are unable to move IFT particles that are associated to surface-tethered FMG-1B proteins. However, as dynein molecules tend to keep their march towards the flagellar base they pull the cell body towards the opposite direction. (b) Gliding direction is set by the leading flagellum, which is the one having a larger number of IFT particles engaged to surface-tethered FMG-1B. The leading flagellum has a higher capacity for force transduction, generating a net force that moves the cell body and the trailing flagella along. When there is an equal number of surface-associated IFT particles, opposite pulling forces cancel out and the cell remains static on the surface. Inspired by Shih *et al.* [81].

### Gliding motility

*Chlamydomonas* not only spend their lives in the swimming or planktonic state searching for optimal places to acquire nutrients and perform photosynthesis. In fact, *Chlamydomonas* has adapted to a myriad of ecosystems exhibiting highly intricate surfaces, namely soil, moss, sand, and even glaciers. Actually, most of *Chlamydomonas* strains used for research have been obtained from soil samples, where swimming might not be the predominant type of motility. *Chlamydomonas* cells can indeed adhere to solid surfaces and perform an alternative type of locomotion called: gliding motility [70].

Gliding is a form of whole-cell locomotion, where the flagella appear to be in full contact with the substrate and extend 180° with respect to each other, in the so-called *gliding configuration*, see Figure 2.6. Gliding cells can move at about 1-2 µm/s, with one leading flagellum dragging the cell body and the trailing flagellum along. Gliding cells can stop and resume their gliding motion either in the same or in the opposite direction, which indicates that any of the flagella can be leading the motion.

Formal studies to elucidate the mechanism of force transduction that led to gliding motility started in the 80s with the identification of FMG-1B as the protein that mediates flagellar adhesion to surfaces [109]. Experiments probing gliding uniflagellated cells showed that the cell body always is dragged by the leading flagellum, which indicates that forces are generated against the substrate in a direction from the flagellar tip to its base [70, 130]. This, in turn, suggested that gliding motility is driven by retrograde motors. Almost two decades later, Shih and others proposed an explanation for gliding motility [81]. Using fluorescently-labeled particles, they showed that flagellar membrane glycoproteins that are transported by IFT particles along the axoneme can transiently adhere to the surface. When this happens, IFT particles stop and dynein-1b retrograde motors, formerly linked to the IFT particles, exert a force on the axoneme, which therefore drags the cell body in the anterograde direction, see Figure 2.6a. It was recently confirmed that the flagellar membrane protein responsible for the force transduction is indeed FMG-1B [131].

The fact that either flagellum can act as the leading flagellum suggests that the gliding direction is established by a force unbalance that results from a different number of surface-tethered IFT particles in each flagellum. Essentially, the flagellum that has more IFT particles attached to the surface is the one that leads the motion. The forces exerted by IFT trains have been calculated to be on the order of tens of piconewton [81]. Since for a single molecular motor the forces are approximately one order of magnitude smaller, this result indicates that several motors engage in a cooperative manner in IFT [132].

Gliding motility is a process that is regulated by calcium ions ($Ca^{2+}$) at a micromolar concentration [133]. Interestingly, it has been found that $Ca^{2+}$ is involved in several signaling processes in the flagella, such as the motion of retrograde IFT-trains, the association of IFT with glycoproteins [134, 135] and the regulation of flagellar beating [136]. Nevertheless, the mechanisms underlying calcium-dependent reactions affecting the motility of *Chlamydomonas* is still a matter of debate [135].

### 2.3.4 Cell behavior

#### Phototaxis and the photophobic response

Light can be very appealing for every photoactive organism. However, it always has to be absorbed in optimal doses as excess light can result in irreversible photodamage [137]. In order to avoid photodamage while maintaining constant exposure to light, many photosynthetic motile organisms have evolved a feedback mechanism that allows the cells to assess how favorable their exposure to light is. This feedback mechanism is known as *phototaxis*.

In general terms, phototaxis is a ubiquitous feedback response in nature [138], and is described as the tendency of an organism to move along gradients of light

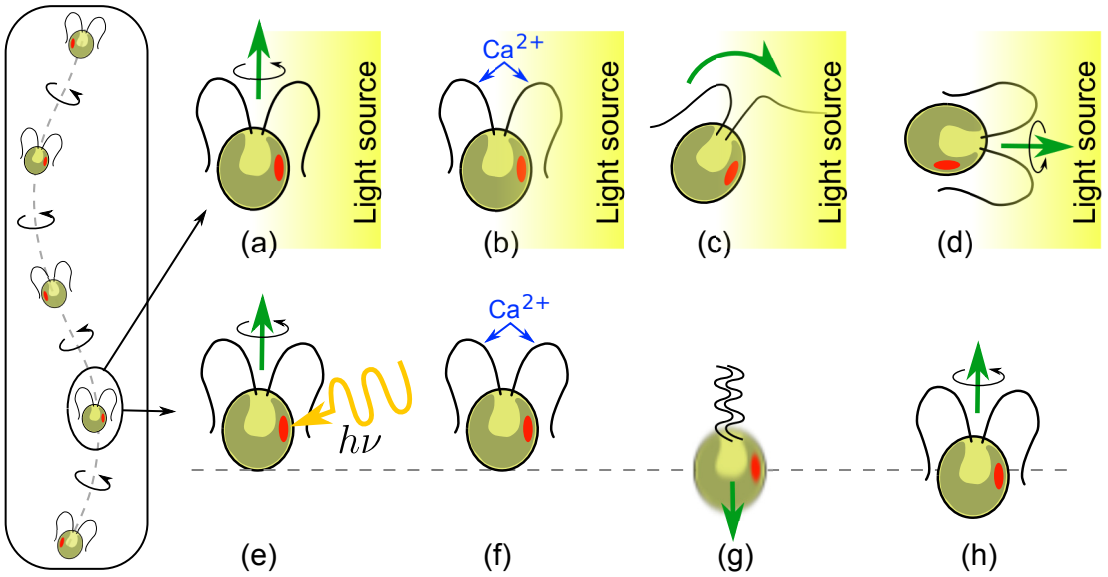


**Figure 2.7:** (a) A swimming *Chlamydomonas* cell rotates around its longitudinal axis. Its eyespot contains light-sensitive molecules (see Section 2.4.1) that receive a periodically varying light stimulus as the eyespot faces towards or away a light source. (b) The modulation of the light intensity in the eyespot triggers an influx of $Ca^{2+}$ to the flagella, which changes the beating pattern of the cis-flagellum. (c) The cell steers then towards the light (positive phototaxis) or away from it (negative phototaxis). (d) The light variation in the eyespot ceases when the cell is swimming towards the light source. (e) If the eyespot suddenly receives a high-intensity light stimulus, a photophobic response may be triggered. (f) Intraflagellar $Ca^{2+}$ levels rise rapidly. (g) The flagella exhibit a transient sinusoidal beating pattern that make the cell swim backwards. (h) After around 300 ms the cell finally resumes phototactic forward swimming. Inspired by Witman *et al.* [83].

intensity. When an organism moves along an increasing light intensity gradient (i.e. towards a source of light), it is referred to as "positive" phototaxis. Whereas when an organism moves away from the light source it is referred to as "negative" phototaxis.

In the case of *Chlamydomonas*, phototaxis is a sophisticated response that results from a signaling cascade initiated by the perception of a light stimulus and that culminates with the modulation of the flagellar beating to produce a change in the cell's orientation. I previously mentioned that swimming *Chlamydomonas* cells rotate around their longitudinal axis at around 2 Hz. This swimming strategy helps the cell to perceive sources of light as the eyespot "scans" its surroundings. If swimming occurs perpendicular to a light source, the eyespot then receives a periodic light signal. This alternating reception of photons by the photoreceptor molecules in the eyespot triggers an influx of calcium across the flagellar membrane, which modifies the beating of the cis-flagellum. This in turn reorients the swimming direction slightly towards the light source, until the eyespot receives a constant light intensity, see Figure 2.7a-d.

In cases of a sudden flash of light intensity, a so-called photophobic response may be triggered [139]. In this response, a flagellar breaststroke pattern of forward-

swimming individuals is modified to a sinusoidal form due to a $Ca^{2+}$ influx across the flagellar membrane [136], which triggers a transient backward swimming, see Figure 2.7e-h. Around 300 ms after the response, the flagella then resume the breaststroke pattern and the cells continue to perform phototactic, forward swimming.

### Chemotaxis

As *Chlamydomonas* not only relies on photosynthesis to acquire energy but also in the acquisition of nutrients and avoidance of toxic substances, it has evolved chemotactic behavior. Chemotaxis is the active motion along chemical concentration gradients. Similarly to phototaxis, chemotaxis can either be described as *positive* or *negative*, depending on whether the cells migrate towards higher or lower concentrations of a chemical species, respectively.

Several chemotactic assays by Ermilova and others have been performed using *C. reinhardtii* to determine its affinity to certain chemical species. The first assays showed that the sugars maltose and sucrose are chemoattractants for *C. reinhardtii* [140]. Subsequent assays show that vegetative *C. reinhardtii* cells exhibit positive chemotaxis to nitrogen sources, such as ammonium ions [141, 142], nitrate [143] and nitrite [144]. Interestingly, the studies also found that chemotactic responses to those substances vary over the circadian cell cycle and are even absent after vegetative cells turn into mature gametes [145]. This suggests then a correlation between chemosensitivity and the sexual cycle of *Chlamydomonas*. A recent study using a stable chemical gradient of bicarbonate[11] in a microfluidic device showed that vegetative *C. reinhardtii* cells exhibit high affinity towards this inorganic carbon source [146]. The study also found that chemotaxis towards bicarbonate depends on the circadian cycle of the cells, reaching its highest affinity during the cells' dark phase.

Despite that chemotaxis is a well-known response exhibited by *Chlamydomonas*, there is still no explanation of its underlying mechanisms. The sensing of gradients suggests the existence of chemoreceptors that specifically bind to the aforementioned substances, but still none of them have been identified so far. Nevertheless, since the studies show that chemotaxis varies along the cells' circadian cycle, it is accepted that there is a strong correlation between optimal nutrient acquisition, via chemotaxis, for subsequent performance of the photosynthetic machinery [147].

### Gravitaxis

In order to explore environments that are exposed to light, *Chlamydomonas* needs to spend most of its time in the upper regions of the soil habitat. Natural selection thus has favored individuals that could swim more easily against the gravity field. As a consequence, *Chlamydomonas* naturally perform negative gravitaxis, i.e. directed

[11] Bicarbonate is the main inorganic carbon source for aquatic photosynthesis.

motion against gravity [148].

Negative gravitaxis was originally thought to arise from a specific biosensor that could detect the orientation of the gravitational field by means of calcium signalling, similarly to higher plants [149]. However, subsequent gravitactic assays using specific calcium-channel inhibitors have ruled out this hypothesis [150]. Later studies conclude that gravitaxis only depend on the cells' shape and can be explained purely by physical arguments [148].

When we discuss the anatomy of *Chlamydomonas* in Section 2.2.1, we showed that the chloroplast is located at the posterior region of the cell body, opposite to the flagella. The mass difference between the chloroplast and the flagella gives the cells a *bottom-heaviness*, which causes the center of mass to be separated from the center of buoyancy. This then results in a gravitational torque that tends to reorient the cells against gravity. Rather recently, experiments and modeling by Kage and others suggest that the presence of the flagella is quite relevant to the upward orientation of *Chlamydomonas* [151]. The difference in the drag coefficient between flagella and the cell body causes them to orient upwards as they sediment. This then strongly suggests that upward reorientation arises from an interplay between bottom-heaviness of the cell-body and viscous drag of the flagella.

In the first part of this chapter I introduced the model organism *C. reinhardtii* and discussed relevant phenomena about its biology and behavior that will be taken into consideration for the present work. I mentioned that light plays a major role in the life of *C. reinhardtii*. In fact, light not only serves as a source of energy for the cell, but it constantly influences the cell's motility and is also used as an environmental cue that elicits circadian entrainment, which sets the phases of the cell's growth and vegetative reproduction.

It is worth to mention that the use of *C. reinhardtii* transcends the study of purely biological phenomena. Fundamental research aimed at understanding its biology has, in fact, made *C. reinhardtii* a suitable model organism to understand biological phenomena from the perspective of active living matter physics [152].

The knowledge about *C. reinhardtii*'s physiology, metabolism, behavior and the access to a myriad of genetically modified strains allow for precise adjustments of different control parameters. This, in turn, opens a door to systematic studies of a multitude of fascinating dynamics displayed by *C. reinhardtii*, which span several length- and time scales. Fast coordinated activity of molecular motors [81], synchronization of flagellar beating [153] or even slow, mesoscale emergent phenomena in dense microbial suspensions [154] are just a few examples of the recently explored topics.

In the next sections, I will discuss how different light-sensitive molecules or photoreceptors in *C. reinhardtii* generate light-mediated responses. I will then describe an important light-induced response that allows the cells to transition from swim-

ming motility to the surface-associated gliding motility. This response is known as light-switchable adhesion and it stands at the core of the present work.

# Light-induced responses in C. reinhardtii

## 2.4 Photoreceptors in *C. reinhardtii*

Light is the most important environmental cue for many of the (living) species on our planet [155]. Photoactive organisms, for instance, base much of their biology on light-mediated processes, such as photosynthesis and the circadian rhythm. The occurrence and regulation of such processes have their origin at the molecular level, where light interacts with specialized light-sensitive proteins called photoreceptors.

Photoreceptors are proteins that evolved the ability to turn a light stimulus into a physiological response, such as a change in motility, synthesis of structural proteins or the resetting of the circadian cycle. In other words, photoreceptors transform light into information, which enables the photoactive organisms to adapt to the dynamics of their environment.

Photoreceptors inherit their sensitivity to light from the association to photosensitive organic molecules, called *chromophores*. Upon reception of a light stimulus, chromophores become more energetic and they transfer their excess of energy to the non-photoactive structure of the photoreceptor, namely the *apoprotein*[12]. However, the energy transfer is triggered only when the chromophores are exposed to specific wavelengths of the sunlight spectrum [156]. In other words, the chromophores endow the photoreceptors with an *absorption spectrum*, and the chemical reactions started by the chromophore are elicited more efficiently upon exposure to certain ranges of wavelengths. As the first microorganisms that populated the Earth evolved underwater [157], where only the shorter wavelengths of the solar spectrum are physically able to reach a substantial depth [158], the sensitivity of photoreceptors has been evolutionary biased to respond to wavelengths in the UV-blue range. Such ancient photoreceptors are commonly referred to as *blue-light photoreceptors*.

In *C. reinhardtii*, the functionalities of most of the blue-light sensitive photoreceptors have remained, for many years, unknown. However, with the sequencing of the genome of *C. reinhardtii* [41] and the recent development of optimized gene editing tools [42], the generation of targeted photoreceptor-deletion mutants has allowed to study the biological relevance of several light-sensitive proteins in *Chlamydomonas*. Up to today, a total of 18 blue-light sensitive photoreceptors have been deduced from the genome of *Chlamydomonas* [42]. These are categorized in just four groups, according to the chromophore they bind to: rhodopsin-, cryptochromes-,

[12]Formally speaking, a photoreceptor is a type of *holoprotein* that consists of an amino acid chain, or apoprotein, in association with a *prosthetic group*; in this case, the photoactive chromophore.

phototropin- and UVR8-type photoreceptors.

Blue-light photoreceptors and their biological relevance in *C. reinhardtii* are discussed in the following sections. I put special emphasis on the discussion of rhodopsins, the most well-characterized photoreceptors; and cryptochromes, which are also of special importance to the present work.

### 2.4.1 Rhodopsins

Franz Boll was a young well-educated physiologist of the late 19th century. Ever-troubled by health problems, he escaped from the colorless cold days of Germany and sought for a better life in the warmth of Italy. As he analyzed the anatomy of eyes taken from dozens of freshly-killed frogs, he was surprised to see that the intense red pigmentation in the frogs' retina tissues turned transparent upon exposure to light. More strikingly, he observed that the pigmentation was recovered in darkness [159]. Puzzled by this intriguing phenomenon, Boll only managed to intuit that the reversible bleaching of the red pigment was involved in animal light perception. Subjected to his ailments, Boll's longing for a *dolce vita* came to a sour end as he died from tuberculosis at the dawn of his 30s. Fortunately, Boll's findings did not escape the attention of the prominent physiologist Wilhelm Kühne, who named the red pigment *rhodopsin* and conducted meticulous studies that, consequently, helped to understand the phenomenon of vision, not only in animals, but also in lower organisms [160].

Decades before rhodopsin was thought to play an important role in animal vision, biologists already suspected that the influence of light in the swimming direction of tiny flagellated organisms was the result of a rudimentary form of vision [161]. Indeed, by the time that Boll and Kühne had suggested the biological relevance of rhodopsin in animal vision, biologists already speculated that the distinctive red organelle seen in many flagellated green algae, namely the eyespot (see Section 2.2.1), was the structure responsible for photoperception [162, 163]. The nature and location of the corresponding photoreceptor, however, remained yet to be determined for several decades.

A few decades into the 20th century, significant progress was provided by Wald and Hubbard on the photochemistry of rhodopsin. They found that rhodopsin consists of two parts: an apoprotein, which Wald called *opsin* and the associated chromophore, *retinal*, which gives rhodopsin its characteristic red color [164, 165]. Through a series of remarkable publications, they explained that photobleaching of rhodopsin results from isomerization[13] of retinal, followed by its dissociation from the opsin protein [166–168]. The detailed explanation of this reaction, at the biochemical and molecular level, laid the groundwork for the understanding of light perception

[13]Isomerization is the transformation of a molecule into a different isomer (i.e. a molecule with identical chemical composition, though in a different arrangement).

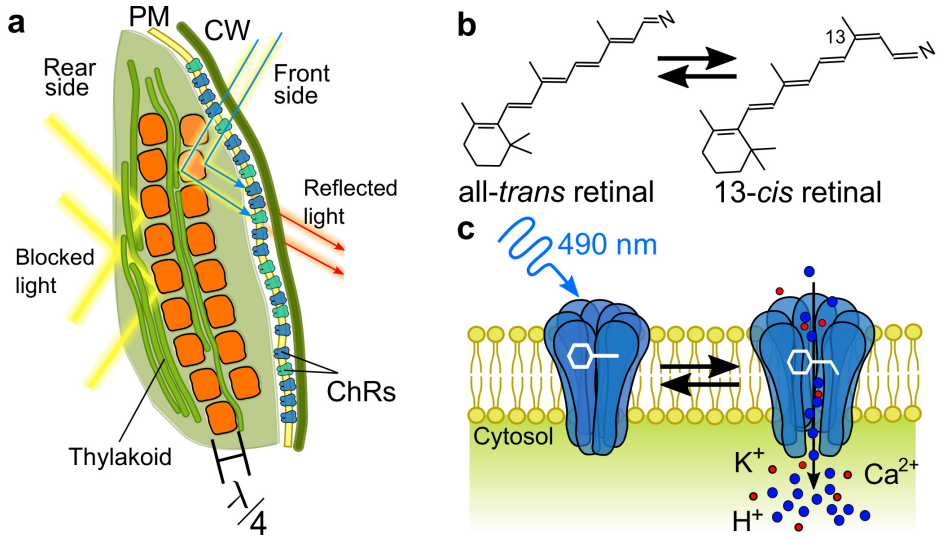


**Figure 2.8:** (a) Schematic of the eyespot of *C. reinhardtii*. The eyespot contains orange carotenoid granules that form layers that reflect incident light. The plasma membrane (PM), between the cell wall (CW) and the outermost carotenoid layer, contains the photoreceptors that mediate phototaxis (identified later as channelrhodopsins (ChRs) [171]). Light beams from the exterior of the cell are reflected by the front side of the granules and are directed to the photoreceptors, whereas the light from the inside of the cell is reflected, by the rear side of the granules, away from the photoreceptors. This gives the eyespot directional sensitivity, which helps to determine light intensity gradients. The thickness of the granular layers is ca. 100-120 nm, which corresponds to a quarter of the wavelength absorbed by the ChRs. This results in constructive interference of the reflected waves that reach the photoreceptors [56].(b) Isomerization of the retinal chromophore from all-*trans* (dark state) to 13-*cis* retinal under blue light is typical of microbial (type I) rhodopsins. (c) Schematic of the working principle of a transmembrane light-gated ion pump protein, whose retinal chromophore is sensitive to blue light (400-500 nm). The retinal undergoes isomerization, as shown in (b), which results in the opening of the protein channel and the generation of photocurrents driven by $Ca^{2+}$ and other physiologically-relevant ions. Inspired by [171, 172].

in lower organisms, like *Chlamydomonas*.

In the meantime, the use of electron microscopy approaches on microalgae to expose the ultrastructure of the eyespot, suggested that the photoreceptor involved in light perception of *C. reinhardtii* is located at the eyespot and associated to the overlying plasma membrane [169]. Finally, cumulative data gathered from electron microscopy studies, as well as the characteristics of the swimming motion of *Chlamydomonas*, was condensed in an elegant description that Foster and Smyth provided about the working principle of the eyespot [56], see Figure 2.8a. In essence, they proposed that the eyespot operates as a quarter-wave stack antenna, where incident light waves are reflected by the surfaces of the carotenoid vesicles. The reflection occurs in a way that they produce constructive interference in the overlying plasma membrane, where the photoreceptors are located [56, 170].

The dependence of phototaxis on the light wavelength (i.e., the action spectrum of phototaxis) shows that *C. reinhardtii* performs phototaxis under blue light, in a

way that its efficiency matches the absorption spectrum of a rhodopsin-type photoreceptor [56]. Later on, in a remarkable experiment, Foster successfully reconstituted the phototactic behavior of blind cells by administration of retinal chromophores. This demonstrated that a rhodopsin photoreceptor mediates phototaxis and the photophobic responses and, in addition to it, established *C. reinhardtii* as a model organism to study rhodopsin photoreceptors [173].

Subsequently, Hegemann *et al.* characterized the isomeric states of the retinal of wild-type *C. reinhardtii* and show that the dark form corresponds to an all-*trans* configuration, which isomerises to 13-*cis* retinal under blue light [174], see Fig. 2.8b. After determining rhodopsin as the photoreceptor underlying phototaxis, and the chemical structure of retinal in *Chlamydomonas*, research directions centered heavily in explaining the nature of the fast light-induced motility responses.

By the end of the 20th century, it was already known that the phototactic responses occurred fast and within 20 ms [175]. This suggested that the process connecting the stimulus of the photoreceptor and the start of the flagellar wave modulation could be mediated by fast ion transport. Harz and Hegemann showed, indeed, that light induces inward currents to the eyespot, which depend on the concentration of calcium ions, $Ca^{2+}$ [176]. Monovalent ions, such as $H^+$ [177] and $K^+$ [178] also contribute to photocurrents, provided high ionic concentrations, namely low pH or high extracellular potassium, respectively. As for the action spectrum of photocurrents, the maximum response in intensity occurs at a wavelength of 494 nm, which coincides with the absorption spectrum of rhodopsins [176]. This was then a univocal sign that photocurrents were rhodopsin-mediated.

The kinetics of photocurrents have also been characterized. They appear extremely fast, in less than 50 µs after light stimulus, peaked after 1-2 ms and decayed within 20 ms, depending on the light intensity [179, 180]. This ultra-fast appearance of photocurrents strongly suggested that the rhodopsin in *Chlamydomonas* should be directly coupled to an ion channel, see Figure 2.8c. Fortunately, the existence of light-gated ion-pump rhodopsins was already known, as two of such representatives, namely *bacteriorhodopsin* [181, 182] and *halorhodopsin* [183], were characterized in the 1970s and beginning of 1980s, respectively. Both rhodopsins established a novel category of its kind, known as microbial (type I) rhodopsins[14].

In *C. reinhardtii*, two rhodopsins were the first photoreceptors to be characterized. amino acid sequencing of the apoproteins showed that they resemble type II sensory rhodopsins, like the ones found in animals, and were named *chlamyopsins* (Cop) [184]. Both sensory rhodopsins, Cop1 and Cop2, were immunolocalized within

[14]Rhodopsins whose retinal chromophore isomerizes from all-*trans* to 13-*cis* upon light exposure, are classified as type I rhodopsins. These rhodopsins are typically found in archaea and bacteria, and hence are commonly known as microbial rhodopsins. In contrast, rhodopsins whose retinal chromophore isomerizes from 11-*cis* to all-*trans* are classified as type II rhodopsins. These are commonly found in the eyes of animals.

the eyespot area of *C. reinhardtii*. However, mutants with deficient production of Cop1 and Cop2 still exhibit phototaxis and photophobic responses, just like wild-type cells [185, 186]. This, finally, confirmed that Cop1 and Cop2 are incompatible with light-gated, microbial rhodopsins. Therefore, they were discarded as the photoreceptors controlling phototaxis and phobic responses in *Chlamydomonas*.

Up to date, a total of twelve Cop-proteins have been identified in *C. reinhardtii*. Yet, it is still a matter of debate whether Cop1 and Cop2 should be categorized as opsins (even if their sequence is analog to animal rhodopsins) since they are different from the rest of the opsins discovered in *Chlamydomonas*, which are membrane proteins that operate as light-gated ion pumps [187]. Since the role played by Cop1 and Cop2 in *Chlamydomonas* is still completely unclear in the present, I will not discuss them further. Therefore, I present the relevant literature on the remaining opsins in the following sections.

### Channelrhodopsins

After Cop1 and Cop2 were ruled out as the photoreceptors controlling phototactic responses, three independent research groups discovered novel DNA sequences in a genome database of *Chlamydomonas*. The sequences encoded two opsins, with a molecular weight of 76 kD, that partially resembled bacteriorhodopsin [175, 188, 189]. The genes in the database were named Cop3 and Cop4, and are commonly referred to as *channelrhodopsin-1* (ChR1) and *channelrhodopsin-2* (ChR2)[15], respectively [175]. The names come from the fact that Cop3 and Cop4 were expected to function as ion channels, precisely because of their structural homology to microbial rhodopsins and the fast appearance of photocurrents. Many of the initial studies performed in ChRs aimed to characterize such fast photocurrents, in order to confirm the light-gated nature of the photoreceptors.

Using electrophysiological methods [190] and RNA interference to modify the synthesis of ChRs, it was shown that ChR1-deficient cells exhibited weaker and delayed photocurrents, whereas ChR2-deficient cells exhibited stronger and faster currents [188]. This suggested that ChR1 and ChR2 mediate fast and slow components of the photocurrents, respectively. In addition, characterization of the action spectrum of photocurrents showed that ChR1-enriched cells exhibit highest photocurrent amplitudes at around 500 nm, whereas ChR2-enriched cells show a peak in sensitivity at 470 nm [188].

The extent to which phototaxis is controlled by ChR1 or ChR2 was just elucidated recently with the development of modern gene-targeting techniques, such as

[15] In the literature, the Cop3 and Cop4 photoreceptors have been initially referred to as: *Chlamydomonas sensory rhodopsins A and B* (CSRA and CSRB) [188], as well as *archaeal-type Chlamydomonas opsin 1 and 2* (Acop1 and Acop2) [189].

CRISPR/Cas9[16] [42]. *C. reinhardtii* cells that completely lack ChR2 were shown to have an action spectrum for phototaxis that is indistinguishable from the one of the WT strain. This confirmed that ChR1 is the dominant photoreceptor for phototaxis, with a response that peaks at 495 nm. Additionally, phototactic behavior is completely disrupted when both genes encoding for ChR1 and ChR2 are erased from the *C. reinhardtii* genome. This result completes previous ones, obtained by electrophysiological methods, in which cells with lower expression of any of the ChRs presented impaired phobic responses [188].

The ion-transporting nature of ChRs was confirmed by electrophysiological experiments carried out by Nagel *et al.*, first in ChR1 [192] and then in ChR2 [193]. The results show that ChR1 has high selectivity for $H^+$ and presents high conductivity in acidified medium, which confirmed that ChR1 is a light-gated proton channel [192]. Further characterization of the photocurrents of ChR1 in alkaline medium show that it also conducts $K^+$ and $Na^+$ [194]. As for ChR2, it was shown to transport the physiologically-relevant ions: $Ca^{2+}$, $K^+$ and even $Na^+$ [193]. Light stimulation with 10 ns pulses of 440 nm induces ultra-fast photocurrents within 200 µs or faster, which is a strong sign that ChR2 is an actual light-gated voltage ion [193]. These results helped to establish ChRs as the first ion channels with an intrinsic light-activated switch in *Chlamydomonas*.

After two decades of extensive study, ChRs have become the most well-characterized photoreceptors in *C. reinhardtii*. Yet, the development of more sophisticated visualization- and gene-editing techniques have provided even more insights on ChRs and their biological roles in *Chlamydomonas*. For instance, novel immunolocalization techniques have revealed that IFT trains transport ChR1 between the eyespot and the flagella with circadian-dependent dynamics [195]. A more recent example is the combined use of CRISPR/Cas9-generated, single ChR-mutants (i.e. deletion of one of the ChRs) with point mutations in the non-deleted ChR, aimed to explore further aspects of its ion conductivity in *Chlamydomonas*. Baidukova *et al.*, showed recently that strains with altered cation selectivity present a 100-fold lower photosensitivity [196]. In mutants with anion-conducting ChR2, phototaxis is completely disrupted, which revealed the importance of cation selectivity in the accuracy of phototactic motility of *C. reinhardtii*.

The knowledge gathered from the characterization of the molecular structure and the photocurrents of ChRs has lead to the development of a revolutionary field of neuroscience, called *optogenetics* [197]. In this field, methods from genetics are used to incorporate light-gated channels in specific cells within living tissues, aiming to control precise cellular functions [198]. The field emerged from the works of Peter Hegemann and Georg Nagel, who foresaw the potential of ChR2 to generate mem-

[16]CRISPR/Cas 9 stands for Clustered Regularly Interspaced Short Palindromic Repeats and associated protein 9 [191].

brane depolarization using light in different sorts of cells [193]. Subsequently, the functionality of ChR2 was demonstrated in different neural systems by Deisseroth and others, which marked the start of optogenetics [171]. After almost 20 years since its foundation, optogenetic tools have elucidated several principles underlying the function of nervous systems [197]. In the future, it is expected to provide therapeutic solutions to nervous-related problems, such as visual blindness, as well as neuropsychiatric and neurodegenerative diseases [197].

### Histidine kinase rhodopsins

The rhodopsins addressed so far, namely ChR1 and ChR2, are structurally characterized for having a single domain, which transports ions and propagates electric signals by membrane depolarization under blue light. In addition to these single-domain rhodopsins, the genome of *C. reinhardtii* was found to produce a novel type of opsin photoreceptors that, initially, had escaped identification. This new type of photoreceptors contains multiple domains that are similar to the ones found in proteins with enzymatic functions. Therefore, the novel opsins are part of a group of photoreceptors known as *enzymerhodopsins* [199].

In *C. reinhardtii*, three enzymerhodopsins were discovered initially and were identified as Cop5, Cop6, and Cop7 [172]. Later on, five opsins were added, namely Cop8 up to Cop12 [42, 195]. From genomic analysis, these photoreceptors were predicted to be large proteins, with the rhodopsin sensory domain linked to a chain of functional domains, namely a histidine kinase[17] (HK), a response regulator[18] (RR) and, in some cases, a cyclase domain[19]. Photoreceptors whose sensory domain is coupled to a transducer domain that activates a RR are known as *two-component systems* (TCS or 2c). In our present discussion, the coupling of rhodopsin to HK and the RR forms a TCS. In addition to this, the TCS can be coupled to a cyclase domain, which could be either guanylyl- or adenylyl cyclase (GC or AC, respectively), in which case, the photoreceptor is termed *2c-cyclase opsins* (2c-Cyclops) [187]. Despite of the complex terminology, all photoreceptors comprising Cop5 to Cop12 are simply referred to as *histidine kinase rhodopsins* (HKRs).

HKR1,2 (i.e. Cop5,6) and HKR4 to HKR6 (i.e. Cop8 to Cop10) are known to be 2c-Cyclops, as they contain either a GC- or AC domain [42]. This suggests that these HKRs catalyze intracellular signaling molecules known as *cyclic adenosine monophosphate* (cAMP) and *cyclic guanosine monophosphate* (cGMP), which are involved in multiple physiological responses in many organisms [203]. Particularly

[17] Histidine kinases are enzymes involved in intracellular signal transduction reactions elicited by environmental stimuli [200].

[18] A response regulator is a protein domain that binds to a histidine kinase to induce enzymatic responses within the cell [201].

[19] A cyclase is an enzyme that catalyzes chemical reactions that produce organic cyclic compounds. These compounds mediate important physiological responses within a cell [202].

in *C. reinhardtii*, cAMP is involved in signaling reactions that induce mating [204], whereas both cAMP and cGMP seem to participate in phototaxis [205].

Little is known about most of the HKRs in *Chlamydomonas*. Indeed, only the sensory domain of HKR1 has been spectroscopically studied *in vitro*, whereas its enzymatic functions still remain elusive. The rhodopsin domain of HKR1 shows two stable forms that are interconverted by light [206–208]. One state, termed Rh-UV, absorbs UV-A with maximum at 380 nm and is photoconverted to the blue state Rh-bl. This state, which absorbs efficiently at 490 nm, can be converted back to the Rh-UV state under blue light. Immunolocalization shows that HKR1 is located in the eyespot region of *C. reinhardtii* [206], although no involvement in phototaxis has been confirmed. HKR4 (Cop8) has also been immunolocalized in the eyespot of *C. reinhardtii*, and has been found to migrate to the eyespot, in a light-dependent way, via IFT [195].

The most recently studied enzymerhodopsin in *C. reinhardtii* is HKR2 (Cop6). Tian *et al.*, characterized the structure of HKR2 and demonstrated that it has an effector domain with guanylyl cyclase activity [187]. Specifically, it was shown that the production of cGMP by HKR2 is inhibited by light and it also depends on ATP in the dark. Therefore, HKR2 is proposed as a light-inhibited photoreceptor, whose enzymatic activity is achieved by cGMP produced in darkness. Finally, the rhodopsin domain of HKR2 seems to be composed by 8-transmembrane (8TM) structures, which is different to the typical 7TM structures found in microbial rhodopsins [187]. From this, it is proposed that 2c-Cyclops correspond to a novel sort of microbial rhodopsins, whose light-controlled enzymatic functions could provide promising applications in optogenetical settings [187].

### 2.4.2 Cryptochromes

At the end of the 19th century, Charles Darwin and his son, Francis, studied the directed growth of plants towards a source of light, known as *phototropism* [209]. They noticed that the photosensitivity of growing shoots lies in their uppermost light-exposed portion. If only this section was covered with an opaque foil, the plant would keep growing straight up, undeflected by the sunlight. The German botanist, Julius von Sachs, aware of Darwin's studies and the significance that light has in the behavior of plants, obtained a rough action spectrum and noted that blue light mediated the bending response [210]. The results from Sachs were not a surprise to botanists in the 1900s. Extensive research on lower plants and fungi, also known as *cryptogamic plants*[20], already showed that blue light controls many tropic and morphogenic responses. That is, blue light controls how plants move and

[20]Cryptogams are plants or plant-like organisms that reproduce by spores. They do not produce flowers or seeds, therefore their reproductive method remained hidden or *cryptic* to botanists. Examples of cryptogamic plants are algae, fern, mosses and fungi.

grow.

Although the action spectrum of phototropic responses suggested the involvement of a group of pigments known as *flavoproteins* [211], the actual chromophore mediating such responses remained undiscovered for more than a century. Thus, inspired by the hidden nature of the chromophore and its involvement in the light-mediated responses studied in cryptogamic plants, the provisional name, *cryptochrome* (CRY), seemed more appropriate rather than the longer and unspecific *blue-light photoreceptor* [212]. The first CRY was finally discovered in 1993, in a mutation of the land plant *Arabidopsis thaliana* [213], and one part of its amino acid sequence was found to resemble a well-characterized family of blue-light photoreceptors, called *photolyases* [214].

Photolyases are blue-light photoreceptors that mediate the reparation of UV-damaged DNA, also known as *photoreactivation* [215]. Their protein structure consists of one main domain, where they bind to the chromophore *flavin adenine dinucleotide* (FAD), which absorbs UV light with maxima at around 280 and 380 nm; and blue light at around 480 nm [216]. Curiously, photolyases bind a second chromophore, usually 5,10-methenyltetrahydrofolate (MTHF) [217] or, less commonly, 8-hydroxy-5-deazariboflavin (8HDF) [218]. The second chromophore acts as a light-harvesting antenna that is not essential for activity, but serves as a booster for efficiency of DNA repair under limited light conditions.

The structure of photolyases is evolutionary inherited by the CRY photoreceptors. Indeed, all CRYs possess two protein domains, see Figure 2.9. First, a domain that extends from the N-terminal, known as *photolyase homology region* (PHR), which is highly conserved among all cryptochromes and photolyases and serves as the chromophore-docking region [219]. Second, a domain known as carboxyl-terminal extension (C-extension), which is non-existent in photolyases, but, in CRYs, exhibits variable length and is poorly conserved, even among CRYs of the same species [219].

The biochemical properties and the photochemistry of FAD have been characterized, *in vitro*, relatively recently, and it shows that FAD can be in different redox states: oxidized ($FAD_{ox}$); semireduced as an anion radical ($FAD^{\bullet -}$); semireduced neutral radical ($FADH^{\bullet}$); and fully reduced ($FADH^{-}$) [219]. Each state allows CRY photoreceptors to pick up specific regions of the UV-visible spectrum, see Figure 2.10a. Furthermore, each state induces a conformational change of the apoprotein, thus resulting in a plethora of different signaling responses, such as the control of light-mediated growth and flowering in plants [213], entrainment of the circadian clock in animals [222] and even magnetoreception in migratory birds [223, 224].

I will mention basic features of the photochemistry of CRYs found in *C. reinhardtii*. The complexity of the photochemical processes, however, will not be discussed in the present work. For a more detailed discussion on the photocycle of CRYs and their biological function in organisms other than *Chlamydomonas*, I refer

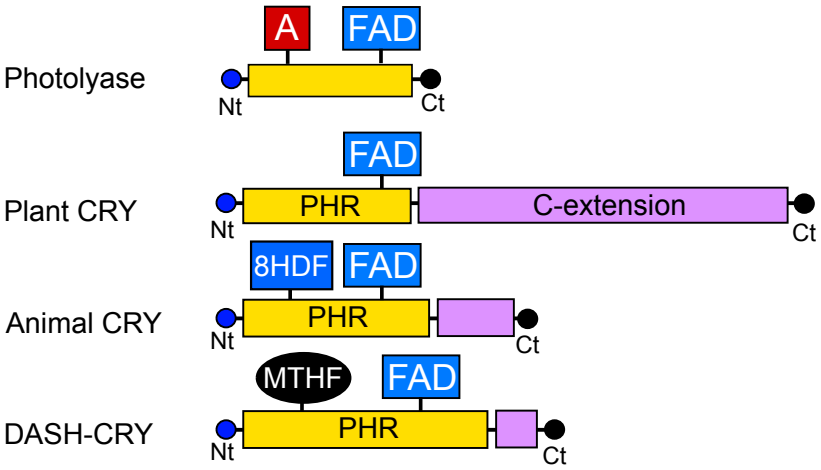


**Figure 2.9:** Topological representation of protein domains. The extension of each domain gives an idea of the length of the polypeptide chain forming it. DNA-repairing photolyases have only one domain, delimited by the classic N-terminal (Nt) and the C-terminal (Ct). The photolyase domain binds to the chromophore flavin adenine dinucleotide (FAD) and can also bind a light-harvesting molecule or *antenna chromophore* (A). The antenna can be typically 5,10-methenyltetrahydrofolate (MTHF) or 8-hydroxy-5-deazariboflavin (8HDF). The structure of cryptchromes (CRY) consists of two domains. First, a photolyase homology region (PHR) which is highly similar to the photolyase domain. Second, a C-extension of variable length and that is poorly conserved. The three different types of cryptochromes in *C. reinhardtii*, namely plant-, animal-, and DASH-CRY, are depicted. All of them bind FAD as chromophore, but, additionally, animal cryptochrome contains a binding site for 8HDF [220], whereas DASH-CRY has a binding site for MTHF [221].

the interested reader to the review written by Chaves *et al.* [219].

In the following, I will then discuss the current state of knowledge of the four CRYs discovered in *C. reinhardtii*. A comprehensive review has been written recently by Petersen *et al.*, from which I summarize the experimental results related to CRYs redox states and their biological functions in *Chlamydomonas*.

### Plant cryptochrome

The first CRY identified in *C. reinhardtii*, formerly named *Chlamydomonas photolyase homologue 1* (CPH1) [227], was found to have almost 50% of homology to higher-plant CRYs. Its physical and chemical properties identify CPH1 as a plant cryptochrome (pCRY).

In *C. reinhardtii* pCRY accumulates during the cell's dark phase, as part of a protein complex, and reaches its maximum accumulation before the start of the day phase [228]. Then, pCRY is degraded rapidly during the start of the day phase [228, 229]. This light-induced proteolysis is mediated by blue and, surprisingly, red light, in a way that does not depend on the cell's circadian rhythm [229]. Further analysis suggests that the degradation is controlled by the proteasome[21] pathway, as the use of a proteasome inhibitor interrupts the light-induced proteolysis [229].

[21] A proteasome is a protein complex that degrades proteins that are damaged or not needed.

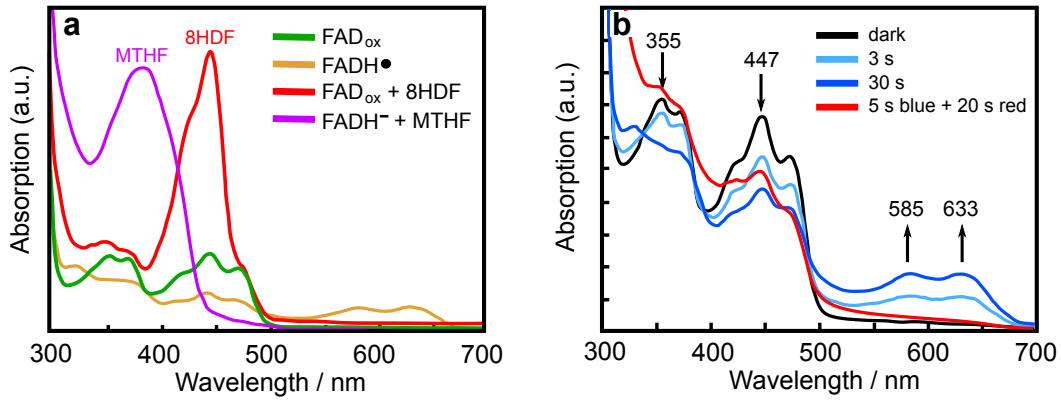


**Figure 2.10:** (a) *In vitro* absorption spectra of FAD states found typically in *C. reinhardtii*. Under physiological conditions, FAD is synthesized in the oxidized state, $FAD_{ox}$. Depending on the light exposure, $FAD_{ox}$ can also be found in the semireduced neutral radical state, $FADH^{\bullet}$. The absorption efficiency of CRYs can be upgraded if they bind to a second chromophore. In *C. reinhardtii*, for instance, animal CRY can bind 8HDF, which enhances absorption in the blue range. Also DASH-CRYs can bind MTHF, which boosts absorption in the UV-A band and stabilizes the fully reduced FAD state, $FADH^-$. Plot adapted from [225]. The MTHF spectrum was added from [221]. (b) Different FAD redox states, depending on light exposure. When $FAD_{ox}$ is exposed to blue light for several seconds, the main absorption bands in the UV and blue regions are weakened, whereas an absorption band rises in the 500-700 nm range. This indicates the appearance of the $FADH^{\bullet}$ state. If $FADH^{\bullet}$ is further illuminated with red light, the yellow-to-red absorption band is lost, but the oxidized state is not recovered. This is characteristic of the $FADH^-$ state. Adapted from [226].

The mechanism of degradation is believed to require phosphorylation[22] [229], which depends on blue-light and does not depend on the presence of the C-extension, as confirmed by *in vitro* assays [230].

The photochemistry of pCRY has also been studied *in vitro*. Heterologous expression (in *E. coli*) of the light-sensitive domain has been used to produce the chromophore and to purify it. Then, its absorption spectrum has been determined using UV-visible spectroscopy. The results show that the pCRY-associated chromophore, FAD, presents two absorption bands, one in the 300-400 nm region and the other in the 400-500 nm region, which is a typical feature of oxidized FAD ($FAD_{ox}$) [230], see Figure 2.10. Blue light induces the formation of the neutral radical $FADH^{\bullet}$, which is considered the signaling state, and presents a broad absorption band between 500-600 nm, see Figure 2.10b. The *in vitro* recovery of $FAD_{ox}$ is established in the dark, in the order of minutes, and it is strongly delayed by the addition of ATP or the absence of oxygen [230].

Recently, the biological functions of pCRY in *C. reinhardtii* have been addressed. Müller *et al.* reported that pCRY is involved in the circadian clock of *C. rein-*

[22]Phosphorylation is the binding of a phosphate group ($PO_4{}^{3-}$) to a molecule. It is a common reaction in biological systems, where it controls the functions of proteins and regulates signaling pathways.

*hardtii*. This was confirmed by measurements of the rhythmic photoaccumulation, also known as rhythm of phototaxis [231], of cells that have been previously entrained in a 12h/12h light/dark cycle [228]. The results show that circadian-adapted wild-type cells maintain a rhythm of phototaxis with a periodicity of 24 h, even after several days in darkness. In contrast, pCRY-deficient *C. reinhardtii* mutants exhibit a phase shift of 3 h after 5 days in darkness, followed by arrhythmicity.

Experiments probing the level of pCRY at different stages of the *C. reinhardtii* life cycle show that pCRY is almost vanished in pregametes and in gametes [228]. Nevertheless, dark incubation of vegetative cells in nitrogen-deficient medium and in the presence of a proteasome inhibitor resulted in pregametes with accumulated pCRY [228]. This means that the degradation of pCRY, in the case of dark-adapted pregametic cells, is not induced by light, but by nitrogen starvation [228]. This corroborates that pCRY degradation is proteasome-dependent and also extends previous results obtained in vegetative cells, in which the proteasome inhibitor halts light-induced pCRY proteolysis [229].

In the case of *C. reinhardtii* gametes, transcriptional levels have found to be naturally lower than pregametes, although not in a significant way [228]. Thus, even when mRNA encoding pCRY is still being transcribed in gametes, pCRY does not show accumulation in this life stage [228]. Furthermore, pCRY does not even accumulate when gametes are exposed to a proteasome inhibitor. This suggests a gamete-specific degradation pathway that is yet to be revealed.

Finally, it has been found that pCRY strongly affects gametogenesis by acting as an inhibitor of both the mating ability, under light exposure, and the loss of mating ability in light-deprived gametes [228]. During the process of light-dependent germination, however, pCRY acts as a positive regulator, where it seems to act in conjunction with phototropin.

### Animal cryptochrome

In the previous section, it was mentioned that red light also participates in the degradation of pCRY [229]. This is a surprising evidence because the genome of *C. reinhardtii* does not encode red-light sensitive photoreceptors [41]. Nevertheless, several experiments show that red light is involved in physiological responses related to the resetting of the circadian clock in *C. reinhardtii* [232, 233]. Therefore, explorations of sequence homology were conducted in *C. reinhardtii* in order to find photoreceptors that were known to influence circadian clock components, such as the CRYs found in higher animals [219]. One putative CRY was identified and, since it does not have homology to any plant CRYs, it was simply named *animal cryptochrome* (aCRY).

Precise sequencing shows that aCRY has homology with a special type of pho-

tolyases, namely (6-4)-photolyases[23]. Elucidation of the aCRY crystal structure, and experiments probing its biological function *in vivo*, indicate that aCRY is indeed a bifunctional photoreceptor [220, 225]. This means that aCRY controls biological functions in *C. reinhardtii* but, unlike pCRY, it can also repair UV-damaged DNA. This gives rise to rich spatiotemporal dynamics of the photoreceptor within the cells.

Accumulation of aCRY varies along the day-night cycle and the sexual cycle, and its localization also depends on its function. In vegetative cells, for instance, aCRY is abundant in the cell nucleus during subjective day, where it is thought to provide photoreactivation of UV-damaged DNA [220]. At the beginning of subjective night, aCRY levels are 2-fold reduced, and it is spread over the cell body as a soluble protein in the cytosol [226, 234]. As for pregametes, gametes and even early zygotes, soluble aCRY is strongly reduced and it was never found in the nucleus of the cells. However, membrane-bound aCRY is more abundant in sexual *C. reinhardtii* cells, and is also present in vegetative cells [235].

As opposed to pCRY, aCRY is not degraded by light exposure during the day phase. This has allowed the realization of reliable experiments, both *in vivo* and *in vitro*, to probe aCRY's biological functions in *Chlamydomonas*. Much more is known about the roles of aCRY in *Chlamydomonas* thanks to the fruitful collaboration of the research groups of Maria Mittag and Tilman Kottke [236].

*In vivo* experiments, comparing vegetative wild-type *Chlamydomonas* cells with aCRY-deficient mutants, show that aCRY mediates the expression of genes encoding proteins involved in metabolic processes of the photosynthetic apparatus under blue and red light [226]. Furthermore, aCRY regulates transcription levels of genes associated to the circadian clock. This regulation is equally mediated by blue and red light [226].

With respect to the life cycle of *C. reinhardtii*, aCRY and pCRY regulate the transition steps of this cycle. The transition from pregametes to gametes, which is mediated by blue light, is negatively regulated by aCRY and pCRY. On the contrary, during germination, both CRYs act as positive regulators in the development of this step [235]. During germination, blue-light regulated processes are found to be dominant, yet red light contributes significantly as well [235].

The diversity of aCRY-controlled biological functions over a broad range of effective wavelengths has motivated a precise characterization of the redox states of its FAD chromophore [220, 225, 237, 238]. Similarly as in pCRY, $FAD_{ox}$ in aCRY is converted to the neutral radical, $FADH^{\bullet}$, under blue light; see Figure 2.10b. However, this state can remain stable *in vivo*, because, in contrast to pCRY, aCRY can bind a second chromophore, namely 8HDF, which has a strong absorption peak at

[23]Photolyases repair two types of UV-induced DNA damage. The most common one is cyclobutane pyrimidine dimer (CPD) and, to a less extent, (6-4) photoproducts. Depending on the type of DNA damage that is repaired, photolyases can be classified as CPD photolyases or as (6-4)-photolyases, respectively.

around 448 nm (see Figure 2.10a) and prolongs the lifetime of the neutral state [225]. This suggests that the dark state in aCRY is $FAD^{\bullet}$ rather than $FAD_{ox}$, which explains how aCRY can act as a red-light sensitive photoreceptor in *C. reinhardtii*.

### DASH cryptochromes

After the discovery of plant and animal CRYs, a third group of photoreceptors with similar characteristics were discovered in the cyanobacterium *Synechocystis*, as well as in the bacterium *Vibrio cholerae*. Further analysis of the genes encoding this new CRYs showed sequence homology to *Arabidopsis* and other species [239]. The cryptochrome was named DASH-CRY (*Drosophila, Arabidopsis, Synechocystis, Human* and it was known to retain photolyase activity. The genome of *C. reinhardtii* encodes two DASH-CRYs, namely DASH-CRY1 and DASH-CRY2 [226]. However, only DASH-CRY1 has been studied so far.

Diurnal expression of DASH-CRY1 reaches its maximum at subjective noon and it is lowest at the start of the dark phase, when the expression is 3-fold reduced [221]. Immunoblots performed on crude subcellular extracts of *C. reinhardtii* suggest that DASH-CRY1 is localized in the chloroplast [221]. Cells of a mutant strain with inhibited DASH-CRY1 exhibit a dark green coloration, which corresponds to increased levels of chlorophyll a and b, as well as carotenoids. This suggests an integration of DASH-CRY1 in the thylakoid membranes, which is in agreement with immunoblots [221]. To confirm this feature, it was necessary to find differences at a smaller scale.

Electron microscopy studies shows that the ultrastructure of thylakoid membranes is significantly different between the WT and the DASH-CRY1 deletion mutant, where the latter one presents hyper-stacking of thylakoid layers [221]. Thus, DASH-CRY1 is presumed to act as a negative regulator for the overexpression of photosynthetic pigments, balancing therefore the photosynthetic machinery.

The study of the *in vitro* photoreduction of DASH-CRY1 reveals that its absorption spectrum has a single broad maximum in the UV-A range, at 388 nm. This indicates association to the antenna chromophore MTHF, see Figure 2.10a. The purified FAD from DASH-CRY is present in its fully reduced state $FADH^{-}$ and it was found to be very stable as it fully converts to the $FAD_{ox}$ state after several days in complete darkness [221]. Therefore, $FADH^{-}$ is presumed to be the *in vivo* functional state of DASH-CRY1 in *C. reinhardtii*. The stability of this redox state promotes algal growth under UV-A exposure and optimizes the photosynthetic machinery [221].

As a general summary, the different CRYs found in *C. reinhardtii* mediate a plethora of biological processes allowing the cells to keep track of time and control different aspects of its physiology. This is achieved under a range of wavelengths that span most of the sunlight spectrum. Multiple functionalities are provided by

the different redox states in which the FAD chromophore can exist. Depending on the biological processes to be mediated, some redox states are more suitable and, thus, association to a light-harvesting antenna is required for stabilization and to produce a sustained functionality of the photoreceptor. Each redox state is sensitive to UV and blue light, however, the existence of the semireduced neutral radical state makes CRYs the only red-light sensitive photoreceptor found in *C. reinhardtii*. Consequently, the expanded range of photosensitivities provided by CRYs is revealed in their broad effective action spectrum.

### 2.4.3 Phototropin

A few years after the discovery of the first cryptochrome in the plant *Arabidopsis*, a new gene encoding for a blue-light photoreceptor was discovered in the same organism [240]. As this photoreceptor was directly implicated in phototropism it was trivially called *phototropin* [241, 242]. Together with rhodopsins, phototropins are one of the most well-studied photoreceptors. Their molecular structure and biological relevance have been extensively studied, though mainly in land plants.

Phototropin has two distinct molecular structures. First, a C-terminal extension composed by a *serine/threonine kinase* domain [243], which propagates the light signal within the cell [244]. Second, the N-terminal that binds two light-sensitive domains, named LOV1 and LOV2, where LOV stands after *Light-Oxygen-Voltage*[24] [242, 245]. The structural characteristics and properties of both the sensitive and the functional domains have been studied.

LOV1 and LOV2 domains bind the chromophore flavin mononucleotide (FMN), whose photochemistry has been well characterized, even a decade before phototropin was proven to be a blue-light photoreceptor [243, 246]. In darkness, LOV domains bind FMN noncovalently, forming a spectral-sensitive domain that absorbs blue light with a peak at 447 nm ($LOV_{447}$) [242, 247, 248]. Subsequent illumination with blue light generates a species that absorbs near UV-A with a maximum at 390 nm ($LOV_{390}$). This state reverses back to $LOV_{447}$ in darkness and it is considered the signaling state of phototropin [246, 248].

The crystal structure of the LOV domains is almost identical between them, and their arrangement in the dark and illuminated states has been elucidated as well [249, 250]. From photochemical data, it is deduced that the activity of phototropin stems mainly from the properties of the LOV2 domain, which is considered a light switch that controls the activity of the functional C-extension domain under blue light [243, 251]. This kinase domain undergoes then local and global conformational changes [252] that trigger the signaling within the cell and exploit the functionality of phototropin [244].

[24]The LOV domains are related to a group of proteins that are regulated by external signals, namely light (L), oxygen (O) and voltage (V); hence the acronym.

Although the structure and photochemistry of phototropin are highly conserved between algae and plants [253], the functional properties have diverged immensely between these lineages. In the following, I will address the biological functions of phototropin in *C. reinhardtii*, which contains only one gene that encodes phototropin (PHOT) [254].

In *C. reihardtii*, PHOT mediates several processes that control photosynthesis and the activation of photoprotection mechanisms. For example, PHOT regulates the expression of genes encoding photosynthetic proteins, such as chlorophyll and carotenoids, and also apoproteins of the light-harvesting complex (LHC) [255], which convert light into energy. Furthermore, this conversion is accompanied by the synthesis of protein effectors that sustain energy-dissipative processes and are positively regulated by PHOT. This, in the end, prevents the damaging of the cell's photosynthetic machinery under high light intensity [256, 257].

Another important aspect controlled by PHOT is the sexual life cycle in *C. reinhardtii* [258]. Huang *et al.*, determined that blue light is used by PHOT to control: gamete formation, sustain of mating competence, and zygote germination. Furthermore, PHOT is also presumed to mediate the reactivation of flagellar agglutinins (i.e. mating competence) in dark-inactivated *C. reinhardtii* gametes. Fractionation studies and immunolocalization show that PHOT is present, not only in the cell body but also in the outer microtubules of the flagella [259]. There, PHOT might promote flagellar agglutinin activation under blue light [260] in gametes, given that reactivation does not involve protein synthesis.

Complementary to the work of Huang *et al.*, the studies of Ermilova and Zalutskaya show the role that PHOT plays in the chemotactic behavior during the sexual life cycle of *C. reinhardtii* [144]. Using PHOT-deficient mutants, they showed that the disruption of chemotaxis towards ammonium is delayed with respect to the WT strain [261]. Two things were concluded from these results. First, PHOT is a negative regulator of chemotaxis in *C. reinhardtii*. Second, PHOT enhances sexual reproduction, since it helps the cells to find light-exposed areas that are suitable for mating and avoids them from detouring to darker places in search of nitrogen sources.

Finally, besides the regulation of chemotactic behavior, PHOT also has an influence on phototaxis. The use of PHOT-deleted mutants and complementary strains with overexpression of the PHOT kinase domain have revealed a link between PHOT and the regulation of eyespot size in *C. reinhardtii* [262]. Both intensity and prolonged exposure to blue light affect the size of the eyespot via PHOT, and overexpression of the PHOT functional domain causes a strong decrease of ChR1, the main photoreceptor controlling phototaxis. This suggests that PHOT desensitizes the eyespot when blue light irradiation is increased, which makes PHOT an essential component for long-term light adaptation for phototaxis.

### 2.4.4 Ultraviolet Resistance Locus 8

As mentioned in Section 2.3.4, all photoactive organisms exposed to sunlight have evolved photoprotective mechanisms to overcome the dangers of UV radiation. Photoprotection under light stress is, indeed, seen in every branch of the evolutionary tree containing photosynthetic forms of life [263]. Therefore, it is expected that some features of the photoprotective machinery are conserved over the course of evolution.

*Nonphotochemical quenching* (NPQ) is an important photoprotective mechanism that is carried out by *energy-dependent nonphotochemical quenching* (qE), which is a process that dissipates light energy as heat. The effective activation of qE is mediated by a photoreceptor called *Ultraviolet Resistance Locus 8* (UVR8), which absorbs in the range 280-315 nm (i.e., UV-B light), and is highly conserved in higher plants [264]. As NPQ is also a common mechanism in every photosynthetic machinery, a search for UV-B perception was conducted in the model organism *C. reinhardtii*.

*C. reinhardtii* was found to codify for a UVR8, which is similar to the one found in higher plants [265]. The mechanism of function is quite conserved [266] and is characterized by the perception of UV-B by a triad of tryptophan residues[25] [265, 267], instead of the usual photoreceptive chromophore [268].

Upon UV-B exposure, UVR8 is known to mediate the transcription levels of genes that control the photosynthetic system of *C. reinhardtii* [265]. This promotes the accumulation of specific proteins in the light-harvesting complex (LHC) that contribute to qE [269] and the protection of photosynthetis, which, in turn, results in light acclimation to UV-B in *C. reinhardtii*.

The elucidation of the mechanism of photoprotection, via UVR8, in *C. reinhardtii* is of high importance given that the underlying processes are well conserved between algae and plants [266], as demonstrated by the fact that UVR8 of *C. reinhardtii* reconstitutes photoprotection in plants with disrupted UVR8 production [265]. This provides another reason to use *Chlamydomonas* as a model organism to study other phenomena underlying acclimation responses induced by UV-B in photosynthetic organisms.

## 2.5 Light-switchable flagellar adhesion

In Section 2.3.3, I described the two main types of motility performed by *C. reinhardtii*: swimming and gliding. During swimming motility, the flagella beat and propel the cell through the liquid environment. When the cell performs gliding

[25] In the context of biochemistry, a residue is a monomer within a biopolymeric chain. In the present discussion, tryptophan is an amino acid in the polypeptide chain conforming the UVR8 photoreceptor.

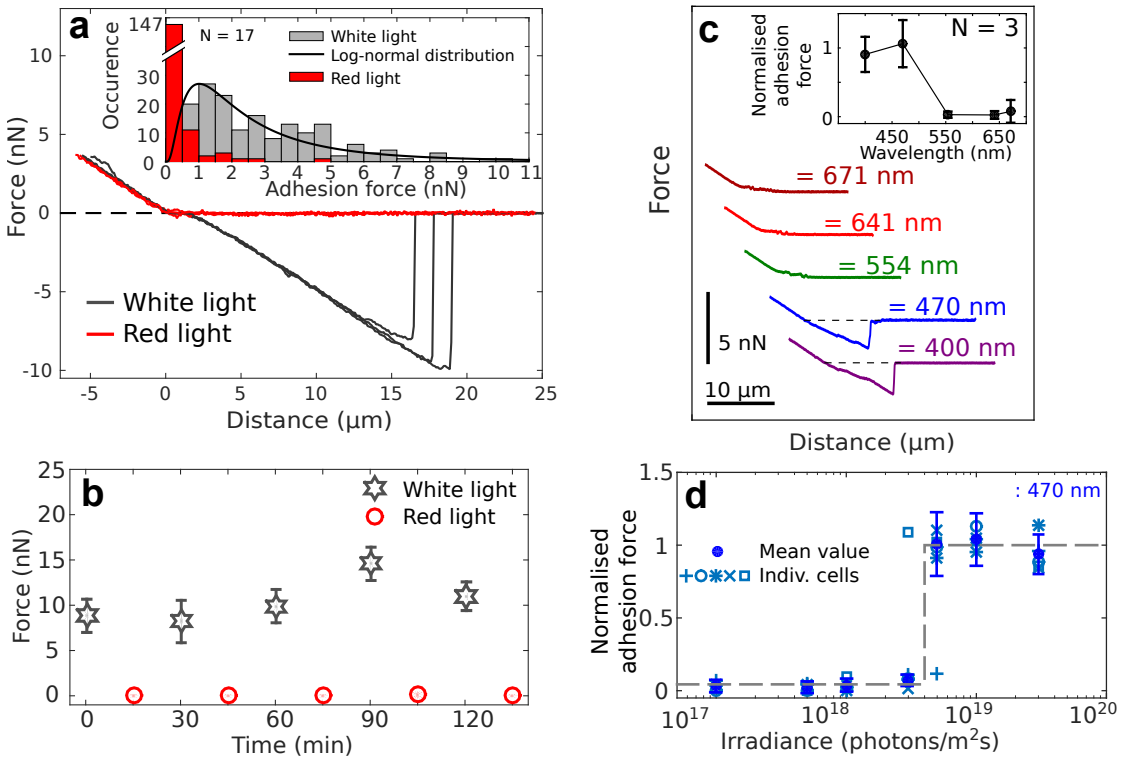


**Figure 2.11:** (a) Force–distance curves of the same cell in white (dark grey lines) and red light (red lines). The inset shows the distribution of adhesion forces for 17 different cells in red and white light. (b) Adhesion force measurements for the same cell in alternating light conditions. (c) Force–distance curves for the same cell using different illumination wavelengths. Cells exclusively adhere in blue and violet light. The inset shows the mean adhesion force of different cells (N = 3), normalized to their adhesion force in blue light (470 nm). (d) Identification of an intensity threshold at $2 - 5 \cdot 10^{18}$ photons·m$^{-2}$·s$^{-1}$ in blue light (470 nm). Dashed line represents a guide to the eye. Reproduced from [40].

motility, the flagella interact with a solid substrate and orient in an angle of 180° with respect to each other. The force transduction is achieved by the interaction of FMG-1B with dynein-1b molecular motors. Despite that there are several studies that describe either of the two types of motility of *C. reinhardtii*, little is known about how the cells transition between one type and the other.

Recently, Kreis *et al.* discovered that the transition between swimming and gliding motility is mediated by light [40]. By measuring the flagellar adhesion of individual cells to a solid substrate, using an *in vivo* micropipette approach (see Chapter 3), they found that when a solid substrate is brought into contact with a cell that is exposed to white light, the flagella adhere to the substrate. However, the measured flagellar adhesion under red light is almost zero, indicating that the flagella do not adhere under red light, see Figure 2.11a. Furthermore, for the exact same cell, the cycle of measurements can be repeated and the results obtained are similar. The flagellar adhesion is, therefore, switched on by white light, whereas it is switched off by red light, see Fig. 2.11b. Hence, this phenotype of *C. reinhardtii* has been termed light-switchable adhesion.

To identify under which wavelength the flagellar adhesion is switched on, a color discrimination was also performed. It was determined that blue and violet light trigger the flagellar adhesion, whereas green light and longer wavelengths do not, see Fig. 2.11c. Furthermore, in order for the flagellar adhesiveness to be switched on, a light intensity threshold must be overcome, see Fig. 2.11d.

Further micropipette experiments, again by Kreis *et al.*, demonstrate that the mechanism underlying light-switchable adhesion is mostly substrate-unspecific [39]. By measuring the flagellar adhesion of single cells to different model substrates, they studied the role of hydrophobicity, van der Waals forces, and electrostatic interactions. The results show that the flagellar adhesion is significantly stronger in negatively-charged surfaces. This indicates that the mechanism of adhesion is likely of electrostatic nature.

Measurements of the flagellar adhesion have also been done using *C. reinhardtii* mutants with altered N-glycan composition [82]. In other words, the chemical composition of the N-glycosylated structures shown in Fig. 2.3 has been modified at the gene level. Xu *et al.* showed that altered N-glycan structures attached to flagellar proteins, namely FMG-1B, lowers the flagella adhesion force. This suggests that the mere interaction of FMG-1B glycoproteins with the substrate is not sufficient to establish adhesion. Thus, N-glycosylation is expected to play a crucial role in the flagellar adhesiveness.

The timescale associated to light-switchable adhesion has also been measured at a single-cell level, using time-resolved micropipette force measurements [40]. In these experiments, the solid substrate is placed at a fixed distance from the cell body, where it can barely be touched by the flagella. Subsequently, when the cell is illuminated with white light, the tip of one or both flagella adhere to the substrate and pull the cell body towards it until the cell reaches the gliding configuration. This process is termed *autoadhesion*, see Figure 2.12a. The average delay time of the onset of autoadhesion is around 10 s, as obtained from the deflection signal of the pipette. Nevertheless, the onset of the active approach can take up to several tens of seconds, see Fig. 2.12b.

Although the seminal studies on the light-activated flagellar adhesion of *C. reinhardtii* give valuable insights, several aspects remain to be elucidated. First, the flagellar adhesiveness is switched on under blue light, which suggests that, at least, one blue-light photoreceptor must mediate this phenotype. The identification of the photoreceptors is of high interest as it should provide hints that explain the mechanisms underlying light-switchable adhesion in *Chlamydomonas*. Secondly, it is not clear how the transition from *non-adhesive* to *adhesive* occurs in the flagella. Proteolysis experiments, in which individual *C. reinhardtii* cells were exposed to enzymatic protein degradation by pronase under white light, show that the adhesion force decays to almost zero after 2 hours of pronase exposure [40]. However,

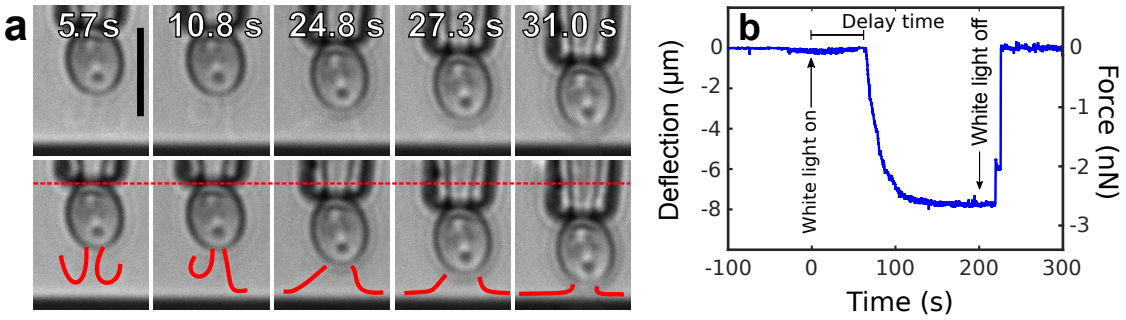


**Figure 2.12:** (a) Optical micrographs showing autoadhesion of a *C. reinhardtii* cell that is held by a micropipette (scale bar: 10 µm). The micrographs correspond to different time points after switching to white light, and the bottom row includes guidelines to the eye (solid: flagella; dashed: initial position of the micropipette). When the cell is exposed to white light, the tip of one or both flagella adheres to the substrate in around 10 s. Subsequently, the flagella pull the cell body towards the substrate until the gliding configuration is attained. Adapted from [40]. (b) Micropipette deflection signal of the cell's auto-attachment. Once the white light is turned off the flagella detach from the substrate. Adapted from [40].

when 2 hours of cultivation with pronase is done under red light, all the cells exhibit adhesion immediately after exposure to white light.

These results indicate that the adhesion-promoting proteins do not surround the flagellar membrane under red light. Kreis *et al.* suggest that a redistribution of proteins is the possible mechanism for light-switchable flagellar adhesiveness [40]. Lastly, as the kinetic aspects of light-switchable adhesion have been studied at the single-cell level using cells that are fixed to a pipette, experiments at the population level, using free-swimming cells, should give insights on the influence of phototaxis on the transition from the swimming to the light-induced surface-associated state. Therefore, a characterization of the kinetics of light-switchable adhesion, at the population level, illustrates the first step towards biofilm formation in *Chlamydomonas*. Consequently, such characterization in microalgae extends the scope of biofilm studies, which have mainly been conducted using bacterial suspensions [270–272].

# Chapter 3

# Materials and Methods

The focus of my doctoral studies was to identify the blue-light photoreceptor regulating light-switchable flagellar adhesion of *C. reinhardtii* to surfaces. To achieve this, I use two experimental complementary techniques. On the one hand, micropipette force spectroscopy, which allows to quantify and compare flagellar adhesion forces of WT and genetically modified *C. reinhardtii* cells. On the other hand, adsorption experiments, which allow to quantify the kinetics of adsorption and desorption of *C.reinhardtii* on the population level. The latter technique can also be used, in a complementary way, to determine whether the cells exhibit light-switchable adhesion or not. In the following sections, I introduce the *C. reinhardtii* cultures that I used during my doctoral thesis, and then I describe each technique and the protocols that I used to acquire and analyze the experimental data.

## 3.1 Cultivation of *C. reinhardtii* strains

All the experiments presented in this thesis were performed using the unicellular microalga *C. reinhardtii* in the vegetative state. In order to determine the photoreceptor regulating light-switchable adhesion, the experiments performed required the comparison of adhesion forces and the adsorption kinetics of genetically modified mutant strains with their corresponding wild-type (WT) strain. In the following, I present the different strains that were used in this thesis and the protocol of cultivation for their subsequent use in force measurements and adsorption experiments.

### 3.1.1 Wild-type strains

All the WT strains used in this thesis were kindly provided by the Culture Collection of Algae (SAG) of the University of Göttingen. Experiments were performed using the WT strain labeled SAG11-32b, but also experiments using the WT strain SAG 73.72 are presented and will be explicitly mentioned.

Cultures in agar were stored in an incubator (IPP110ecoplus with cold white

light module 6500K; Memmert GmbH+Co. KG, Schwabach, Germany), which was set to operate in a 12h/12h day/night cycle. The storage temperature during the day phase was set to 16°C, whereas in the night phase, the temperature was 14°C.

Cultures in agar that were required for experiments, were transferred to Tris-Acetate-Phosphate (TAP) liquid medium (Gibco™; Thermo Fisher Scientific, Waltham, Massachusetts, USA). TAP medium has a well-established composition[1] with pH 7, which is optimized for the cultivation of *Chlamydomonas*.

The transfer from agar to fresh TAP medium was performed under a sterile flow bench (Herasafe 2025 1.5; Thermo Electron LED GmbH, Langenselbold, Germany) to guarantee the growth of axenic cultures[2]. All the glass flasks, each containing 50 mL of culture medium were sterilized in an autoclave (Laboklav 25-M; SHP Steriltechnik AG, Detzel Schloss, Germany) at 121°C for one hour and then transferred to the sterile bench for disinfection under UV light, also for one hour. Once the temperature of the fresh medium was in equilibrium with the temperature in the laboratory (set to 24°C), a small piece of agar culture was inoculated and transferred to the liquid medium.

The liquid cultures were kept inside an incubator (IPP260Plus with cold white light module 6500K; Memmert GmbH+Co. KG, Schwabach, Germany), which was set to operate in a 12h/12h day/night cycle. This led to synchronized cultures, where almost all the cells were in a vegetative growth stage during the day phase and divided by mitosis during the night phase, see Fig. 2.4. The daytime temperature of the incubator was set to 24°C, with a light intensity between $2 \cdot 10^{19}$ photons$\cdot$m$^{-2}\cdot$s$^{-1}$ (at the center of the compartment) and $6 \cdot 10^{20}$ photons$\cdot$m$^{-2} \cdot$ s$^{-1}$ directly next to the light source. During the dark phase, the temperature was lowered to 22°C and the intensity was completely reduced to darkness.

All experiments presented in this thesis used cells from cultures in logarithmic growth phase. The cells were harvested in the daytime, during the growth phase on the third day after incubation. Some experiments required the harvesting of cells before the start of the day phase. These, so-called, *early-morning experiments* are properly described in Section 3.3.5.

### 3.1.2 Photoreceptor-deletion mutant strains

Mutant strains correspond to *C. reinhardtii* cells that were genetically modified via CRISPR/Cas9 to target specific genes encoding for a blue-light photoreceptor. All the photoreceptor-deletion mutants were generated in the lab of Prof. Peter Hegemann, at the Humboldt University, Berlin, Germany. All mutant strains presented

[1] The composition stated by the manufacturer can be found here: https://www.thermofisher.com/de/en/home/technical-resources/media-formulation.354.html (retrieved on 24.05.23).

[2] Axenic cultures only contain a single strain of a certain species. In other words, the cultures do not contain other organisms or other strains of the same species.

in this work were produced from the WT strain SAG11-32b, unless otherwise stated, and were cultivated in liquid medium following the exact same protocol as for the WT strains described above.

The photoreceptor-deletion mutants used in this thesis comprised single- and double knockouts, for which one or two gene sequences encoding blue-light photoreceptors are respectively targeted. The terminology used to distinguish mutant strains consists of labeling the name of the strain with a "*delta*" ($\Delta$), followed by the abbreviation of the photoreceptor that is deleted. For instance, $\Delta$ChR1 denotes a mutant *C. reinhardtii* strain that lacks the photoreceptor ChR1. More information about the blue-light sensitive photoreceptors in *C. reinhardtii* can be found in Sec. 2.4. Below, I provide a list of the different photoreceptor-deletion mutants used in the present work:

- **Channelrhodopsin deletion mutants**: $\Delta$ChR1, $\Delta$ChR2 and $\Delta$ChR1,2.
- **Phototropin deletion mutant**: $\Delta$PHOT.
- **Cryptochrome deletion mutants**: $\Delta$pCRY, $\Delta$aCRY and $\Delta$aCry-$\Delta$pCRY.
- **Histidine-kinase rhodopsin deletion mutant**: $\Delta$HKR2 (or $\Delta$Cop6).

## 3.2 Micropipette Force Spectroscopy

Micropipettes are thin, hollow glass capillaries, with diameters that can be as big as hundreds of micrometers and as small as a few micrometers. Besides their common usage in the life sciences as specimen holders [176] and as injection needles [273], micropipettes have been used also as force sensors [274–276].

Micropipette force spectroscopy (MFS) is a technique that employs the deflection of the most flexible portion of a micropipette, namely the *cantilever*, to measure the mechanical properties of living organisms [277]. The deflection of the cantilever is recorded by brightfield microscopy, which allows for simultaneous visualization of the force sensor, the specimen (e.g., a cell), and its surroundings.

In the present study, a micropipette force sensor is used to hold a *C. reinhardtii* cell by a small suction pressure, so that the flagella are exposed to the surrounding liquid medium. In the following, I describe the protocol for manufacturing micropipette force sensors that are suitable for measuring the flagellar adhesion of single *C. reinhardtii* cells to a solid substrate. The experimental setup and protocols for such measurements have been previously developed by Dr. Marcin M. Makowski and Dr. Christian T. Kreis [40]. A detailed description of the setup and protocols for data acquisition and analysis is presented in the doctoral thesis of Dr. Kreis [278].

### 3.2.1 Manufacturing the force sensors

The manufacturing of micropipettes consists of two main steps. First, the fabrication of micropipettes from glass capillaries. Second, the fabrication of the desired force sensor by bending the micropipette in a way such that it enables a proper visualization of the specimen (i.e., a single *C. reinhardtii* cell) and the deflection of the cantilever during data acquisition.

Borosilicate glass capillaries with an initial outer diameter of 1 mm and inner diameter of 0.75 mm (TW100-6; World Precision Instruments, Inc., Sarasota, Florida, USA) were used to fabricate micropipette force sensors. The glass capillaries were clamped in a micropipette puller (P-1000; Sutter Instrument, Novato, California, USA), such that their center portion was surrounded by a heating filament. Subsequently, heat was applied at the center portion of the capillary, and, as the glass started to melt, the extremes of the capillary were pulled apart. This results in a tapered, straight micropipette of a few micrometers in diameter and several centimeters in length. The tip of the micropipette was cut to obtain a straight opening with an inner diameter of around 10 µm, which is compatible with the size of *C. reinhardtii* cells. Fire polishing was applied to the tip of the micropipette to smooth the edges. Then, the straight micropipette was bent using a microforge (MF-900 or MF2; Narishige Group, Tokyo, Japan) to manufacture the force sensor needed.

In order to visualize the deflection of the cantilever, as well as the *Chlamydomonas* cell as it interacts with a solid substrate, the shape of the force sensor requires two bends of the micropipette, in a way such that the cantilever and the cell are in the same plane. To bend the micropipette, tension is applied by pushing the pipette against a metal wire. Then the glass is locally heated at the place where the bending is needed. The heat melts the glass and releases the tension, which generates the formation of a kink, see Fig. 3.1a.

The bending procedure is repeated until the kink forms an angle of around 90°. This first bent portion of the micropipette constitutes the nozzle, which is perpendicular to the cantilever and has a typical length of 200 µm, see Fig. 3.1b. Subsequently, a second kink was forged in a similar way and at a distance of around 1-3 cm from the first bending. The larger length ensures that the cantilever is flexible enough to be deflected by flagellar adhesion forces. After the two bends of the micropipette were completed, the force sensor consisted of three parts that are shown in Fig. 3.1c:

1. The **glass capillary support**, which is the most rigid portion of the micropipette and serves as a robust structural component that can be easily handled or clamped to the experimental setup.

2. The **cantilever**, which typically has a length of 1-3 cm and serves as the force sensor due to its flexibility.

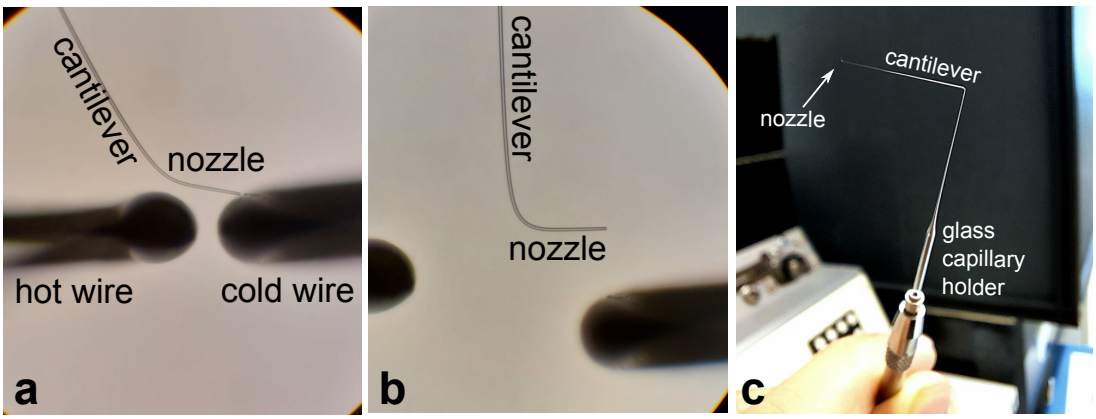


**Figure 3.1:** Manufacturing of a micropipette force sensor. (a) A hot filament locally heats the glass, whereas the cold wire exerts tension on it. The heat softens the glass and the tension is released, which results in a kink that forms the nozzle (about 200 µm in length) and the cantilever. (b) The cantilever, which is the most flexible structure of the force sensor, is perpendicular to the nozzle. (c) A second kink of 90° is made at a distance of approximately 1-3 cm away from the nozzle, which sets the length of the cantilever. In the end, the micropipette force sensor is composed of three parts: the nozzle, the cantilever, and the glass capillary support.

3. The **nozzle**, which has a typical length of 200 µm. It is perpendicular to the cantilever and corresponds to the tip of the micropipette, where a *Chlamydomonas* cell can be held by suction.

### 3.2.2 Calibration of the force sensor

The next step after the fabrication of the force sensor is the calibration procedure, which relates the deflection of the cantilever to the force applied to it. In order to deflect the cantilever, the micropipette is first filled with deionized water using a syringe that is connected to the glass capillary support via a plastic tube, see Fig. 3.2a. Afterwards, the micropipette is mounted on the microscope setup (IX-83; Olympus Corporation, Tokyo, Japan) with the glass capillary support parallel to the direction of the gravitational force, as depicted in Fig. 3.2b. This configuration is preferred as the adhesion forces applied to the cantilever are in the same direction as the nozzle. An active vibration isolation table (Halcyonics i4-large; Accurion GmbH, Göttingen, Germany) is used to dampen the vibrations that may disturb the cantilever during the calibration procedure. Subsequently, water is run through the pipette to generate a droplet at the opening of the nozzle and a series of optical micrographs are recorded at 10 fps using a scientific camera (Grashopper GS3-U3-41C6M-C; FLIR Integrated Imaging Solutions Inc., Richmond, BC, Canada)[3]

[3]Optical micrographs in this thesis correspond to greyscale, digital images. The camera sensor has a pixel depth of 8 bits, which allows for 256 different pixel intensity values, ranging from zero (black) up to 255 (white). The sensor has a resolution of 4.2 Megapixels and a pixel size of $5.5 \times 5.5$ µm$^2$.

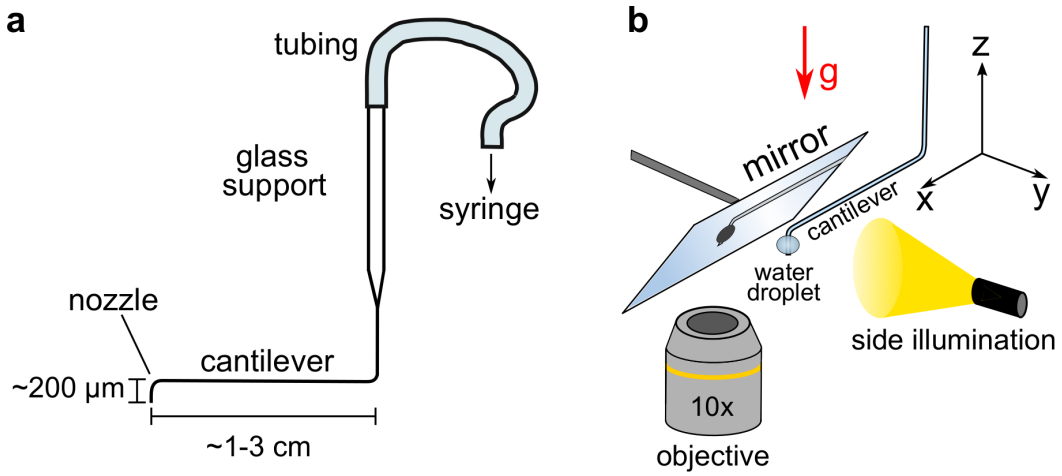


**Figure 3.2:** (a) A syringe connected to the micropipette's glass support via plastic tubing is used to fill the force sensor with water for subsequent calibration and force measurements. The different parts of the force sensor are shown, as well as the approximate lengths of the cantilever and the nozzle. (b) Setup for the calibration of the force sensor. The nozzle and capillary support are in the same orientation as the gravitational acceleration $g$. Side illumination is set so that the shadow of the force sensor is projected in a mirror tilted at 45° with respect to the nozzle. The image on the mirror is reflected to the objective lens of 10x magnification, and then to a camera (not shown). The cantilever is deflected by the weight of a water droplet generated at the nozzle by running water through the pipette. The deflection is correlated with the weight of the water droplet to obtain the spring constant of the cantilever, see Section 3.2.2.

using an objective lens of 10x magnification. As the volume of the hanging droplet is increased, so does the cantilever deflection. The force acting on the cantilever corresponds then to the gravitational force, i.e., the weight of the water droplet. This method of calibration is known as the *added mass method* and was used for all the calibrations of micropipette force sensors used in the present work[4].

All the image analysis routines used to calibrate the force sensor involved the use of custom-made MATLAB code[5] that reads images obtained by high-resolution optical microscopy. The routine is described in the following sections.

### Autocorrelation analysis to determine the cantilever's deflection

In order to relate the deflection of the cantilever with the force applied to it, the deflection of the cantilever has to be computationally determined from the optical micrographs. To do this, a pixel intensity profile over a cross-sectional line, perpendicular to the cantilever, is extracted for each recorded optical micrograph, see Fig. 3.3a. The pixel intensity profile captured by the selected cross section has a characteristic shape, as shown in Fig. 3.3b. As the position of the cross-section line remains fixed for every image, the spatial shift of the cantilever's position yields

[4] An alternative calibration procedure can be done by using a reference cantilever, which has been previously calibrated by the added mass method [277].

[5] The code was originally written by Dr. Marcin M. Makowski and Dr. C. T. Kreis [278].

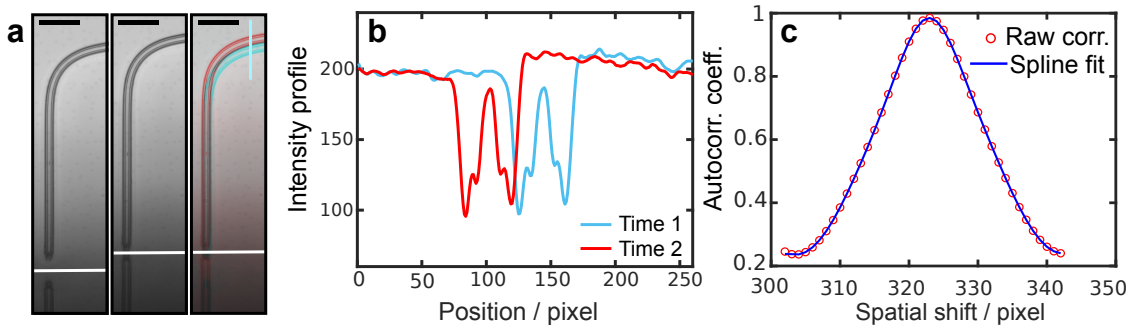


**Figure 3.3:** (a) Left and middle images are optical micrographs illustrating the deflection of the cantilever at two different instants. The dashed line indicates the position of a solid substrate that deflects the cantilever. The image on the right shows the vertical cross-sectional line where the autocorrelation analysis is performed. (b) Intensity profiles extracted from the cross-sectional line shown in the rightmost image in (a). The cantilever profiles correspond to the two timepoints recorded. (c) Autocorrelation analysis of the cantilever intensity profile as a function of the spatial shift.

a displacement of the pixel intensity profile over the cross-sectional line. Profiles corresponding to two different instants of time in the calibration procedure are then analyzed by autocorrelation. This technique spatially shifts one of the intensity profiles with respect to the other. In doing so, the autocorrelation returns a measure of the overlap of the profiles as a function of their positions within the line of acquisition.

In other words, the pixel distance between the profiles is determined. Then the raw correlation value is associated with the match between the two compared profiles, with larger values indicating a better match. The set of all correlation values is collected and forms a discrete raw correlation function whose maximum indicates the exact overlap of the profiles. The raw correlation is then fitted with a non-parametric *spline* function, whose maximum yields a sub-pixel resolution [278], see Fig. 3.3c.

### Calculation of volume of the water droplet

The second step to obtain a calibration of the micropipette force sensor is to determine the weight of the water droplet that hangs from the nozzle and deflects the cantilever, see Fig. 3.4a. To achieve this, the contour of the water droplet's two-dimensional projection in the optical micrographs was obtained. Assuming that the droplet has rotational symmetry, its volume was determined by rotating the two-dimensional projection around the axis of symmetry of the droplet. The symmetry axis is defined as the line parallel to the direction of the gravitational force and goes through the centroid of the droplet's projected area. The size of the water droplet was smaller than the capillary length of water ($\approx$ 2.7 mm at 25°C [279]). Thus, gravitational forces are not expected to deform the droplets substantially.

Finally, since an estimated volume of the water droplet is associated to a specific

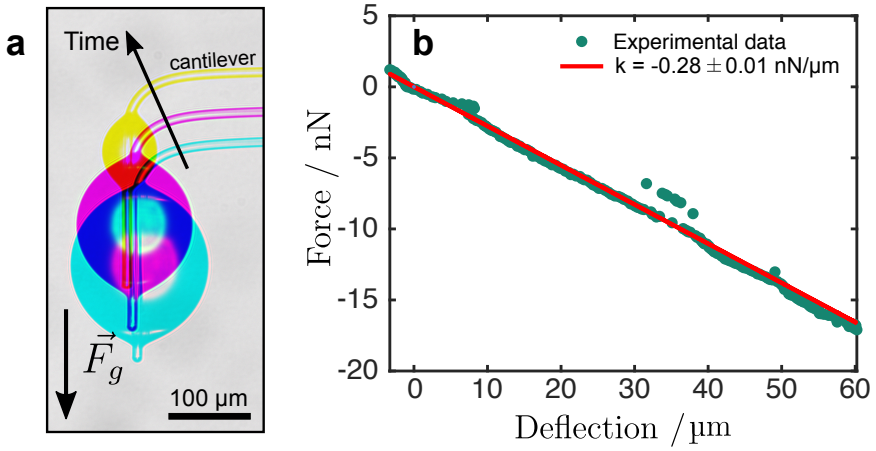


**Figure 3.4:** (a) Optical micrographs of the calibration of a micropipette force sensor. The gravitational force $F_g$ of the water droplet deflects the cantilever. (b) Force and deflection extracted from optical micrographs as seen in (a). The cantilever deflection scales linearly with the weight of the droplet.

position of the cantilever in each optical micrograph, a force-deflection graph can be obtained, see Fig. 3.4b. As the magnitude of the force $F$ applied to the cantilever increases linearly with its deflection $\Delta x$, then the micropipette force sensor can be considered to operate in the linear elastic regime. Therefore, the cantilever can be considered as a Hookean spring, with a constant $k$ given by Hooke's law:

$$F = -k\Delta x \tag{3.1}$$

For the calibration of the pipettes used in this work, I always made sure to minimize the error in the estimated volume of the water droplet. To achieve this, I discarded calibration runs in which the water droplet was not spherically symmetric, for instance, as a result of the droplet being pinned between the nozzle and the cantilever. Furthermore, I took five independent calibration runs with the same cantilever, which yielded a total error below 10%, while the error of the individual measurements was usually around 7%. The micropipettes obtained in this work exhibit a typical cantilever spring constant $k$ that ranges between 0.2-1.5 nN/µm. Together with the sub-pixel resolution given by the autocorrelation analysis of the cantilever's deflection, the spring constants enabled a force resolution in the order of tens of pN [277, 278]. The accuracy in the deflection of the cantilever is better than 100 nm, which yields a force resolution of less than 50 pN for a spring constant of 0.5 nN/µm, which is comparable to the resolution achieved with single-cell adhesion studies using atomic force microscopy [278].

### 3.2.3 Experimental setup

As described in Sec. 3.2, MFS relies on high-resolution optical microscopy to determine the deflection of the micropipette's cantilever. Thus, the whole micropipette

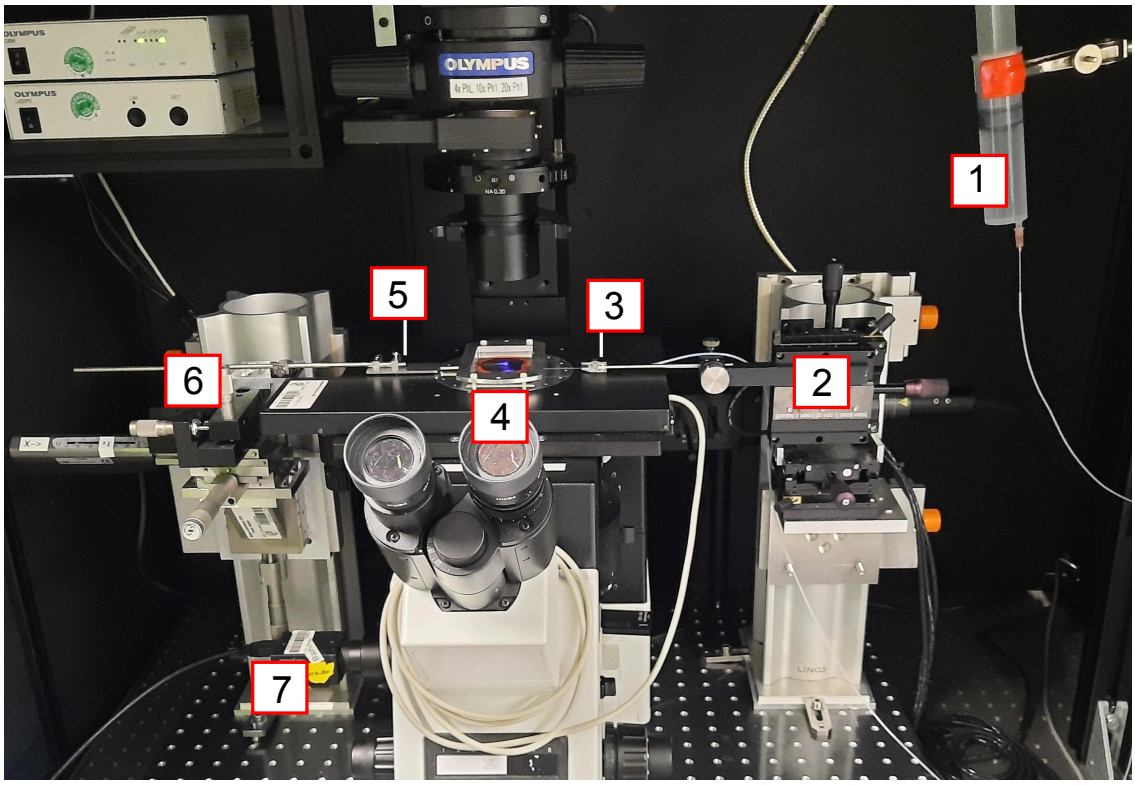


**Figure 3.5:** Picture of the experimental setup used to measure flagellar forces of single *C. reinhardtii* cells. The setup consists of an inverted microscope mounted on an active anti-vibration table. The entire setup is enclosed within a black box to guarantee controlled light conditions. (1) Syringe connected to the capillary support to create suction pressure. (2) Micromanipulator set to control the position of the force sensor. (3) Micropipette holder. (4) Liquid chamber; see Fig. 3.6. (5) Stainless steel substrate holder. (6) Set of linear stages to control the position of the substrate. (7) Scientific camera.

force spectroscopy setup is built around an optical microscope, as shown in Fig. 3.2.3. In order to perform *in vivo* measurements of the flagellar adhesion force of *C. reinhardtii* cells, a custom-built liquid chamber is mounted on the microscope stage[6]. As the MFS works with single cells, precision instruments are mounted on the setup to guarantee an accurate positioning of the micropipette force sensor and the solid substrate, which consisted in non-functionalized silicon wafers with thin $SiO_2$-layer[7] of 1.7 nm (Si-Mat, Kaufering, Germany). The position of the pipette's nozzle and the substrate are controlled by several micromanipulators.

To suppress any external vibrations that could disturb the cantilever during data acquisition and cause a premature rupture of the adhesive contacts between the microalga and the silicon substrate, the microscope and the micromanipulators are placed on an active anti-vibration table (Halcyonics i4-large; Accurion GmbH,

[6]Most of the components of the setup and the metallic frame of the liquid chamber were designed by Dr. Marcin M. Makowski and manufactured in the workshop of the Max Planck Institute for Dynamics and Self-Organization, Göttingen, Germany

[7]The wafer specifications are: type P/Bor, orientation $\langle 100 \rangle$, resistivity 1-20 $\Omega \cdot$ cm, unilateral polished.

Göttingen, Germany). The active dampening of the external vibrations of the setup reduces the noise level on the cantilever deflection by more than one order of magnitude[8] [278].

As the main objective of this thesis requires experiments under light-controlled conditions, the light exposure of *C. reinhardtii* cells was an important parameter. A black box was installed around the whole experimental setup and enclosed the anti-vibration table and the microscope. This box prevents the access of external light to the liquid chamber and enables the use of specific wavelengths during the experiments. The settings of the light conditions during the experiment are described in Section 3.2.4. In the following, I elaborate on the different components of the MFS experimental setup.

### Optical Microscope and Imaging system

This study employed two inverted microscopes (IX-73 and IX-83, Olympus Corporation, Tokyo, Japan). For the micropipette calibration, I used mostly the microscope IX-83 and for the micropipette force experiments I used the microscope IX-73. The cantilever deflection was monitored using brightfield optical imaging with long-distance objectives. For the calibration procedure, I typically used an objective of 10x magnification with an optical resolution of 0.3433 µm per camera pixel (pixel size is 5.5×5.5 µm$^2$). In the case of the MFS experiments, I used an objective with 20x magnification, with a resolution of 0.2736 µm per camera pixel.

The optical micrographs were recorded using scientific greyscale cameras. To visualize the cantilever's deflection during force-distance curves and during calibration, micrographs were taken at 10 frames per second (Grasshopper, GS3-U3-41C6M-C; FLIR Integrated Imaging Solutions Inc., Richmond, Canada).

### Liquid chamber

All micropipette force measurements were performed in aqueous solution in a custom-built liquid chamber, see Fig. 3.6. This chamber was filled with the undiluted liquid medium in which *Chlamydomonas* cells were cultured, see Sec. 3.1.

The liquid chamber consists of two glass slides, separated by two pieces of an O-ring, which were positioned so that there were two openings to introduce the substrate and the micropipette force sensor. For micropipette force measurements, the height of the liquid cell is 3.4 mm, which allowed the insertion of a substrate holder of 2 mm of height. The glass slides were fixed tightly with a custom-made metal frame made out of aluminum.

[8]The noise level of the cantilever deflection is defined as the standard deviation of the deflection signal, from its equilibrium position, when a *Chlamydomonas* cell is held by suction to the nozzle. The value of the deflection is typically of the order of 10-20 pN [278].

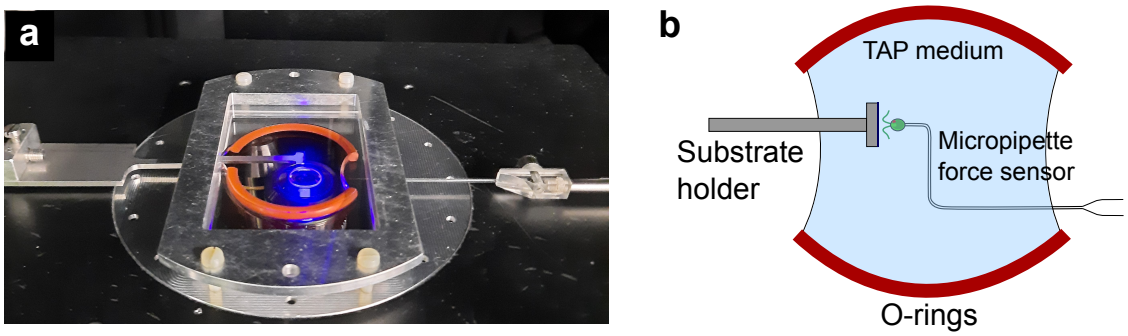


**Figure 3.6:** (a) A picture of the experimental chamber used for force-distance measurements. The substrate holder is introduced from the left, whereas the force sensor is introduced from the right-side opening of the chamber. (b) Illustration of the liquid chamber shown in (a). A *C. reinhardtii* cell being held by suction at the nozzle is depicted.

Before assembling the chamber, I rinsed the glass slides and O-rings with ethanol (CAS-64-17-5, ROTISOLV®, HPLC Grade, Purity (GC)≥ 99%; Carl Roth GmbH) and dried them with a stream of ultra-pure nitrogen. Subsequently, I placed the glass slide at the bottom metal frame and the two O-rings on top of the glass slide. The O-rings were placed at a distance of around 2 cm, so that the micropipette cantilever and the substrate holder could be inserted easily afterwards. Then, I closed the chamber with the top glass and the top frame, which was fixed to the bottom frame using screws. I mounted the chamber onto the microscope stage and then I carefully filled the chamber with 3 mL of Tris-Acetate-Phosphate liquid growth medium, such that no air bubbles were left inside the liquid chamber. Subsequently, I introduced around 1 mL of a *Chlamydomonas* cell suspension to the liquid chamber. The cell concentration inside the liquid chamber was not controlled. However, it was chosen to be small enough so that swimming cells inside the chamber do not disturb the experiment. The menisci of the aqueous medium at the openings of the liquid chamber were flattened as much as possible so that the silicon substrate and the force sensor could be introduced perpendicularly through the menisci. This guarantees that the cantilever deflection is solely due to flagellar adhesion forces and not external capillary forces that might deform the cantilever.

### Micromanipulators and linear actuators

Micromanipulators and linear stages are used to control the position of both the micropipette and the substrate. The micromanipulators (Burleigh PCS-5400; Thorlabs Inc., Newton, New Jersey, USA) consisted of a three-axis mechanical micromanipulator for coarse alignment, which can be adjusted manually, with an additional integrated piezoelectric-driven unit for fine alignment. According to the supplier, the piezoelectric alignment had an accuracy better than 120 nm without any backlash and low drift. This combination allows for precise handling and positioning of the micropipette's nozzle, which is crucial to correctly grab a *C. reinhardtii* cell

from the substrate in the correct orientation.

The position of the substrate was controlled by a motorized linear actuator (LTA-HS; Newport Corporation, Irvine, California, USA) that enables cyclic, approach-retraction motions of the solid substrate. During the measurements of the flagllar adhesion forces, the cantilever is kept stationary and the substrate is moved forwards or backwards relative to the cantilever. The linear actuator featured a position repeatability of approximately 200 nm, an average hysteresis of about 500 nm, and a backlash of about 7 µm (inferred from the control reports of the actuators [278]). The substrate motion was controlled with the graphical user interface provided by the supplier of the linear stages. Additional multi-axis tilt platforms (M-36; Newport Corporation, Irvine, California, USA) enabled parallel alignment between the cantilever and the substrate, which yields a perpendicular alignment between the cantilever's nozzle and the surface of the substrate.

### 3.2.4 Micropipette force measurements

Micropipette force measurements were performed to quantify the flagellar adhesion of individual *C. reinhardtii* cells to a solid substrate. In the following sections, I describe the experimental protocol that I followed to do the force measurements, and I introduce the relevant experimental parameters.

#### Introducing the solid substrate and force sensor in the liquid chamber

After mounting the liquid chamber in the microscope stage, as described in Section 3.2.3, I cleaned the silicon substrate in an ultrasonic bath of HPLC-grade ethanol for one minute and dried it with a stream of ultra-pure nitrogen. The substrate is mounted in a stainless steel substrate holder. Subsequently, I clamped the substrate holder to the linear stages of the MFS setup and introduced the silicon substrate to the liquid chamber. Afterwards, I applied the same cleaning procedure to a calibrated micropipette force sensor and then connected the glass capillary support to a 50 mL syringe via a plastic tube. Both the tube and the syringe contain deonized water, and I looked that no bubbles were inside the tubing and the micropipette. Thereafter, I fixed the micropipette to a metal holder and positioned the capillary support onto the micromanipulator stage in the setup. Finally, I carefully introduced the micropipette into the liquid chamber.

#### Positioning the cantilever and the solid substrate

Once the solid substrate and the cantilever were inside the chamber, the pipette is brought very close to the surface of the silicon substrate. Then the substrate and cantilever are manually aligned so that the micropipette nozzle is perpendicular to the substrate surface. This minimized lateral shear forces during the experiment and

guaranteed that the adhesion forces of the cell are measured normal to the substrate. After the alignment was finished, I set up the imaging of the cantilever and the data analysis MATLAB code for a real-time view of the cantilever's deflection during the force-distance cycles.

### Holding a cell at the pipette's nozzle using suction

The force spectroscopy experiments require holding an individual, living (and motile) *C. reinhardtii* cell to the cantilever's nozzle in a controlled orientation. The orientation of the cell is crucial as only the flagella exhibit adhesion [40]. The cell's orientation can be controlled by monitoring the flagella beating or, in the case of the present work, by identifying the pyrenoid (see Fig. 2.1) at the anterior part of the cell body.

To grab a cell at the nozzle of the force sensor using suction, I took advantage of the light-switchable adhesion exhibited by *C. reinhardtii*. I exposed the cells to blue light (see Sec. 3.2.4), at an intensity of $1 \cdot 10^{19}$ photons$\cdot$m$^{-2} \cdot$ s$^{-1}$, and waited for a few minutes until I observed several cells adhered by their flagella to the solid substrate. Adhered cells are indeed in the gliding configuration (see Fig. 2.6) and, therefore, exhibit the right orientation needed to probe their flagellar adhesion.

I selected a cell whose cell body was about the same size as the inner diameter of the pipette's nozzle. Then, using the micromanipulators, I brought the pipette's nozzle very close to the cell body and positioned it such that the cell was in contact with the opening of the nozzle. Subsequently, I generated a small suction pressure at the opening of the nozzle, by lowering the syringe below the level of the micropipette force sensor. The hydrostatic pressure difference between the extremes of the tubing is given by $\Delta p = \rho g \Delta h$, where $g$ is the gravitational acceleration, $\rho$ is the density of water and $\Delta h$ is the difference in height between the positions of the micropipette and the syringe. The suction pressure, which was kept constant in all the measurements performed for a single cell, immobilized the cell body in a way that the flagella are facing the solid substrate. At the end of the force measurements, I checked that the cell was still alive. For this, I lowered the suction pressure and released the cell, which indicated that it was still motile. All the measurements considered in this work were obtained from cells that could swim after the measurements, which indicated that the cell was alive during the whole experiment.

### Find the contact position and the limits of the substrate motion

The final preparation step for data acquisition involves establishing the position at which the substrate comes into contact with the cell body, i.e., the contact position. I assessed this by approaching the solid substrate towards the cell, with a speed of 1 µm/s, until I observed a slight deflection of the cantilever. The cells are known

to be stiffer than the micropipette's cantilever, which ensured that cells are not significantly deformed during the experiments. The contact position is then defined as the *zero-distance position* at which the cell came into contact with the substrate and entered the repulsive force regime in the coordinate system of the force-distance curves, see Fig. 3.8a.

### Setting up the light conditions

As described in Sec. 2.3.3, the motility of *C. reinhardtii* cells is strongly affected by the light conditions (e.g. phototaxis). Therefore, controlled illumination settings were established. During data acquisition, *C. reinhardtii* cells were illuminated with different wavelengths using bandpass interference filters. The filters are classified by the center wavelength of transmission and the width at which the transmission is reduced to 50%, which corresponds to the *full width at half maximum* (FWHM). For instance, 671/10 nm corresponds to a filter that is transparent to red light of wavelength 671 nm and that has a FWHM of 10 nm.

The microscopes used for force-distance experiments have a built-in halogen lamp (JC 12V100W; Olympus Corporation, Tokyo, Japan). The power supplied to the lamp was calibrated depending on the filter used. The calibration was made using a power meter (PM100D with sensor S130C; Thorlabs Inc., Newton, New Jersey, USA).

For experiments in which the *C. reinhardtii* cells were illuminated with UV light, an external mercury lamp source (U-HGLGPS; Olympus Corporation, Tokyo, Japan) was incorporated to the microscope IX-73. In this case, the illumination of the cell was not from the top, but from the bottom, where a beam from the light source was filtered by a UV 365/10 nm bandpass filter (TECHSPEC®HC365; Edmund Optics Ltd., York, UK), then reflected by a beam splitter (Semrock HC 593; IDEX Health & Science LLC, Rochester, NY, USA) towards the sample and finally focused on the cell by a 20x objective. An illustration of this illumination setup[9] is shown in Fig. 3.7. As the UV light does not reach the sensor of the camera, background illumination was provided from the top by the halogen lamp of the microscope. The background illumination was filtered using a red-light bandpass filter (671/10 nm), provided that it does not induce light-switchable flagellar adhesion of the cell. A 665/65 nm bandpass filter (BP ET665/65; Chroma Technology Corporation, Bellows Falls, VT, USA) was placed between the beamsplitter and the camera to filter any parasite light that could distort the final image. A list of the filters used in force-distance experiments and in other experiments of this thesis is provided in the Appendix A.1.

With respect to the intensities used, all experiments performed with the

[9]This setup was developed by Dr. Kristian Hantke and Dr. Antoine Girot at the Max Planck Institute for Dynamics and Self-Organization, Göttingen, Germany.

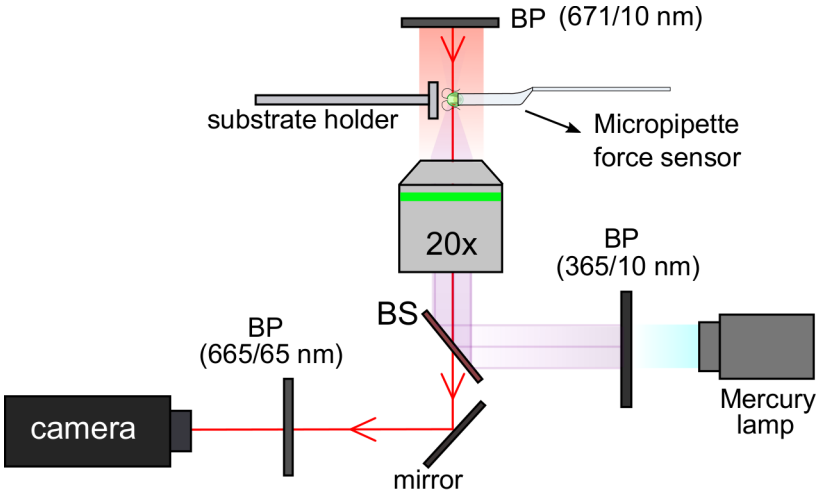


**Figure 3.7:** Experimental setup for force measurements under UV illumination. The light coming from a mercury lamp passes through a 365/10 nm bandpass (BP) filter that is transparent to UV light. A beamsplitter (BS), opaque to UV light, redirects the beam towards the sample. A 20x objective focuses the UV-beam on the *C. reinhardtii* cell being held by a micropipette force sensor. Background illumination to image the experiment was provided by a red-light BP filter transparent to 671/10 nm. The red light beam passes the BS and is reflected to the camera by a mirror. A BP filter was used to prevent parasite light from reaching the camera.

*C. reinhardtii* strain SAG11-32b were performed with a standard illumination of $1 \cdot 10^{19}$ photons$\cdot$ $\mathrm{m}^{-2} \cdot \mathrm{s}^{-1}$. The strain SAG 73.72 required an illumination of $3 \cdot 10^{19}$ photons$\cdot\mathrm{m}^{-2} \cdot \mathrm{s}^{-1}$ to trigger light-switchable adhesion.

### Data acquisition

In the following paragraphs, I describe the procedure to acquire the data for force-distance experiments. I followed the established protocol developed by Dr. Kreis, which is detailed in his doctoral thesis [278]. The extraction of the force-distance curves from the raw deflection data was done by the autocorrelation analysis described previously in Sec. 3.2.2.

Each individual force-distance cycle consists of a substrate-cell approach, a contact time during which the cell's flagella were in contact with the substrate, and the retraction of the substrate from the cell, see Fig. 3.8. The coordinate system was chosen such that a zero distance corresponds to the contact position of the substrate and the cell body. The adhesion force of the cell can be calculated, either from the raw deflection-time data or from the force-distance curve. The definition of the adhesion force is the maximal force measured during the detachment process of the cell, which corresponds to the minimal force in the retraction cycle of the force-distance curve, see Fig. 3.8b. A complete force spectroscopy experiment consisted of a set of 5 individual force-distance cycles that were consecutively performed using the exact same *C. reinhardtii* cell.

The following points summarize the standard parameters used in every MFS experiment. Any deviation from this protocol will be explicitly mentioned in the description of the experiment itself.

- Optical images of the force-distance curves were recorded at 10 fps using an objective with 20x magnification.
- The substrate was moved, using high-precision linear motors, at a constant speed of 1 µm/s during both the approach and retraction regimes. The limits of the substrate motion were such that the cantilever is deflected 10 µm during the push phase, and, upon retraction, it is positioned at 30 µm from the contact position.
- Between the push and retraction phases, the substrate remained stationary for approximately 10 seconds (defined as the *dwell time*). This guarantees that the total cell-substrate contact time (i.e. push, dwelling and retraction) was of approximately 30 seconds before the cell detached from the substrate.
- The time between two contact periods of consecutive force-distance cycles was about 50 to 60 seconds, which is long enough so that the flagella restored a regular beating after the detachment from the solid substrate.
- Unless stated otherwise, the cells were illuminated with an irradiance of $1 \cdot 10^{19}$ photons$\cdot$m$^{-2} \cdot$ s$^{-1}$. Before the start of the measurements, the cells were illuminated for 5 minutes at the working wavelength. A list of the filters used can be found in the Appendix Section A.1.

### 3.2.5 Statistical analysis of force-distance data

Once the experimental data of adhesion forces was collected, I proceeded to extract information from it using diverse statistical tools. For the analysis of the data, I used the built-in statistical tools and fitting functions of MATLAB. In the following, I briefly summarize the statistical methods that are relevant to this work. An in-depth overview of statistics can be found in introductory books on data analysis, for instance in the book[10] [280]. For an applied approach to the statistics in life sciences in general I recommend [281].

For the data points corresponding to single-cell force measurements at a particular wavelength, the mean adhesion extracted from all the force-distance cycles is presented with errorbars representing the standard deviation of the data. In the present case, the standard deviation is given in round parentheses after the average value. For instance, an adhesion force of 1.53(4) nN means that the mean adhesion

[10]Chapter 3 of this book contains the basic statistical tools to be applied using MATLAB.

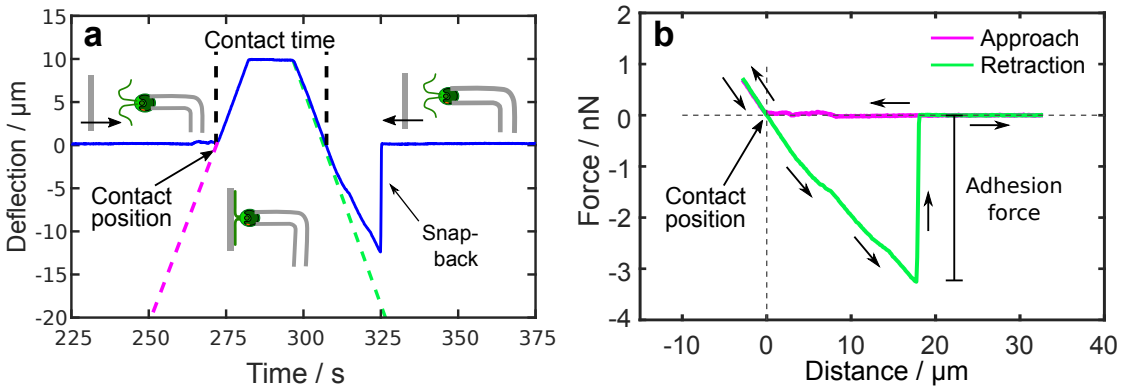


**Figure 3.8:** (a) The different stages of MFS measurements. The pink and green dashed lines represent the approach and the retraction of the substrate, respectively. Initially, the substrate is approached towards the cell. Then the substrate comes into contact with the cell and enters the repulsive force regime, where the cantilever is pushed up to a given distance (in this example, 10 µm). The initial encounter between the substrate and the cell sets the contact position. After the push regime, the cantilever is in stationary contact with the cell before the start of the retraction. Upon retraction, the contact between the cell and the substrate extends below the contact position if the cell is attached by its flagella to the substrate. In that case, the cantilever is deflected until its restoring force overcomes the flagellar adhesion and the cantilever snaps back to its resting zero-deflection position. (b) Force-distance curve extracted from the deflection measurement. The flagellar adhesion force is defined as the maximum deflection of the cantilever before it snaps back to its equilibrium position.

force is 1.53 nN with a standard deviation of 0.04 nN, whereas 1.83(12) nN refers to a mean adhesion of 1.83 nN with a standard deviation of 0.12 nN. The plus-or-minus nomenclature, namely 1.83±0.12 is not presented as it implies a symmetric distribution that has not been seen for flagellar adhesion forces of *C. reinhardtii* [40].

Confidence intervals are set to 95% of confidence level. The box bracket nomenclature is sometimes used to indicate half of the width of the confidence interval. For example, a value $\alpha = 0.45[3]$ indicates a fit that yields a value of $\alpha = 0.45$ with 95% confidence interval ranging from 0.42 to 0.48.

### Visualization of datasets

The statistical analysis for MFS experiments can be represented in three ways: visualization of the forces by means of a histogram, box-plots, and the empirical cumulative distribution function (ECDF) of the sample. In the following, I describe the pros and cons of each representation.

### Histograms

The histograms provide intuitive insights into the statistical distribution of the data points, where several features, such as the skewness of the data or even multi-modal features, can be easily recognized, see Fig. 3.9a. Nevertheless, a reliable representa-

tion requires a relatively large amount of data points (ideally more than 100 individual data points), so that the bin width of the histogram is chosen small enough to give the distribution a continuous appearance. Furthermore, it is not so easy to retrieve important statistical parameters from a histogram, such as the spread, the mean, or the median of the distribution. For this reason, other representations of the data are needed.

Box plots are useful to visualize samples containing a relatively limited amount of data points. The usefulness of boxplots comes from the fact that they show certain statistical features of the data set without addressing to a specific distribution, see Fig. 3.9b. The upper and lower boundaries of the box indicate the 25th and the 75th percentile[11], respectively. The horizontal line within the box corresponds to the *median* of all observations, which indicates that 50% of the data set is above or below this value. The difference between the upper and lower quartiles is the interquartile range (IQR) and is a measure of the spread of the data. The vertical lines projected beyond the lower and upper quartile are called *whiskers* and they extend up to 1.5 times the value of the IQR. All the observations that appear beyond the limits of the whiskers are considered to represent *outliers*. Conclusively, a boxplot is a simple, yet quite intuitive way to represent the data set, which can give a good characterization of its distribution.

The final representation to be discussed is the empirical cumulative distribution function (ECDF) of the data set, see Fig. 3.9c. This is the discrete version of a cumulative distribution function. The idea behind the ECDF is that, given any value $x_0$ of the data set, the ECDF gives the fraction of the points in the data that are smaller than $x_0$. This helps to visualize any of the intervals shown in the discussion of boxplots, such as the median, the upper and lower quartiles, or interval that contains a given fraction of the data set. To assess statistical differences between the distribution of two data sets, one can compare their ECDFs using a statistical significance test described below.

### Logarithimic-Normal Distribution

The logarithmic-normal distribution, commonly known as log-normal distribution, is a distribution in which the logarithm of a random variable is normally distributed. The probability density function of the log-normal distribution is:

$$f(x) = \frac{1}{\beta x\sqrt{2\pi}} \exp\left(-\frac{\left(\ln(x) - \alpha\right)^2}{2\beta^2}\right) \tag{3.2}$$

Here, the statistical properties of the data set can be obtained as follows.

[11] The 25th percentile (also known as *lower quartile*) is the median of the lower half of the data set. The 75th percentile (also known as *upper quartile*) is the median of the upper half of the data set.

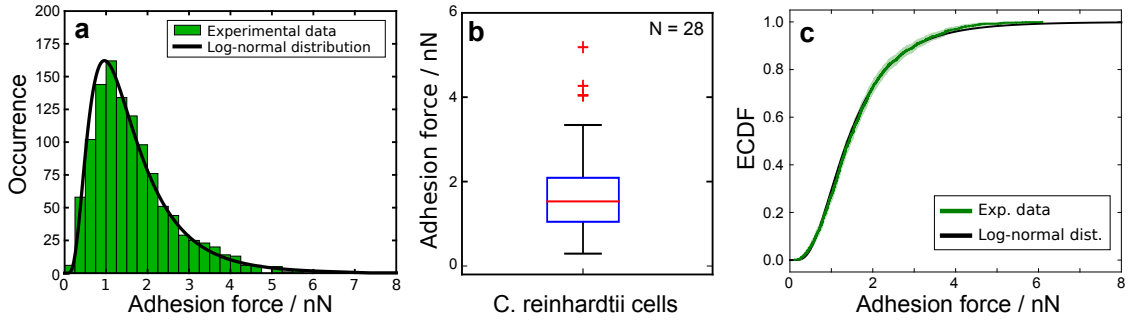


**Figure 3.9:** Three ways to visualize the statistical distribution of a data set. Flagellar adhesion forces are known to be log-normally distributed [39, 40]. (a) Histogram representing the statistical distribution of adhesion forces of *C. reinhardtii* cells under white light. The sample consists of 114 cells or *biological replicates* [278], each of which contributes 10 individual force measurements or *technical replicates*. (b) Box plot showing the adhesion forces measured for 28 different *C. reinhardtii* cells. Five measurements were done for each cell. (c) Empirical cumulative distribution function (ECDF) of the data set shown in (a).

The value $\exp(\alpha)$ gives the median; the mean of the distribution is obtained as $\exp(\alpha + \beta^2/2)$; and the standard deviation of the data set is $\exp(\alpha + \beta^2/2) \cdot \sqrt{\exp(\beta^2) - 1}$. The log-normal distribution has a distinctive right skewness given by $(\exp(\beta^2/2) + 2) \cdot \sqrt{\exp(\beta^2) - 1}$. The log-normal distribution often represents biological phenomena, as the outcomes exhibited in such systems have positive values. In particular, the adhesion force to a substrate, for instance, can be characterized as a log-normal distribution, see Fig. 3.9a.

### Statistical Significance Testing: The Kolmogorov-Smirnoff test

In order to evaluate statistical differences between two data sets, a statistical significance test is performed. The test evaluates the so-called *null hypothesis* $H_0$, in which a specific relation between the data sets is assumed to be truth. As the data sets usually are collected from different experimental conditions, the significant test is a way to assess whether changes in such conditions significantly influence the results obtained. Below, I describe the protocol for statistical significance testing that I applied to compare the distribution of flagellar adhesion forces obtained from micropipette force measurements. The protocol stems from the doctoral thesis of Dr. Christian T. Kreis [278].

A significance test gives a quantitative measure for the certainty of the null hypothesis, which can be rejected at a specific significance level. The significance level in force-distance measurements is 5% [278], which means that the probability of rejecting the null hypothesis is 5% (this is known as *type I error*). If the significance test fails to reject the null hypothesis this does not mean that the null hypothesis is true. Nevertheless, the failure to reject the null hypothesis is a strong indication that $H_0$ resembles the actual relation between two data sets.

A way to test the null hypothesis is by using a Kolmogorov-Smirnoff (KS) test, which assesses the null hypothesis that two distributions of data (for instance, adhesion forces obtained with the exact same cell under different light conditions) were drawn from the same underlying distribution:

$$H_0 : \ F_1 = F_2 \tag{3.3}$$

where $F_1$ and $F_2$ are the ECDFs of each data set. A rejection of the null hypothesis means that the two sets come from different distributions. In other words, the adhesion forces under two different light conditions are different, with 95% of certainty at a significance level of 5%. In contrast, if the test fails to reject the null hypothesis, it can be assumed, with high confidence, that there is a non-significant difference between the adhesion forces under the two light conditions.

To test the null hypothesis, the KS significant test quantifies the difference between the ECDFs of the two samples. Mathematically:

$$T_{KS} = \sup_x \left| F_1(x) - F_2(x) \right| \tag{3.4}$$

If the sizes of the first and second samples are $n$ and $m$, respectively, the null hypothesis that the distributions are equal is rejected if:

$$T_{KS} > c(\alpha) \sqrt{\frac{n+m}{n \cdot m}} \tag{3.5}$$

where $c(\alpha = 0.05) = 1.36$ and $c(\alpha = 0.01) = 1.63$ are fixed to account for a significance level of 5% and 1%, respectively. The KS-test statistic is then the maximal absolute difference (residuals) of the two empirical distribution functions. In MATLAB a two-sample KS-test can be performed using the function *kstest2()*.

A one-sided KS-test is used to evaluate whether the ECDF $F_1$ is significantly larger or smaller than the ECDF $F_2$. In other words, the null hypothesis is now $H_0 : \ F_1 > F_2$ and the KS-test is:

$$T_{KS} = \max_x \left( F_1(x) - F_2(x) \right) \tag{3.6}$$

or, for the alternative hypothesis $H_0 : \ F_1 < F_2$:

$$T_{KS} = \max_x \left( F_2(x) - F_1(x) \right) \tag{3.7}$$

The alternative hypothesis is accepted at a given significance level in case that Eq. (3.5) is true, where $c'(\alpha = 0.05) = 1.22$ and $c'(\alpha = 0.01) = 1.36$ correspond to a significance level of 5% and 1%, respectively. Note that the smaller ECDF belongs to the data set with the larger values and vice versa.

## 3.3 Adsorption experiments

Besides the quantitative characterization of adhesion forces of *C. reinhardtii* strains, I also performed adsorption experiments aiming at studying the light-induced surface colonization of *Chlamydomonas* cells to a glass substrate. In this type of experiment, a small volume of a *C. reinhardtii* cell suspension was injected into a cylindrical chamber, which has a height of around 300 µm and a diameter of 4 mm. The chamber was enclosed in between two microscope glass slides. Then, the cells in the suspension are illuminated with blue light (the filters used are mentioned in Section 3.3.2), which induces the transition of the cells from the planktonic state to the surface-associated state onto the microscope slides enclosing the PDMS chamber. Subsequently, red light is applied so that the cells detach from the glass surface and return to the planktonic state. The idea behind these experiments was to establish a reliable protocol that could quantify the kinetics of adsorption during the first stage of microalgal biofilm formation and assess the influence of phototaxis on the kinetics of adsorption. Below, I describe the different steps that were followed to perform adsorption experiments.

### 3.3.1 Fabrication of liquid chambers

The first step before the preparation of the adsorption experiments is the production of cylindrical chambers. The chambers are made of polydimethylsiloxane (PDMS; Sylgard™184, Dow Corning, Michigan, USA), which is a polymer commonly used to manufacture microfluidic devices [282]. I thoroughly mixed the PDMS base polymer with a curing agent in a 10:1 weight, as recommended by the manufacturer. This was intended to generate flexible PDMS chambers that could be easily manipulated. After mixing the PDMS base with the curing agent, a lot of bubbles were formed within the mixture. The bubbles were removed by placing the mixture inside a dessicator and applying vaccuum for up to one hour.

After all the bubbles were removed from the mixture of PDMS base and curing agent, I proceeded to fabricate PDMS slabs of thickness of around 300 µm. To impose the desired height, I used stacks made out of of two glass coverslips (24×24 mm). Each coverslip has a height of around 150 µm. Hence, each stack has a height of about 30 µm. Two of these stacks were fixed with adhesive tape on a plastic Petri dish and positioned at a distance of around 5 cm apart. Subsequently, a small volume of 0.4 mL of PDMS mixture was placed in between both stacks using a syringe, and then the volume was spread out by putting a rectangular polystyrene microscope slide (76×25 mm) on top of it. The extremes of the slide were touching the coverslips and confined the volume of PDMS to form a slab with an approximate height of 300 µm. Then, the slab was put inside a closed oven at 75°C for 2-3 hours to speed up the cross-linking reaction between the PDMS base and the curing agent.

After cross-linking was completed in the oven, a solid and flexible PDMS slab was obtained and served to generate several circular chambers with outer diameter of 7 mm and a central hole with an inner diameter of 4 mm. The circular cuts were made using Harris Uni-core punchers.

### 3.3.2 Cell counting

Axenic cultures of vegetative *C. reinhardtii* cells were cultivated as described in Sec. 3.1. The cells were harvested on the third day after cultivation, approximately one hour after starting the day phase.

In order to work with a controlled density of the suspension during the experiment, the determination of the number of cells per unit volume needed to be determined. For this, I first centrifuge 50 mL of cell culture at 100 $g$ for ten minutes using a lab centrifuge (5804R; Eppendorf, Hamburg, Germany). The cells were accumulated at the bottom of the centrifuge tube and I removed the excess of liquid culture medium. Then, I resuspended the cells by adding 2 mL of fresh TAP medium and obtained a very dense suspension, which needed to be diluted later on. As the shear forces inside the liquid culture can deflagellate the cells during centrifugation, I placed the resuspended cells in the incubator for two hours. This guarantees that the cells had completely regrown their flagella, which typically should take between 45-60 minutes [45].

After the resting time in the incubator, I determined the number of cells in a given volume of the dense suspension. As the starting cultures were usually quite dense, I diluted 50 µL of the suspension in 450 µL of TAP medium and I fixed the cells using 2 µL of formaldehyde. Subsequently, I counted the number of cells in a given volume using a counting chamber (Neubauer Improved; Laboroptik Ltd., Lancing, UK) which allowed me to determine the concentration of the dense suspension. Subsequently, I readjusted the concentration of the dense suspension by adding TAP medium so that a final concentration of $5 \cdot 10^6$ cells/mL was obtained.

### 3.3.3 Assembly of the liquid chamber

Once the cell concentration in the suspension was controlled, I started to assemble the experimental liquid chamber. All the components of this chamber, namely the glass slides and the PDMS circular chamber were carefully cleaned with HPLC-grade ethanol (LiChrosol®; Merck KGaA, Darmstadt, Germany) and dried using a stream of ultra-pure nitrogen. A circular PDMS ring was settled on a glass slide and a droplet of around 80 µL of the cell suspension was placed inside the circular compartment, which was then closed by another glass slide on top of it, as shown in Fig. 3.10a. Finally, the liquid chamber was mounted onto the stage of an inverted optical microscope.

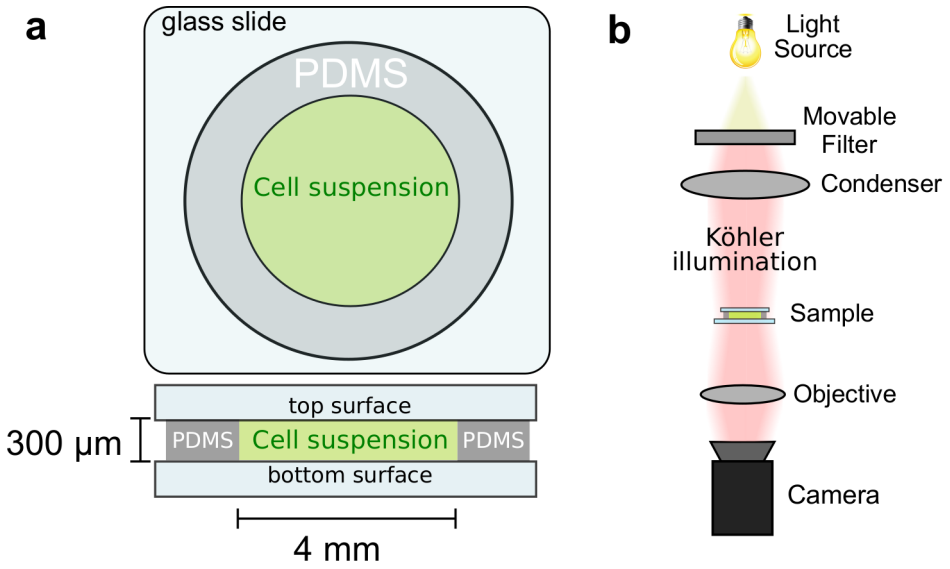


**Figure 3.10:** (a) (Top) Top-view sketch of the circular chamber used for adsorption experiments. The chamber is made out of polydimethylsiloxane (PDMS) and has an inner diameter of 4 mm and outer diameter of 7 mm. The height of the chamber is 300 µm. (Bottom) Side view of the same PDMS chamber, which is enclosed by two glass slides. The top and bottom surfaces of the chambers confine the cell suspension. (b) Experimental setup used for adsorption experiments. The light beam was collimated by the condenser and Köhler illumination was set up for homogeneous illumination of the entire chamber.

### 3.3.4 Experimental setup and light conditions

Inverted optical microscopes (IX-83; Olympus Corporation, Tokyo, Japan) were used to perform adsorption experiments, see Fig. 3.10b. The same greyscale camera (Grashopper GS3-U3-41C6M-C; FLIR Integrated Imaging Solutions Inc., Richmond, BC, Canada) as the one used for MFS experiments was used for adsorption experiments. The microscopes were equipped with either a built-in LED light source or a halogen lamp. Both light sources generated a light beam of 25 mm in diameter, which is sufficiently large to illuminate the entire PDMS compartment. For the purpose of providing a homogeneous light intensity through the sample, I set up Köhler illumination on the chamber and subsequently exposed the cells in the suspension to red light (664/11 nm) with an intensity of $1 \cdot 10^{19}$ photons$\cdot$m$^{-2} \cdot$ s$^{-1}$ for 5-10 minutes. This guarantees that the cells that were adsorbed to the glass surfaces, before mounting the chamber on the microscope, transit to the planktonic state. After this, the cells in the suspension were in the planktonic state and I proceeded to start the adsorption experiments.

### 3.3.5 Data acquisition

After red-light incubation, I started to record optical images at 3 fps using a 20x objective with 1.6x extra magnification, thus, yielding a 32x magnification in total. All the optical micrographs were recorded focusing on either the top or the bottom

surface of the PDMS compartment, as these are the boundaries in which the adsorption and the desorption of the cells are observed. Except for ΔChR1,2, I recorded micrographs focusing on the bottom surface of the experimental chamber for all the rest of the strains studied.

After starting recording images, I switched the illumination conditions by selecting another wavelength with a different filter. Most of the adsorption experiments were recorded under two light conditions. Unless otherwise stated, these light conditions are:

- **blue illumination**: LED light source or halogen lamp, using a bandpass interference filter 476/11 nm. An intensity of $1 \cdot 10^{19}$ photons$\cdot$m$^{-2} \cdot$ s$^{-1}$ is used for SAG11-32b, and $3 \cdot 10^{19}$ photons$\cdot$m$^{-2} \cdot$ s$^{-1}$ for SAG 73.72.

- **red illumination**: LED light source or halogen lamp, using a bandpass interference filter 664/11 nm or 671/10 nm. Intensity of $1 \cdot 10^{19}$ photons$\cdot$m$^{-2} \cdot$ s$^{-1}$ for SAG11-32b and $3 \cdot 10^{19}$ photons$\cdot$m$^{-2} \cdot$ s$^{-1}$ for SAG 73.72. Under these light conditions, cells adsorbed to the glass slides detach and swim to the bulk of the chamber.

I recorded around 1000 frames under blue light, which is equivalent to approximately 330 s of light exposure. This time was enough to see the adsorption process of *C. reinhardtii* cells to the glass surface of the PDMS chamber until a constant surface density was established (i.e. no more cells were seen to adhere to the glass surface). Afterwards I switched back to red light, during which the cells were recorded for another 330 s. This time frame was enough to see the desorption of almost all the cells that were attached to the surface under blue light.

After completing the recording in blue- and red-light conditions, I kept the cells in red light, and after 5-10 minutes of red-light incubation, I started another cycle of measurements. For a complete adsorption experiment, I recorded between 5 to 7 adsorption/desorption cycles. Given that these are experiments performed on the population level, I required a minimum of 4-5 independent experiments, for each strain studied, to yield statistically robust data.

Different intensities and wavelengths were also used in the present work, for instance, in experiments studying the dependence of the adsorption kinetics on the light intensity, or the action spectrum of adsorption (i.e. its dependence on the wavelength) of *C. reinhardtii* cells. A table with the bandpass filters used in adsorption experiments is provided in the Supplementary Information Section. Nevertheless, regardless of the light conditions stated above as an example, the protocol for taking adsorption/desorption measurements remained the same.

**Early-morning adsorption experiments**

As mentioned in Section 2.4.2, pCRY has been found to be light-degraded at the beginning of the cells' day phase [228, 229]. To test this, I performed adsorption experiments using both WT and ΔpCRY *C. reinhardtii* cells before the start of subjective day[12]. I call such type of adsorption experiments: *early-morning experiments*.

For the preparation of the early-morning experiments, I took an experimental liquid culture containing vegetative WT or ΔpCRY cells out of the incubator, around 40 minutes before the start of subjective day. I wrapped the flasks with aluminum foil and kept the lights of the laboratory off in order to avoid exposure of the cells to visible light. Due to time and illumination constraints, I did not do cell counting for early-morning experiments. Therefore, I maximized the chances of having a high amount of cells in the suspension by preparing cultures that were more concentrated than the ones used for regular adsorption experiments[13].

For the assembly of the chamber, I followed the same procedure described for the regular adsorption experiments, although, this time, I only used a small flashlight to orient myself during the chamber assembly. I placed the flashlight at around 2 m of distance from the working bench, pointing away from the cell chamber. Since at the end of subjective night there are several cells in the final stage of the mitotic division, see Fig. 2.4, I only worked with volumes from the upper part of the cell suspension. In that way I aimed to maximize the number of swimming cells in the chamber and minimized groups of non-motile cells that were still dividing.

After assembling the chamber, I mounted it on the microscope stage and used red light in low light conditions (i.e., intensity less than $1 \cdot 10^{16}$ photons$\cdot$m$^{-2} \cdot$s$^{-1}$) for a few seconds to center the chamber in the path of the light beam. Subsequently, I started recording adsorption runs at 3 fps and 32x magnification. For this, I exposed the cells to blue light at an intensity of $1 \cdot 10^{19}$ photons$\cdot$m$^{-2} \cdot$s$^{-1}$ and recorded 900 micrographs. At the end of the adsorption run, I turned off the light and left the cells in darkness for 15 minutes after the start of the following adsorption run. Before each run of adsorption, I used low-intensity red light for a few seconds to assess whether the cells had left the surface during the dark phase of the experiment.

### 3.3.6 Cell detection in optical images

After finishing the adsorption experiments, I used a particle-detection algorithm, written in MATLAB, to count the number of cells that were adsorbed during the

[12]The use of the terminology *subjective day / night* refers to the moment in the circadian cycle in which the microalgae are found.

[13]For early-morning experiments, experimental cultures were prepared 3 days before the experiments, using a one-week-old, synchronized mother culture. The experimental culture consisted of 100 µL of mother culture in 50 mL of fresh TAP medium.

adsorption/desorption cycles. The detection algorithm consisted of two parts: cell detection and cell tracking.

Since the cell bodies of *C. reinhardtii* appear circular in the micrographs when they are in the gliding configuration on the surface of the compartment, I used the built-in MATLAB function called *imfindcircles* for detecting circular objects, i.e., the adsorbed cells during the experiments. This function also provided information on the cell radii, from which I obtained the size distribution of the studied cell population, see Sec. 4.1.

When the cells are adsorbed on the surface, during blue light illumination, most of them stay in the gliding configuration, in which they move on the surface along the flagella direction, see Fig. 2.6. However, some cells remain only loosely attached and may transit back to the planktonic state in the suspension. Cells that are not completely attached to the surface might still be detected as adsorbed cells by the algorithm, which would yield a miscounting of the adsorbed cells and noisy data. In order to avoid this, I used a tracking algorithm [283], which links the positions of all the cells between consecutive frames. In other words, the tracking algorithm established a trajectory for each detected cell in the adsorption experiment. To identify only the cells that were in the gliding configuration, I constrained the program according to the distance a gliding cell can move between consecutive frames. Since the gliding speed of cells is approximately 1-2 $\mu m \cdot s^{-1}$ [45], the displacement between frames taken at 3 fps is of around 0.7 µm, which is less than the average cell radius of *Chlamydomonas*. Therefore, I only allowed the tracking algorithm to consider displacements up to one average cell radius between consecutive frames. Cells, whose trajectory spans less than 2 s are consequently removed from the dataset. Identifying the correct number of adhered cells allows then to monitor the time-dependent surface cell density throughout each adsorption/desorption cycle. From this collected data, I generated adsorption and desorption curves that I present in the following chapter.

# Chapter 4

# Kinetics of light-regulated adsorption and desorption of *C. reinhardtii*

Microbial colonization of surfaces represents the first step towards biofilm formation. While most of the research has been oriented to understand bacterial surface colonization, the underlying phenomena associated to the adhesion of photosynthetic microbes remain largely unexplored so far. In this chapter, I present the results on the adsorption experiments using vegetative cells of the photoactive microalga *C. reinhardtii*. The main objective was to establish a protocol to quantify the kinetics of adsorption and desorption of the cells, aiming at establishing adsorption experiments as an assay for characterizing the dynamics of the surface colonization of photoactive microbes under precisely-controlled light conditions. This approach will be then used in subsequent chapters as a complementary way to determine the photoreceptor mediating light-switchable adhesion of *Chlamydomonas*. Most of the results presented in this chapter have been published in a peer-reviewed article [284].

## 4.1 Cell detection

As mentioned in Sec. 3.3, adsorption experiments were performed using *C. reinhardtii* cells of the WT strain SAG11-32b. The cells in the suspension, enclosed in the chamber shown in Fig. 3.10, were exposed to either blue light ($\lambda = 476$ nm) or red light ($\lambda = 664$ nm).

After the start of blue-light conditions, the cells in the suspension transition from the swimming state to the surface-associated state and exhibit several changes in their motility that are described below. First, I start with the process of adsorption at the single-cell level. The description of the adsorption on the population level is described in Sec. 4.2. When a *C. reinhardtii* cell in the suspension encounters

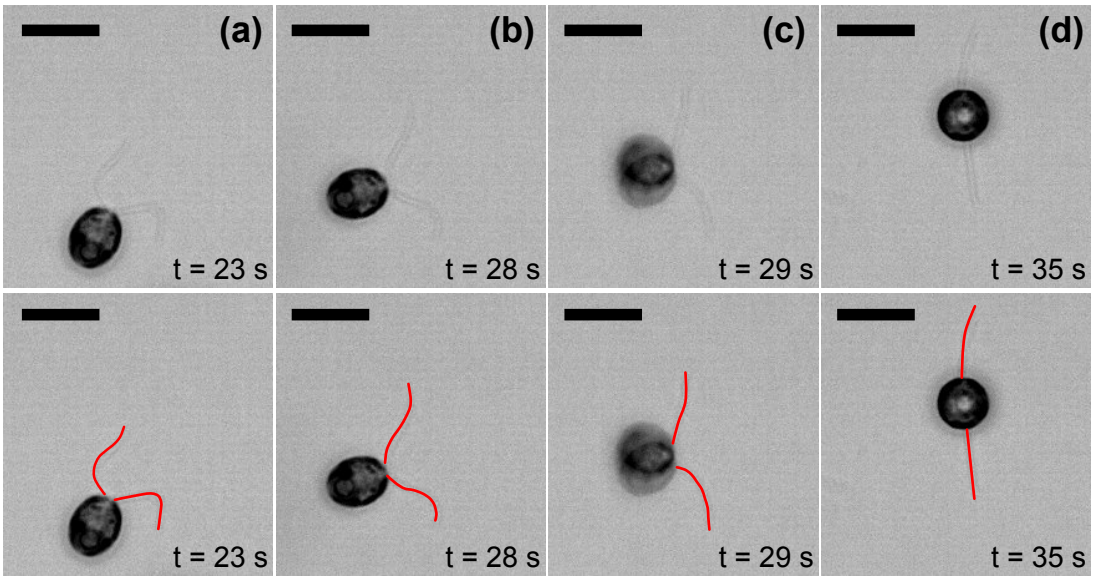


**Figure 4.1:** Sequence of optical micrographs showing the adsorption of a *C. reinhardtii* cell under blue light ($\lambda = 476$ nm). The scale bar represents of 10 µm. The time stamp shown in the micrographs corresponds to the time after exposing the cells to blue light. In the lower micrographs, the flagella have been highlighted in red for guidance. (a) When a swimming cell encounters the glass surface, usually the tips of each flagella adheres to the glass slide and anchors the cell to it. (b) The flagella establish further contact with the substrate and, in the process, they start to orient in opposite directions. (c) The portion of the flagella that is not adhered to the substrate can still beat, which makes the cell wiggle and appear blurry. This process continues until the gliding configuration is achieved, see Sec. 2.3.3. (d) In this configuration, the cell body appears circular in the micrograph and the cell can glide along the direction of either one of its flagella.

one of the glass surfaces of the liquid chamber, the cell is anchored to it by the tip of its flagella, see Fig. 4.1a. Subsequently, the flagella progressively orient in opposite directions and actively become more and more in contact with the slide, see Fig. 4.1b. At this stage, the flagella are partially in contact with the slide and the portion that is not adhered can still beat, which transiently changes the orientation of the cell body, see Fig. 4.1c. This phase continues until the flagella form an extended angle, which indicates that the cell has achieved the gliding configuration, as shown in Fig. 4.1d. In the gliding configuration, the cell body appears circular in the micrographs and the cell can glide along the direction of either flagella.

Under blue light, *C. reinhardtii* cells adsorb mostly to the bottom surface of the compartment, as shown in the micrographs of Fig. 4.2. Therefore, the micrographs to study the adsorption kinetics of WT *Chlamydomonas* cells were always recorded focusing at the bottom surface of the experimental chamber, unless otherwise stated. This guarantees a bigger sample of adsorbed cells, which yields a reliable statistical analysis of the experimental results. Conversely, when the adsorbed cells are then exposed to red light, their flagella start to become less and less in contact with the glass surface. During this phase, the flagella begin to resume their beating motion and, consequently, the cell body progressively exhibits more random reorientations.

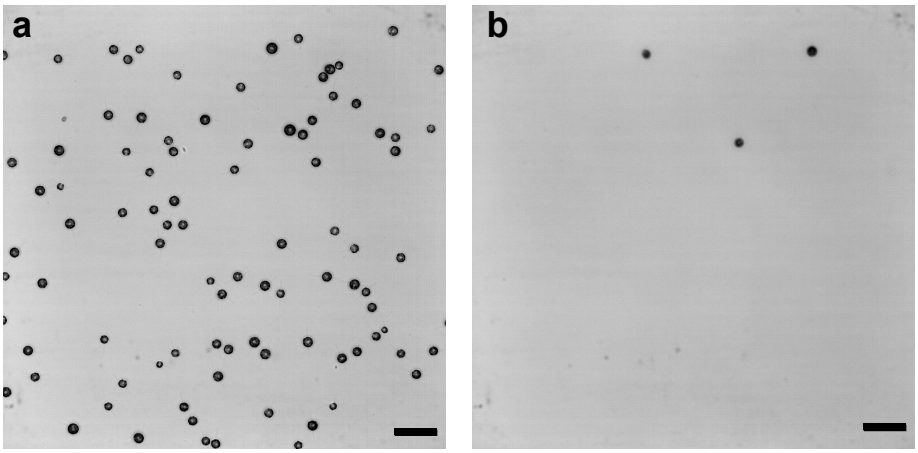


**Figure 4.2:** Micrographs showing WT *C. reinhardtii* cells adsorbed (a) at the bottom and (b) at top surface of the chamber. The micrograph at the bottom was taken 3 minutes after exposure to blue light, and the one at the top boundary was taken around 10 s later. It always occurred that there were many more cells adsorbed at the bottom boundary of the chamber rather than at the top of it, with the exception of strains that cannot perform phototaxis. This is further discussed in Sec. 4.5.

Finally, when the cells' flagella are able to completely detach from the substrate, the cells desorb and swim away to the bulk of the suspension.

To accurately track the timescales associated to the adsorption and desorption of the cells, I performed cell detection and tracking. To achieve this, I exploited the circular shape that the cells exhibit in the micrographs as they are in the gliding configuration, as explained in Sec. 3.3.6. The particle detection algorithm identifies the circular objects that are darker than their background, and whose radii are within a interval. For all the experiments using *C. reinhardtii* strains, I used an interval of cell radii between 2.2-6.5 µm, which is compatible with the size of *C. reinhardtii* cells [45]. The algorithm can successfully detect the cells adsorbed, as shown in Fig. 4.3.

For every circular object detected in each micrograph, the position of its center and also its radius were obtained. The micrograph that has the maximum amount of detected objects during the adsorption run is used to obtain the mean size of the cells. The values of the radii of the detected cells follow a log-normal distribution (see Sec. 3.2) with a mean of 3.61(0.06) µm, see Fig. 4.4. After every micrograph was analyzed with the particle detection algorithm, the trajectory of each detected cell was tracked and it was used to remove cells, whose displacement is more than 0.7 µm between consecutive frames, as mentioned in Sec. 3.3.6. In this way, only cells that are gliding on the glass surface are considered.

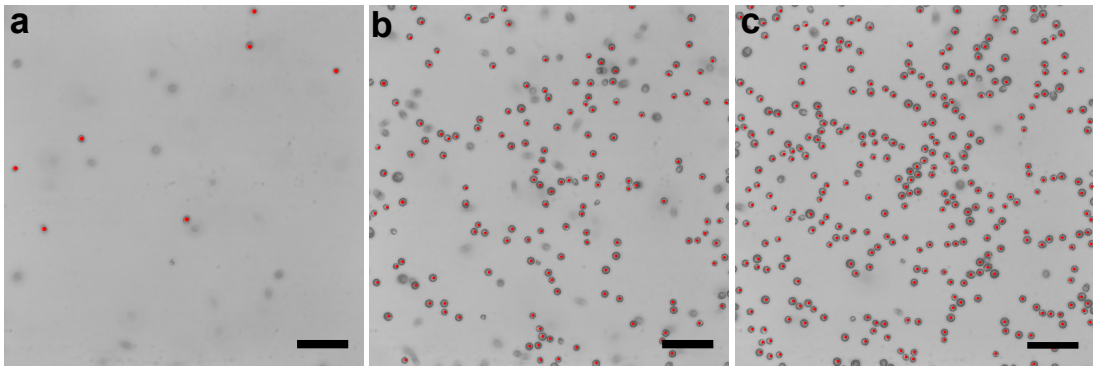


**Figure 4.3:** Micrographs showing adsorbed WT *C. reinhardtii* cells during a representative adsorption run (scale bar: 50 µm). Red dots highlight the cells that are successfully detected by the detection algorithm. (a) Micrograph taken 9 s after exposing the cells to blue light. The number of detected cells are 7. (b) Micrograph taken 54 s after switching to blue light. The number of detected cells are 144. (c). Micrograph taken 230 s after switching to blue light. The number of detected cells are 312.

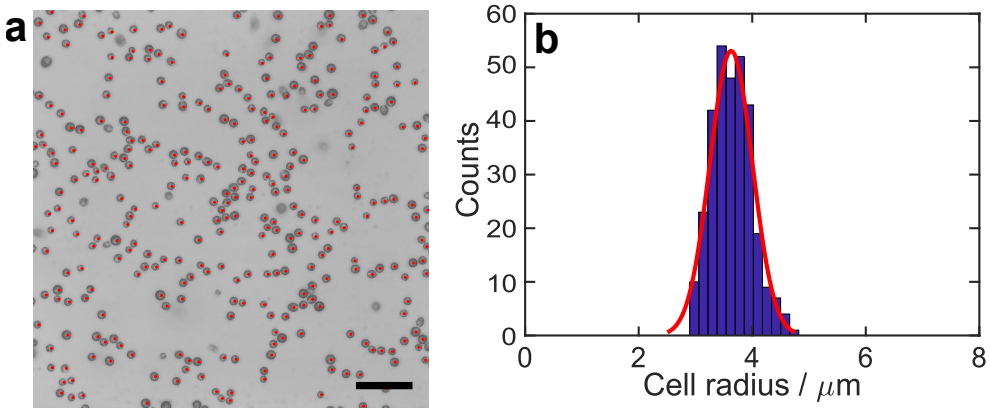


**Figure 4.4:** (a) Micrograph that shows a total of 312 detected circular objects, corresponding to *C. reinhardtii* cells adsorbed at the bottom surface of the compartment (scale bar: 50 µm). This micrograph contains the maximum amount of detected cells during an adsorption run and it is used to determine the average radius of the cells in the chamber. (b) Cell radius statistics (blue bars) detected in (a) matches a log-normal distribution with an average radius of 3.61(6) µm (red curve).

## 4.2 Adsorption curves

After the tracking algorithm generated a list of all the cells in the gliding configuration, I generated a plot showing the time dependence of the surface density of adsorbed cells for both adsorption and desorption. A typical result is shown in Fig. 4.5. The cell surface density at a given time is calculated considering the number of cells detected in a particular micrograph, divided by the physical area enclosed by the micrograph.

From the generated plot in Fig. 4.5, three main phases can be identified for an adsorption run. When the cells are just exposed to blue light, which occurs at $t = 0$ s, a delay interval is observed, where the surface density remains zero. This indicates that there are no cells adhering to the bottom surface immediately after exposure

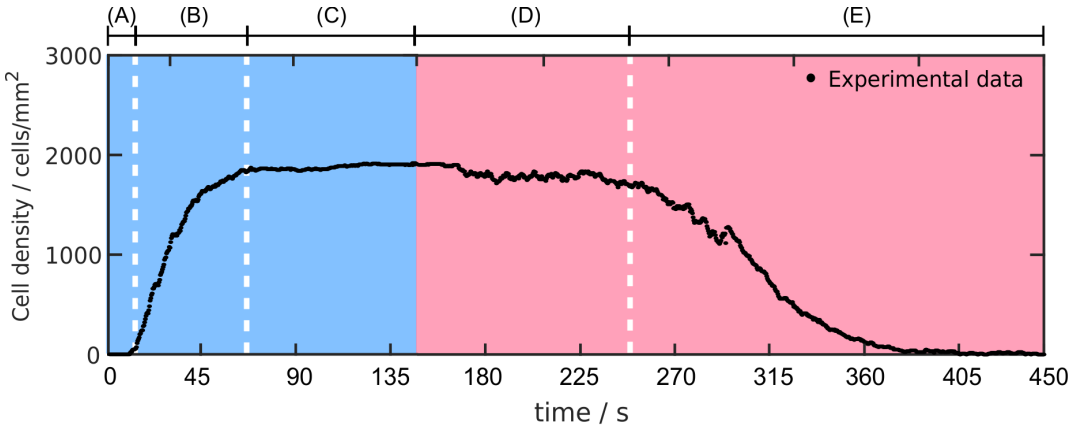


**Figure 4.5:** Representative time dependence of the surface density of adsorbed WT *C. reinhardtii* cells at the bottom boundary of the liquid chamber. The time $t = 0$ s corresponds to the time at which the light conditions were changed from red to blue. Later, at $t = 150$ s cells are again exposed to red light. Under blue light, there are three recognizable stages for an adsorption run: (A) a delay interval, in which the WT cells in the suspension exhibit positive phototaxis and swim towards the upper portion of the compartment, thus the cell surface density remains at zero. (B) Cells exhibit negative phototaxis and swim towards the bottom boundary, where they finally adsorb and the surface density increases. (C) A constant plateau density, in which most of the cells of the suspension are attached to the bottom boundary. This is a steady state where the surface density remains constant as long as the cells are exposed to blue light. If the cells are illuminated with red light, two steps can be identified: (D) A delay interval, where the cells' flagella progressively detach from the surface, but the cells still are attached to the surface. This maintains a constant value of the surface density. (E) The desorption interval, where the flagella are completely detached from the substrate and the cells return to the planktonic state.

to blue light. This transient delay interval only lasts around 10-15 s and is visually characterized by two events. First, just after the cells in the suspension are exposed to blue light, they swim towards the light source, away from the bottom of the chamber[1]. Subsequently, after around 3 s, the cells exhibit negative phototaxis and reverse their swimming direction and swim towards the bottom surface, which sets the end of the delay interval. The next stage starts as soon as the cells encounter the bottom surface and adsorb to it adopting the gliding configuration. This adsorption phase continues until all the cells in the suspension have transitioned to the gliding state.

The third stage corresponds then to a steady state that is characterized by having a constant number of adsorbed cells. In other words, a plateau density is achieved and it can be sustained as long as the cells are exposed to blue light. When the cells are subsequently exposed to red light, another delay interval is exhibited. In that stage, the surface density of adsorbed cells stays constant as the cell's flagella resume their beating and progressively detach from the substrate. Once the flagella are completely detached from the substrate, the last stage starts and it is characterized

[1]The experimental chamber is illuminated from the top, see Fig. 3.10b.

by the desorption of cells from the substrate. The desorption of cells progressively decreases the surface density until all the cells have completed the transition to the planktonic state. After obtaining the raw data that shows the time-dependence of the surface density of adsorbed cells under different light conditions, I developed a systematic approach to fit the raw data and quantify the timescales associated to the adsorption and desorption of *C. reinhardtii* cells. The fitting methodology is explained in the following section.

## 4.3 Time-delayed Langmuir model for cell adsorption

To quantitatively capture how fast the cells respond to the changes in the light conditions and the kinetics of their adsorption and desorption, I used a model that is inspired by the Langmuir model that describes the adsorption kinetics of molecules to surfaces[2] [285, 286]. Nevertheless, although the adsorption of cells to a surface is somewhat analog to the adsorption of molecules to the surface, the assumptions on which the Langmuir model is based need to be carefully readjusted in order to capture the dynamics of the adsorption experiments presented in this work. The classic Langmuir model reads:

$$\frac{d\sigma}{dt} = \frac{1}{\tau_{\mathrm{a}}} \left(\sigma_0 - \sigma\right) \tag{4.1}$$

where $\tau_{\mathrm{a}}$ is the characteristic time parameter that sets the rate of adsorption. The solution to the differential equation yields:

$$\sigma\left(t\right) = \sigma_0 \left(1 - e^{-\frac{t}{\tau_a}}\right) \tag{4.2}$$

Therefore, when the system is left to evolve from $t = 0$ s, the adsorbed particles approach a saturation density $\sigma_0$ by exponential decay with a characteristic time $\tau_{\mathrm{a}}$. An example adsorption curve of the classical Langmuir model is presented in Fig. 4.6, where it is evident that the model fails to capture the delay interval of the adsorption of *C. reinhardtii* to surfaces.

The Langmuir model assumes that the rate of adsorption of particles on a substrate decreases as the adsorption sites on the substrate become successively populated by immobile objects that form one single layer. This is fundamentally different from the adsorption experiments using *C. reinhardtii* cells, in which each cell can move in the surface-associated state by performing gliding motion. Especially at high

[2]The model and its implementation were carried out in collaboration with Dr. Alexandros A. Fragkopoulos.

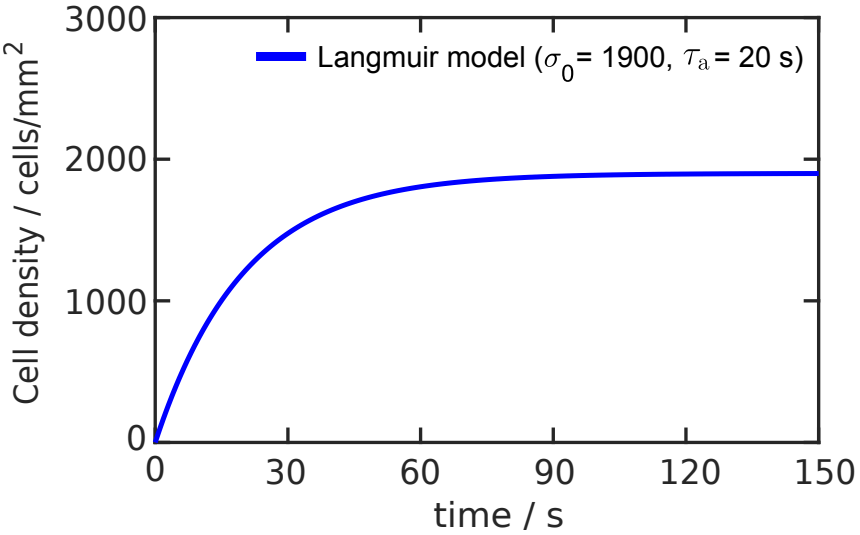


**Figure 4.6:** An example curve of the Langmuir model for saturation density $\sigma_0 = 1900$ cells/mm$^2$ and characteristic time $\tau_a = 20$ s. The instantaneous surface density increases immediately after $t = 0$ s, which fails to capture the initial dynamics of the adsorption of *C. reinhardtii* cells.

cell densities, gliding *C. reinhardtii* cells can develop clusters and interconnected cellular networks [287], which results in a higher packing efficiency that could certainly affect the available area for adsorption. Taking this into account, I excluded effects related to surface-bound cellular motility by performing adsorption experiments using suspensions with a low cell density, equivalent to a cell volume fraction of about 0.1%. In that case, the number of sites at which the cells can adsorb at any time is much larger than the number of cells in the suspension. As a consequence, the adsorption rate is limited by the number of available cells in the suspension rather than the number of available adsorption sites on the substrate.

Another aspect that needs to be taken into account is that the Langmuir model describes instantaneous adsorption or desorption of the particles when the system is left to evolve at $t = 0$ s. This results in a caveat of the Langmuir model to capture the initial delay interval that the cells exhibit when the illumination is changed, see Fig. 4.5. To account for this, I modified the Langmuir model introducing a time-dependent factor $s(t)$, so that the governing differential equation for the surface density of adsorbed *C. reinhardtii* cells is:

$$\frac{d\sigma}{dt} = \frac{1}{\tau_a} s(t) (\sigma_0 - \sigma(t)) \tag{4.3}$$

In this equation, $\sigma$ is the instantaneous cell density and $\sigma_0$ is the saturated surface density (or the plateau density). The parameter $\tau_a$ is a characteristic time that determines the rate of adsorption of the cells. Lastly, the time-dependent factor $s(t)$, which we coined the *stickiness function*, is mathematically defined as:

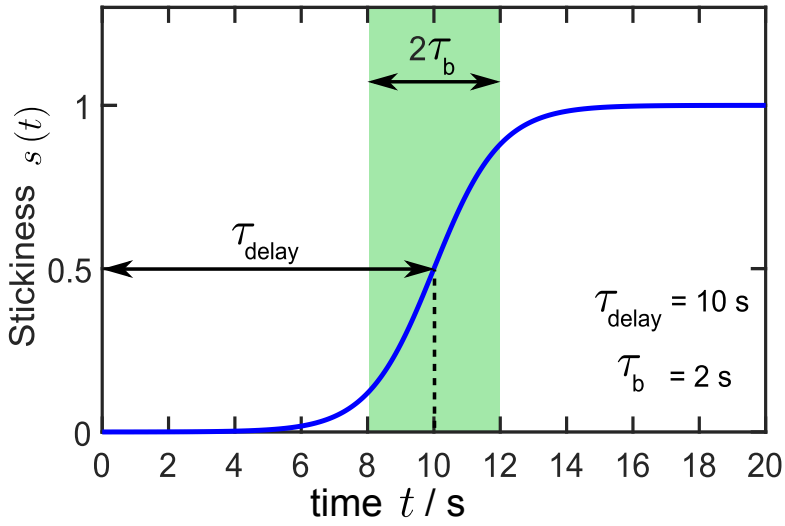


**Figure 4.7:** Stickiness function that is used to account for the delay interval of the adsorption and desorption kinetics of *C. reinhardtii* cells. Several time parameters are considered: the delay time $\tau_{\text{delay}}$, which is defined as the time in which 50% of the cells switch their flagellar adhesiveness to adsorb or desorb to the surfaces of the chamber; $\tau_{\text{b}}$, corresponds to the width of the step function and provides a measure of the cell-to-cell variability for the time that it takes the cells to switch their flagellar adhesive properties on or off. The values of the parameters chosen for this example are $\tau_{\text{delay}} = 10$ s and $\tau_{\text{b}} = 2$ s.

$$s\left(t\right) = \frac{1}{2} + \frac{1}{2}\tanh\left(\frac{t - \tau_{\text{delay}}}{\tau_{\text{b}}}\right) \tag{4.4}$$

This factor is assumed to be a smooth step-function that ranges from zero to one, as shown in Fig. 4.7, and it is introduced to account for the delay interval that precedes both adsorption and desorption. In addition to this, the stickiness functions takes into account the cell-to-cell variability of this delay, which is associated with the capacity that each cell has to switch on and off their flagellar adhesiveness. Note that the classical Langmuir model is recovered when $s\left(t\right) = 1$, see Eq. 4.3. From the definition of the stickiness function, several temporal parameters can be observed. First, the parameter $\tau_{\text{delay}}$ is the time at which 50% of the cell population in the suspension have switched on or off the adhesiveness of their flagella. The parameter $\tau_{\text{b}}$ corresponds to the width of the step, which provides a quantification of the cell-to-cell variability for the time that it takes for 50% of the cells to switch their flagellar adhesive properties, see Fig. 4.7. In other words, $\tau_{\text{b}}$ is the error related to the parameter $\tau_{\text{delay}}$. An analog fit curve for the desorption can be constructed by setting $\sigma_0$ to zero in Eq. (4.3) and $\sigma\left(t = 0\right) = \sigma_0$ as initial condition.

The analytical solutions for the change of the surface cell density during adsorption and desorption, expressed in Eq. (4.3), are:

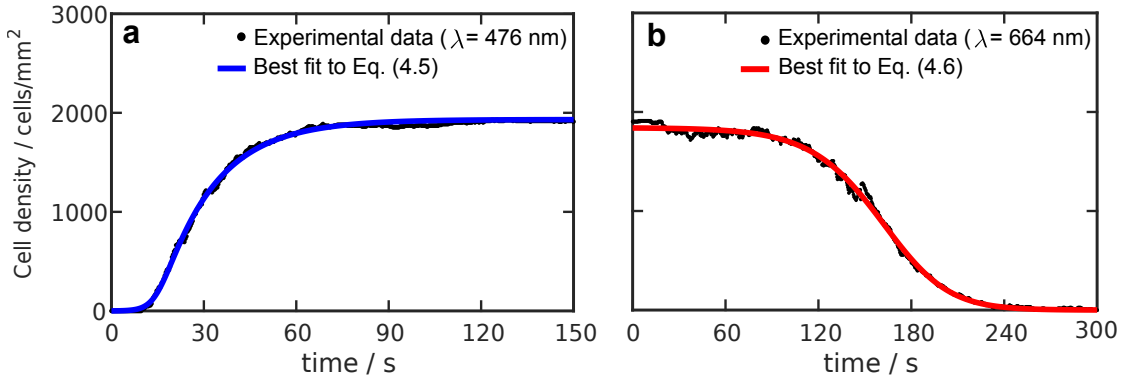


**Figure 4.8:** Best fits of the extended Langmuir model to the experimental data shown in Fig. 4.5. The fit functions for (a) the adsorption and (b) the desorption of *C. reinhardtii* cells were generated from an extended Langmuir model, which captures the delay intervals in both processes. Furthermore, the fit functions capture the entire dynamics of the adsorption and desorption runs, allowing for a more complete quantification of both processes.

$$\sigma_{\mathrm{ads}}(t) = \sigma_0 \left[ 1 - e^{-\frac{-t}{2\tau_{\mathrm{a}}}} \cdot \cosh^{\frac{\tau_{\mathrm{b}}}{2\tau_{\mathrm{a}}}} \left( \frac{\tau_{\mathrm{delay}}}{\tau_{\mathrm{b}}} \right) \cdot \cosh^{\frac{-\tau_{\mathrm{b}}}{2\tau_{\mathrm{a}}}} \left( \frac{\tau_{\mathrm{delay}} - t}{\tau_{\mathrm{b}}} \right) \right] \tag{4.5}$$

$$\sigma_{\mathrm{des}}(t) = \sigma_0 \cdot e^{-\frac{-t}{2\tau_{\mathrm{a}}}} \cdot \cosh^{\frac{\tau_{\mathrm{b}}}{2\tau_{\mathrm{a}}}} \left( \frac{\tau_{\mathrm{delay}}}{\tau_{\mathrm{b}}} \right) \cdot \cosh^{\frac{-\tau_{\mathrm{b}}}{2\tau_{\mathrm{a}}}} \left( \frac{\tau_{\mathrm{delay}} - t}{\tau_{\mathrm{b}}} \right) \tag{4.6}$$

where $\sigma_{\mathrm{ads}}$ and $\sigma_{\mathrm{des}}$ are the instantaneous surface densities during adsorption and desorption, respectively.

I fitted the analytical solutions to the experimental data presented in Fig. 4.5, which yields the fitting curves presented in Fig. 4.8. The analytical solutions were fitted to the experimental data in MATLAB considering a robust regression, which minimizes the sum of the square of the residuals to obtain *best-fit* adsorption and desorption plots. The curve fitting of the extended Langmuir model to the experimental data yielded values for the fit parameters with 95% confidence bounds.

From the presented plots, it is clear that the extended Langmuir model captures the delay interval observed in the experiments, which allows for a complete quantification of the dynamics of adsorption and desorption of *C. reinhardtii*. For each independent experiment, the mean values of the time parameters, obtained from a series of 5-6 adsorption/desorption cycles were calculated with their associated standard deviation. These results are presented in the next section, where the time parameters are compared to each other.

## 4.4 Adsorption and desorption timescales

From the plots presented in Fig. 4.8 it is readily seen that the kinetics of adsorption and desorption of *C. reinhardtii* cells are different. In fact, the delay interval of

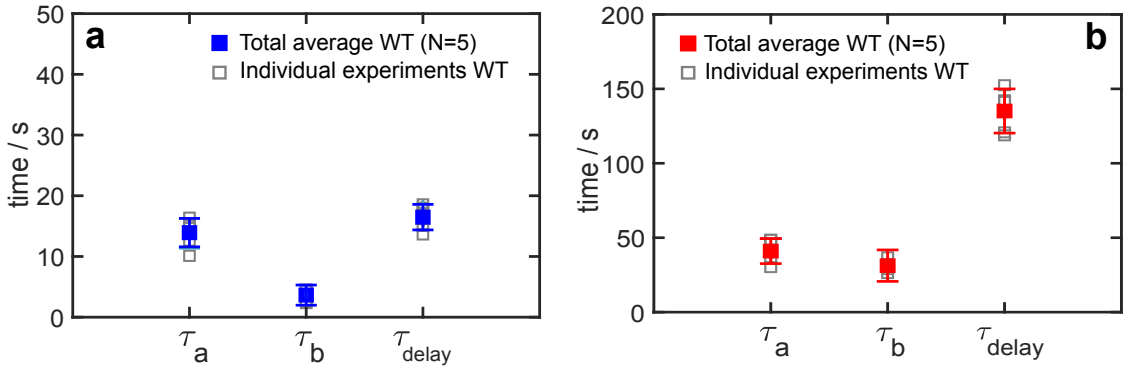


**Figure 4.9:** Time parameters deduced from the extended Langmuir model, which characterize the timescales associated to (a) adsorption and (b) desorption of WT *C. reinhardtii* cells (from images recorded at the bottom surface). The results are taken from $N = 5$ independent experiments. Open symbols indicate the average of single experiments, which comprises 5 to 6 consecutive adsorption-desorption cycles. Filled symbols indicate the mean of the $N$ independent experiments. The error bars illustrate the corresponding standard deviation. All the experiments were performed at a constant light intensity of $1 \cdot 10^{19}$ photons·m$^{-2} \cdot$ s$^{-1}$.

the desorption is more extended than the corresponding time interval for the adsorption process. This is supported by the quantification of the time parameters for adsorption and desorption given by best fits of the extended Langmuir model to the experimental data, as shown in Fig. 4.9. The results show that the value of $\tau_a$ for the desorption ($\tau_a = 36.0 \pm 5.5$ s) is, on average, about three times larger than the one for the adsorption ($\tau_a = 12.9 \pm 3.0$ s). The differences are even more remarkable for $\tau_{delay}$, which exhibits a value of $\tau_{delay} = 16.7 \pm 2.1$ s for adsorption and $\tau_{delay} = 135.4 \pm 21.4$ s for the desorption. The interpretation of this difference is discussed in Sec. 4.7. Lastly, the differences in the value of $\tau_b$ arise from its relation to $\tau_{delay}$. Nevertheless, the ratio $\tau_b \cdot \tau_{delay}^{-1} \approx 0.22$, which represents the relative cell-to-cell variability compared to the mean (i.e., $\tau_{delay}$), is similar in both adsorption and desorption.

In order to properly interpret the time parameters, the motility of the cells inside the experimental chambers needs to be considered. For this, I take into account the study by Fragkopoulos *et al.* [92], in which the positions of *C. reinhardtii* cells are tracked in a quasi-2-dimensional chamber. The average velocity of the cells inside the compartment is $100 \pm 30$ µm/s. From this, it is deduced that the cells can cover the vertical distance (300 µm) of the chamber of my adsorption experiments, on average, in about 3 s. In addition, *C. reinhardtii* cells exhibit run-and-tumble type of motion, with a short-time ballistic regime and a diffusive regime at longer times [128]. The transition between the two regimes has been calculated to occur at around 5 s, as obtained from the cells' mean squared displacement (MSD), see Fig. 4.10. This means that the length scale of the experimental setup in the vertical direction constrains the motion to be predominantly ballistic on the time scale for

the cells to interact with the substrate. As a result of this consideration, the physical meaning of $\tau_{\text{delay}}$ in my experiments can be attributed to the average time it takes for the cells to switch their flagellar adhesiveness, rather than the time to encounter a surface.

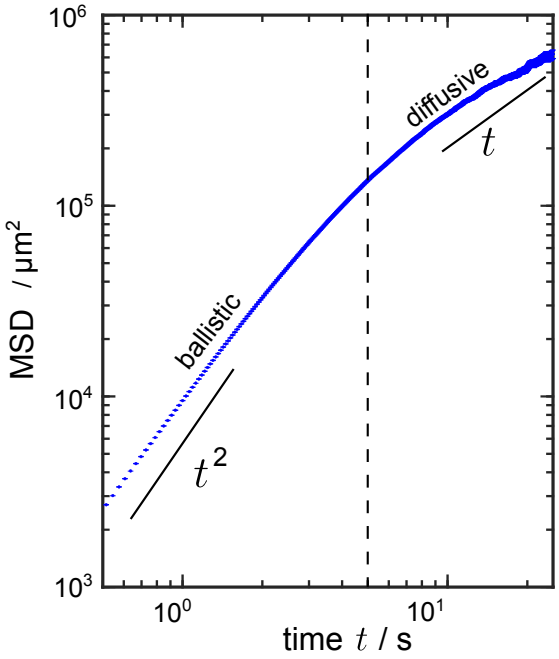


**Figure 4.10:** Different regimes of the swimming motility of *C. reinhardtii*. The MSD was calculated from 4600 independent cell trajectories with error bars representing the standard error. At short times, the motion of the cell is purely ballistic (MSD$\propto t^2$); at longer times, the motion becomes diffusive (MSD$\propto t$). The vertical dashed line illustrates the change from ballistic to diffusive motion.

## 4.5 Effect of phototaxis on the plateau density

As mentioned in Sec. 4.2, the WT *C. reinhardtii* cells show photophobic and phototactic responses when the light conditions are switched from red to blue. Right after switching to blue light, the cells in the suspension predominantly swim towards the light source; away from the bottom surface of the compartment. Around 3 s later, the cells exhibit negative phototaxis and reverse their orientation to swim downwards to the bottom boundary of the compartment, where they finally adsorb. The number of WT cells adsorbed at the bottom surface of the experimental chamber was found to be consistently larger than the number of cells on the top surface, as shown in Fig. 4.2. Given this remarkable asymmetry in the plateau densities at the top and bottom surfaces of the chamber, I decided to compute the ratio of the plateau densities taken at the top and bottom surfaces of the compartment, namely $\sigma_{\text{top}}/\sigma_{\text{bottom}}$. I did this using the WT strain SAG11-32b and its corresponding mutant, blind strain that has a deletion of ChR1 and ChR2 ($\Delta$ChR1,2), which

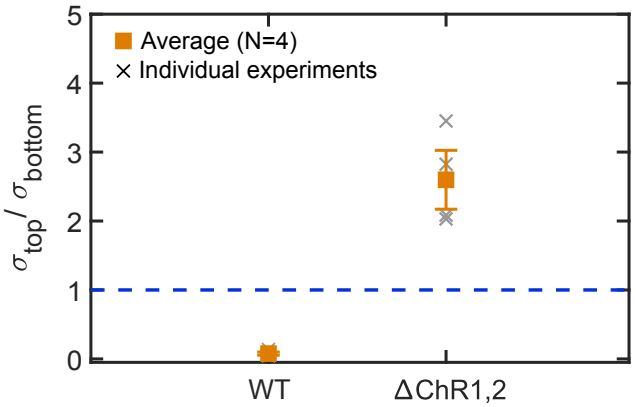


**Figure 4.11:** Phototaxis affects the density ratio of the adsorption. Comparison of the surface density ratio $\sigma_{top}/\sigma_{bottom}$ between the plateau densities of adsorbed cells at the top ($\sigma_{top}$) versus the corresponding density of adsorbed cells at the bottom ($\sigma_{bottom}$). Filled symbols denote mean values of 4 independent experiments and cross symbols denote the mean of single experiments, each comprising 6 runs of adsorption. The density ratio of the WT strain is equivalent to $0.08 \pm 0.04$, whereas for the ΔChR1,2 blind strain the corresponding ratio is equivalent to $2.6 \pm 0.4$. This shows that WT adsorb predominantly at the bottom surface of the experimental chamber, contrary to the blind strain.

are the blue-light sensitive photoreceptors mediating phototaxis, see Sec. 2.4.1. As shown in Fig. 4.11, the WT cells adsorb predominantly to the bottom surface of the chamber, with a density ratio of $0.08 \pm 0.04$. Conversely, the ΔChR1,2 blind strain exhibits a density ratio of $2.6 \pm 0.4$. This shows that phototaxis controls the surface density ratio of adsorbed cells in the experiments. Further results on the kinetics of adsorption of single- and double ChR-deleted *C. reinhardtii* is presented in the next chapter.

## 4.6 Effect of the light intensity on $\tau_a$ and $\tau_{delay}$

In the previous section it was shown that phototaxis influences the density ratio of adsorbed cells. In this section, I address the question whether phototaxis affects the kinetics of adsorption of *C. reinhardtii* at surfaces. To determine this, I study the dependence of the values of the parameters $\tau_a$ and $\tau_{delay}$ on the light intensity, contrasting the results obtained using WT and phototactically impaired cells. In such experiments, I follow the same protocols for data acquisition as for the experiments using constant light intensity, see Sec. 3.3.2, and now also recorded adsorption and desorption data for different light intensities, namely 0.5, 0.8, 1 and $2{\cdot}10^{19}$ photons$\cdot$m$^{-2} \cdot$ s$^{-1}$. The order of these light intensities were chosen randomly in order to avoid adaptation effects in these experiments, whose results are shown in Fig. 4.12, and highlight three important aspects.

First, the value of the parameter $\tau_a$ does not depend on the light intensity, as shown in Fig. 4.12a. The adsorption rate is mainly governed by the rate at which

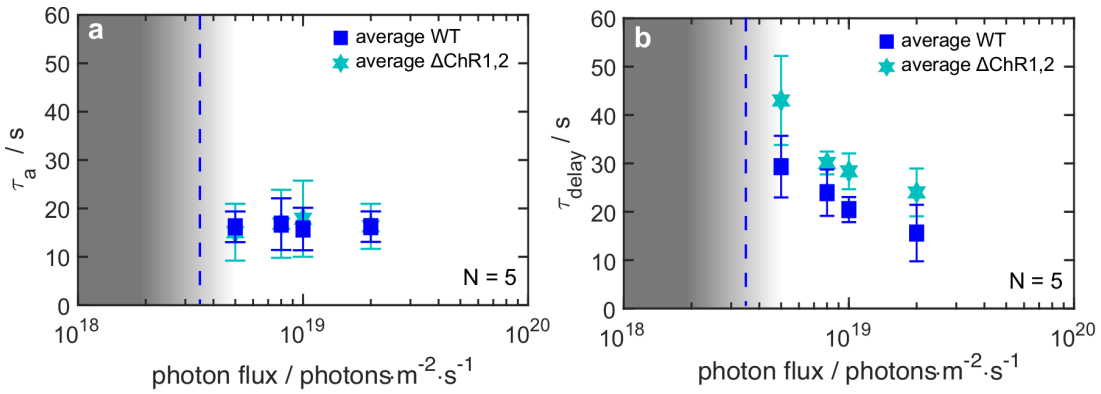


**Figure 4.12:** Light-intensity dependence of the time parameters (a) $\tau_a$ and (b) $\tau_{delay}$. Experiments were performed using WT *C. reinhardtii* cells (rectangles) as well as the ΔChR1,2 blind mutant (stars). Filled symbols indicate mean values of $N = 5$ independent adsorption experiments; error bars denote the corresponding standard deviation. For each experiment, 2-3 adsorption runs were obtained for each intensity. The grey-shaded gradient region between $2 \cdot 10^{18}$ photons·m$^{-2} \cdot$ s$^{-1}$ and $5 \cdot 10^{18}$ photons·m$^{-2} \cdot$ s$^{-1}$ represents the experimentally observed cell-to-cell variability of the intensity threshold of light-switchable adhesion [40]. The vertical dashed blue line highlights the mean of this light intensity threshold. In this transition regime, very few cells in the suspension are able to switch their adhesiveness, leading to non-sigmoidal and irregular adsorption curves, for which the extended Langmuir model could not be applied. For intensities below $2 \cdot 10^{18}$ photons·m$^{-2} \cdot$ s$^{-1}$ cells do not exhibit any adhesion. In contrast to the WT strain, measurements using the ΔChR1,2 strain were taken at the top surface of the experimental compartment as most of the cells adhere at the top boundary, see Fig. 4.11

.

the cells encounter the surface, which depends on their motility and the chamber's surface-to-volume ratio. Second, the time delay $\tau_{delay}$ monotonically decreases with increasing light intensity, see Fig. 4.12b. This result suggests that, in this regime of intensities, the time it takes to switch the flagellar adhesiveness of the cells on average increases as the light intensity decreases.

Third, both the WT and the channelrhodopsin-1,2 knockout strain exhibit consistent adsorption rates above the light-intensity threshold for surface adhesion, with values of $\tau_a = 16.4 \pm 0.4$ s for the WT and $\tau_a = 16.5 \pm 1.2$ s for the mutant strain, see Fig. 4.12a. In the case of the time delay $\tau_{delay}$, the values of the mutant strain are found to be systematically larger than corresponding values of the WT strain, see Fig. 4.12b.

## 4.7 Discussion

In this chapter I studied the adsorption and desorption of *C. reinhardtii* cells of the strain SAG11-32b and its corresponding mutant strain ΔChR1,2, see Sec. 3.1.2. I used particle detection and cell tracking to determine how the surface density of adsorbed cells varies with time as the cells are exposed to blue and red light. I quan-

tified the kinetics of adsorption and desorption by using a time-delayed Langmuir model, which considers four fit parameters: $\tau_a$, which quantifies the cells' adsorption/desorption rate; $\tau_{delay}$, which quantifies the time it takes 50% of the cells in the suspension to switch their flagellar adhesiveness; $\tau_b$, which is the error associated to $\tau_{delay}$ and is also a measure of the cell-to-cell variability of the cell population; and $\sigma_0$, which corresponds to the saturated surface density of adsorbed cells or plateau density.

The model accurately fits the experimental data, as shown in Fig. 4.8, and provides a reliable quantification of the fit parameters. The results show that that the adsorption is a process that occurs faster than the desorption. I hypothesize that the remarkable difference between the delay in the adsorption and desorption has its origin at the molecular level, where adhesive contact points between the flagella and the substrate are established. As mentioned in Sec. 2.3.3, the flagellar membrane glycoprotein FMG-1B is supposed to mediate the unspecific flagellar adhesion of *C. reinhardtii* to surfaces [109]. During the adsorption process, under blue light, the cells need only a few adhesion sites on the flagella to firmly adhere to the surface, as explained in Fig. 4.1. After the initial encounter of the surface, during which the flagella tips attach to the surface, the pulling phase starts and more adhesion sites are established with the surface, from the tip to the base of the flagella [40]. This process continues until the total extent of the flagella is in contact with the substrate. Subsequently, when the adsorbed cells are exposed to red light the desorption process begins when the flagella start disabling their adhesive contacts on the surface. The decreasing number of adhesive contact points leads to the recovery of flagellar beating, which becomes progressively more prominent until the cells detach and swim back to the suspension. Since the number of flagellar adhesive contacts is larger when the flagella are in full contact with the surface, the cells need more time to disable the contact points and overcome the flagella-substrate interaction forces. This mechanism might generate the difference in the extensions of the delay time of adsorption and desorption.

Regarding the results of the plateau density, $\sigma_0$, the suspensions used in the experiments consisted of a fixed cell density of $5 \cdot 10^6$ cells/mL, which corresponds to a cell volume fraction of $\phi \approx 0.1$. I chose this specific density to exclude three effects: First, smaller volume fractions may result in a very low surface coverage of adsorbed cells, which yields experimental data that appears noisy or that might not resemble the sigmoidal shape of adsorption/desorption curves presented in Fig. 4.5. Consequently, the relevant parameters obtained from the fit functions are less reliable in this regime of very low densities. Second, higher cell volume fractions might generate shadowing effects and, therefore, a non-homogeneous light intensity distribution in the suspension. Consequently, not all the cells would be exposed to the same light intensity. Third, high volume densities can also result in high surface

coverage, where gliding cells can develop clusters and interconnected networks that vary in time and increase the packing efficiency of the cellular monolayer on the surface [287]. Then, at longer times, new adsorption sites be populated by new cells, which violates a pre-condition of Langmuir-type adsorption. Therefore, a constant cell volume fraction of $\phi \approx 0.1$ yielded a suitable density to obtain reliable results. In fact, if every WT cell transitions from the swimming to the surface-associated state at the bottom surface, we expect to achieve a maximum surface density of about 1500-2000 cells/mm$^2$. This is confirmed by the experimental data shown in Fig. 4.8.

As for the phototactic responses, and unlike the WT *C. reinhardtii* cells, I do not find a measurable change in the direction of motion of the ΔChR1,2 mutant cells after switching from red to blue light. This indicates that blind cells exhibit neither (transient) photophobic nor (permanent) phototactic responses. This is consistent with the fact that ChR1 and ChR2 are the main photoreceptors regulating phototaxis in *Chlamydomonas* [194]. Contrary to the WT individuals, blind cells adhere mostly at the top surface of the compartment, as indicated by the values of the density ratio in Fig. 4.11. This is attributed to the fact that, in the mutant strain, photoresponses are absent and cannot counteract the natural negative gravitaxis of the cells, which originates from their bottom heaviness [149], see Sec. 2.3.4. This increases the population of cells swimming near the upper part of the compartment, which, after the change to blue-light conditions, increases the probability of cells adhering at the top rather than at the bottom surface of the compartment. From this result, the measure of the density ratio can be employed to quantify the interplay of phototaxis and gravitaxis in other strains.

Ultimately, a proper interpretation of the time parameters presented in this chapter is assessed by comparing the values of $\tau_\mathrm{a}$ and $\tau_\mathrm{delay}$ of WT and blind cells that are exposed to different light intensities. The results suggest that $\tau_\mathrm{a}$ is mainly governed by the rate at which the cells encounter the surface. This depends on the motility and the surface-to-volume ratio of the chamber. For the reported light intensities, however, the swimming motility of cells does not depend substantially on the light intensity [92] and, consequently, $\tau_\mathrm{a}$ is independent of the light intensity. In the case of $\tau_\mathrm{delay}$, the light-activated nature of the surface adhesion of cells implies that it takes longer for the cells' flagella to become adhesive as the light intensity is decreased. A decrease in the light intensity implies that there are less photons triggering the signalling pathway associated to switching the adhesion state of the flagella. In particular, for the highest light intensity used in the experiments, namely $2 \cdot 10^{19}$ photons$\cdot$m$^{-2} \cdot$ s$^{-1}$, the WT cells exhibit a delay time $\tau_\mathrm{delay} = 15.6 \pm 5.8$ s. This result agrees well with the typical timescales of the light-switchable flagellar adhesiveness (average value of $\tau_\mathrm{delay} = 10.9 \pm 9.2$ s) obtained from single-cell auto-adhesion experiments performed in white light at the same intensity [40].

Finally, the comparison between WT and the ΔChR1,2 mutant strain shows that phototaxis does not significantly affect the adsorption rate since value of the $\tau_a$ parameter does not vary with the light intensity. Nevertheless, the values of $\tau_{delay}$ exhibited by the ΔChR1,2 strain are systematically higher than the WT's, see Fig 4.12b. This could be explained by the absence of ChR1 and ChR2 affecting the transport of the adhesion-mediating protein FMG-1B along the flagella. Both ChRs are essential building-blocks of a signal-transduction pathway that is characterized by light-regulated $Ca^{2+}$ currents that take place in the eyespot, where ChR1 and ChR2 are located, and in the flagellar membrane [176]. Given that $Ca^{2+}$ currents are known to regulate the transport of the adhesive glycoproteins FMG-1B from the cell body to the flagella and vice versa [134, 135], the deletion of both ChRs could have potentially disrupted such signaling pathway and delayed the transport of FMG-1B to the flagella.

## 4.8 Summary of results

In this chapter, a reliable protocol has been established to study light-induced adsorption and desorption of WT and blind *Chlamydomonas* to surfaces. The adsorption is modelled using time-delayed Langmuir-type kinetics, from which four parameters are extracted: $\tau_b$, $\tau_a$, $\tau_{delay}$ and $\sigma_0$. The parameter $\tau_b$ measures the cell-cell variability of the studied cell population; $\tau_a$ gives a measure of the adsorption (or desorption) rate of cells to the surface; $\tau_{delay}$ indicates the time at which 50% of the cells in the population switch on or off their flagellar adhesiveness; and $\sigma_0$ quantifies the maximum number of adsorbed cells per unit area under blue light. The results obtained from adsorption experiments reveal that:

- The adsorption rate $\tau_a$ does not depend on the light intensity, whereas the time lag $\tau_{delay}$ monotonically decreases with increasing light intensity.
- The value of $\tau_{delay}$ exhibited by the WT strain in the desorption ($\tau_{delay} = 135.4 \pm 21.4$ s) is about an order of magnitude larger than the corresponding value for the adsorption ($\tau_{delay} = 16.7 \pm 2.1$ s).
- The value of $\tau_a$ exhibited by the WT in the desorption ($\tau_a = 36.0 \pm 5.5$ s) is, on average, about three times larger than the one for the adsorption ($\tau_a = 12.9 \pm 3.0$ s).
- Both the WT and ΔChR1,2 strains exhibit consistent adsorption rates above the intensity threshold, with values of $\tau_a \approx 16$ s. However, the values for $\tau_{delay}$ are systematically higher for the non-phototactic mutant strain.
- After the cells in the suspension are exposed to blue light, all the cells adsorb to the surface until a plateau density $\sigma_0$ is attained. The cells remain attached

to the surface, in the gliding configuration, until they are illuminated with red light. Phototaxis biases the preference of WT cells to adsorb at the bottom surface. This is supported by experiments comparing the plateau density $\sigma_{\mathrm{top}}/\sigma_{\mathrm{bottom}}$ exhibited by WT and non-phototactic mutant strains that lack ChR1 and ChR2, the photoreceptors accounting for phototaxis.

# Chapter 5

# Light-switchable adhesion of ChR- and PHOT-deletion mutants

In order to maximize the energy input for photosynthesis, *C. reinhardtii* cells perform phototaxis to reach areas with optimal illumination. If the cells encounter a solid surface in such areas, they may colonize them via light-switchable adhesion. Although it was shown in the previous chapter that the blind strain, ΔChR1,2, still exhibits light-switchable adhesion, it is worth evaluating whether there are significant differences in the adsorption kinetics and the interaction of cells to surfaces when only one of the ChRs is deleted. In this chapter, I present the first results on adsorption experiments, complemented with single-cell micropipette force measurements using the mutant strains ΔChR1, ΔChR2 and the blind strain ΔChR1,2. Additionally, I also present results using a PHOT-deletion mutant, as PHOT is a photoreceptor known to prevail in the flagella of *C. reinhardtii*.

## 5.1 Adsorption results

### 5.1.1 Channelrhodopsin-deletion mutants

Adsorption experiments were performed using ΔChR1, ΔChR2 and ΔChR1,2[1] deletion mutants following the established protocol in Sec. 3.3. Figure 5.1 highlights the results on the ChR mutants. The obtained results are also compared with the ones obtained from the adsorption experiments using the WT strain (SAG11-32b), see Fig. 4.4. A list of the values of the time parameters presented in Fig. 5.1 is also provided in Table 5.1.

In the case of the adsorption results, the overall features of the kinetics are similar between the strains, see Fig. 5.1a. In fact, there are no significant differences between the ChR-deletion mutants and the WT strain, as all the time parameters

[1]Experiments using ΔChR1,2 were performed by Nicolas von Trott, whom I supervised during the winter semester 2020/2021 at the University of Göttingen.

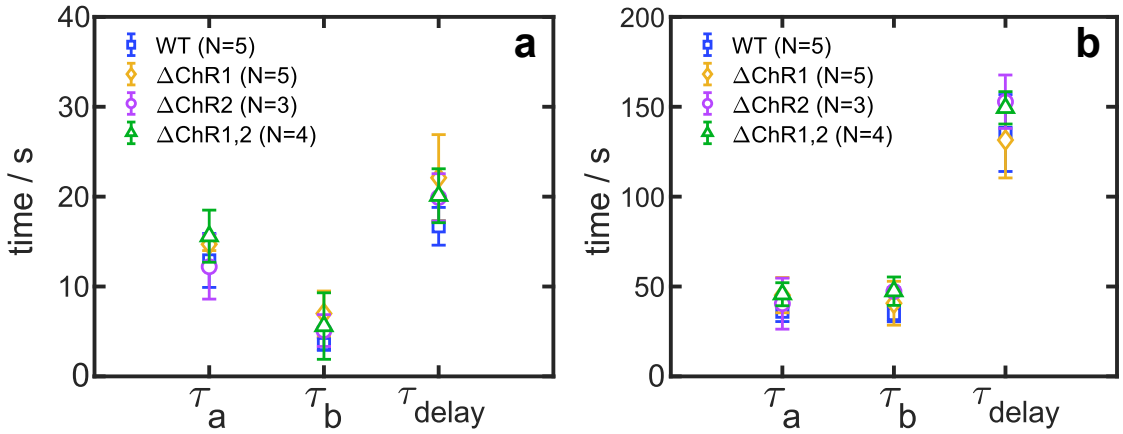


**Figure 5.1:** Fit parameters obtained from (a) adsorption and (b) desorption experiments using ChR-deletion mutants. The results for the WT strain SAG11-32b are shown for comparison. The parameters were obtained from adsorption and desorption curves using the extended Langmuir model, see Sec. 4.3. Markers assigned for each studied strain represent the mean of N independent experiments. For each experiment, 4-6 runs of measurements are collected. Error bars represent the standard deviation of the mean. The light intensity was set to $1{\cdot}10^{19}$ photons$\cdot$m$^{-2}\cdot$s$^{-1}$.

are within error.

| Strain | $\tau_a$ (s) | $\tau_b$ (s) | $\tau_{delay}$ (s) |
|---|---|---|---|
| SAG11-32b | 12.9±3.0 | 3.6±0.7 | 16.7±2.1 |
| ΔChR1 | 14.7±0.7 | 6.6±2.2 | 21.3±3.2 |
| ΔChR2 | 12.2±3.6 | 5.1±1.8 | 19.1±2.6 |
| ΔChR1,2 | 15.6±2.9 | 5.6±3.7 | 20.1±3.0 |

**Table 5.1:** Time parameters of ChR-deletion mutants compared to the adsorption parameters of the WT strain. The value of each parameter is obtained from the results of adsorption experiments shown in Fig. 5.1a.

Interestingly, the WT strain exhibits the fastest switching response (lowest $\tau_{delay}$), showing that the loss of any of the two ChRs results in a delay of light-switchable adhesion. In fact, the loss of either ChR1 or ChR2 seems to result in cells that exhibit an almost-identical switching behavior as the blind strain ΔChR1,2.

Figure 5.1b and Table 5.2 show the parameters for desorption of ChR-deletion mutants. Regarding the parameter $\tau_a$, the strains ΔChR1 and ΔChR1,2 exhibit lower rates of desorption compared to the WT strain. A conclusive remark is difficult to provide for the ΔChR2 strain, given the high spread of the values of the desorption rate. In the case of the $\tau_{delay}$ parameter ΔChR2 and the blind strain ΔChR1,2, on average, exhibit longer times with a smaller variability for flagellar detachment from the surface, compared to both WT and ΔChR1. Nevertheless, the values of the $\tau_{delay}$ parameter are still within error and a specific trend cannot be concluded.

The influence of phototaxis on the plateau density ratio $\sigma_{top}/\sigma_{bottom}$ was also assessed during adsorption experiments, see Fig. 5.2. When cells of the strains ΔChR1

| Strain | $\tau_a$ (s) | $\tau_b$ (s) | $\tau_{delay}$ (s) |
|---|---|---|---|
| SAG11-32b | 36.0 ± 5.5 | 34.7 ± 4.3 | 135.4 ± 21.4 |
| ΔChR1 | 45.2 ± 9.8 | 38.7 ± 13.1 | 131.5 ± 21.1 |
| ΔChR2 | 40.5 ± 14.2 | 47.2 ± 2.2 | 152.8 ± 36.4 |
| ΔChR1,2 | 45.7 ± 6.4 | 47.4 ± 7.9 | 149.4 ± 9.0 |

**Table 5.2:** Time parameters of ChR-deletion mutants compared to the adsorption parameters of the WT strain. Time parameters are obtained from the results of desorption experiments shown in Fig. 5.1b.

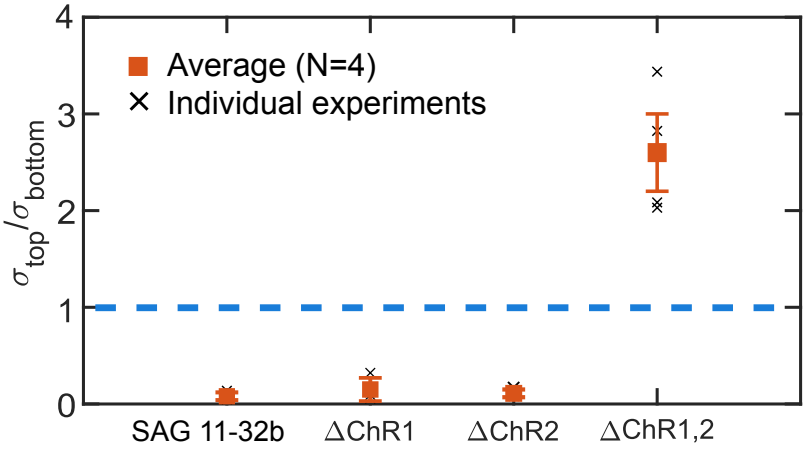


**Figure 5.2:** Plateau density ratios exhibited by the WT and ChR-deletion mutants. A total of N=4 independent experiments were considered for each strain. The measurement of the plateau densities at the top and bottom surfaces of the experimental chamber was conducted at the end of 4-6 consecutive runs for each experiment.

and ΔChR2 are illuminated with blue light, they also exhibit a transient swimming motion towards the light source, i.e. away from the bottom surface of the chamber, just like the WT strain. After around 3-5 s, the mutant cells exhibit negative phototaxis and swim away from the light source until they encounter the bottom boundary of the chamber and become attached to it by their flagella. This means that the loss of one of the ChRs photoreceptors does not impair the phototactic behavior of *C. reinhardtii*.

As shown in Fig. 5.2, the WT and single ChR-deletion strains exhibit values of the ratio below one, indicating that the vast majority of the cells in the suspension adsorbs at the bottom surface of the chamber under blue light. Only the deletion of both ChR1 and ChR2 disrupts the phototactic response and, thus, gravitaxis dominates and the cells preferentially attach to the top of the compartment, as discussed in Sec. 4.7.

### 5.1.2 Phototropin-deletion mutants

Figure 5.3 presents the results of adsorption and desorption experiments performed using the strain ΔPHOT, which lacks the photoreceptor phototropin. The results

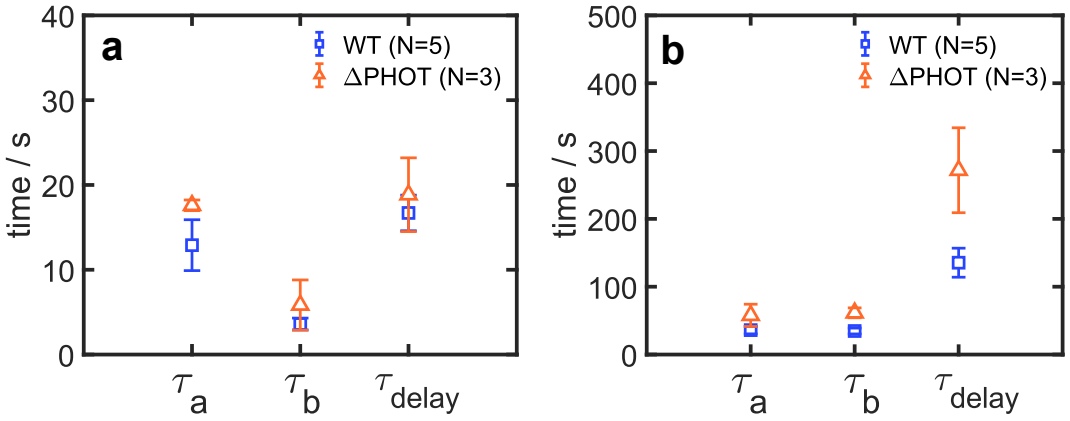


**Figure 5.3:** Fit parameters obtained from (a) adsorption and (b) desorption experiments using a PHOT deletion mutant, ΔPHOT. The results obtained from experiments using the WT strain SAG11-32b are displayed for comparison. The parameters were obtained from adsorption and desorption curves using the extended Langmuir model, see Eq. 4.5 and 4.6. Markers assigned for each studied strain represent the mean of N independent experiments. For each experiment, 4-6 runs of consecutive measurements are collected. Error bars correspond to the standard deviation of the mean. The light intensity was set to $1{\cdot}10^{19}$ photons$\cdot$m$^{-2}\cdot$s$^{-1}$.

reveal that all the time parameters exhibited by the surface adsorption of the PHOT mutant strain are systematically higher in both the adsorption and the desorption, compared to the WT strain. In other words, the deletion of PHOT results in longer times for the cells to switch on or off their flagellar adhesiveness, as well as a slower rate of adsorption and desorption. The time parameters for the adsorption and desorption are provided in Table 5.3 and Table 5.4, respectively.

The most remarkable result is shown in Fig.5.3b, where the value of $\tau_{\text{delay}}$ for the desorption of ΔPHOT cells is practically twice the one exhibited by the WT. This means that *C. reinhardtii* cells lacking PHOT need to spend a time that is twice as much as the WT to remove the contact points between the flagella and the substrate before returning to the planktonic state.

| Strain | $\tau_a$ (s) | $\tau_b$ (s) | $\tau_{\text{delay}}$ (s) |
|---|---|---|---|
| SAG11-32b | 12.9 ± 3.0 | 3.6±0.7 | 16.7±2.1 |
| ΔPHOT | 17.6 ± 0.6 | 5.8±3.0 | 18.6±4.4 |

**Table 5.3:** Comparison of the time parameters of the ΔPHOT and the WT strain, obtained from the results of adsorption experiments shown in Fig. 5.3a.

| Strain | $\tau_a$ (s) | $\tau_b$ (s) | $\tau_{\text{delay}}$ (s) |
|---|---|---|---|
| SAG11-32b | 36.0 ± 5.5 | 34.7 ± 4.3 | 135.4 ± 21.4 |
| ΔPHOT | 57.8 ± 16.4 | 61.5 ± 7.4 | 271.7 ± 62.6 |

**Table 5.4:** Comparison of the time parameters of ΔPHOT and the WT strain, obtained from results of desorption experiments presented in Fig. 5.3b.

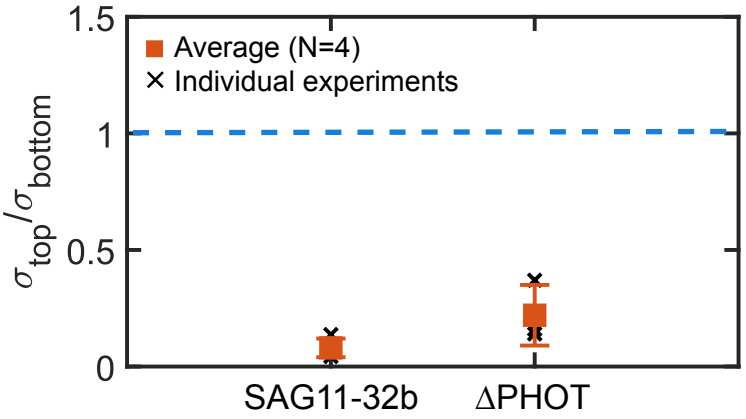


**Figure 5.4:** Plateau density ratio exhibited by the WT strain SAG11-32b and the PHOT-deletion mutant. A total of N=4 independent experiments were considered for each strain. Filled markers represent the mean of the N independent experiments. Error bars denote standard deviations. Black crosses represent the average value of the density ratio measured after 4-6 consecutive runs of individual adsorption experiments.

The phototactic responses are not inhibited for the ΔPHOT strain. After switching from red to blue light, the cells also exhibit a transient directed motion towards the light source, and, after a few seconds, they reverse their orientation and swim downward in the compartment. Once the cells encounter the bottom boundary, several of them transiently adhere to the substrate but do not manage to achieve the gliding configuration and then leave the surface to adhere somewhere else. This makes the analysis of adsorption experiments using the ΔPHOT strain rather challenging since several of the adsorption curves obtained did not exhibit a clear sigmoidal shape. For those adsorption curves, the extended Langmuir model could not be applied and, thus, the curves had to be excluded. Nevertheless, at longer times a plateau density is reached, where most of the cells adhere at the bottom surface of the chamber. This is revealed by the plateau density ratio for this strain, see Fig. 5.4. Interestingly, ΔPHOT has a plateau density ratio of about 0.22, which is almost three times the density ratio exhibited by the WT strain, which is about 0.08.

## 5.2 Force measurements results

Now that the kinetics of desorption has been presented, I describe the complementary results obtained by micropipette force measurements using the mutant strains ΔChR1, ΔChR2, ΔChR1,2 and ΔPHOT. Force measurements using these strains were conducted following the protocol described in Sec. 3.2.4. Each measured cell was kept under blue ($\lambda = 470/10$ nm) or red light ($\lambda = 671/10$ nm) for five minutes before the start of the force measurements. After this incubation time, the cell undergoes a cycle of 5 force-distance measurements. Once these measurements were completed, a new illumination condition was set. The order of the illumina-

tion conditions was randomly selected for each cell in order to prevent adaptation effects. Each cell is exposed twice to both blue and red light, obtaining a total of 10 force-distance measurements for each cell and for each wavelength. The mean adhesion force is calculated for each cell and is used to construct the boxplots shown in Fig. 5.5. Micropipette force measurements for the presented strains were conducted by Dr. Antoine Girot.

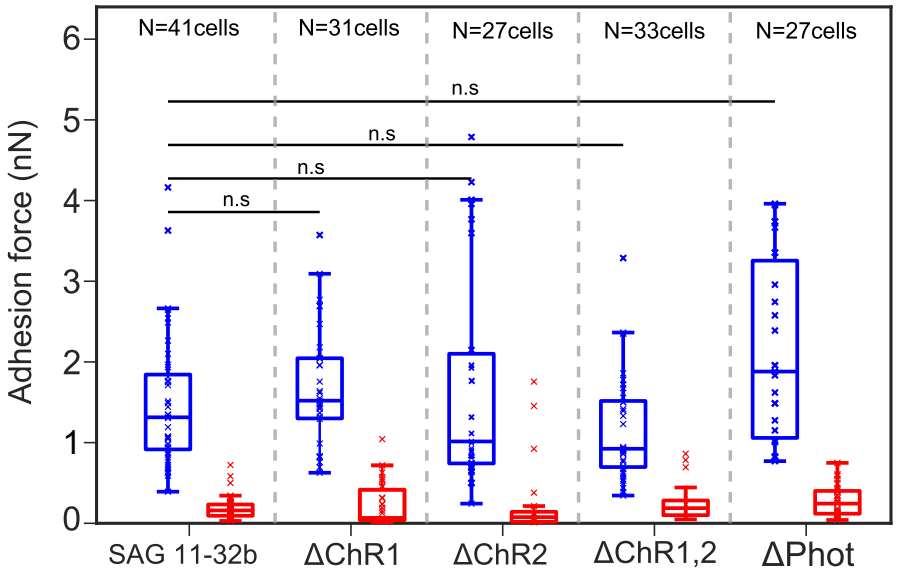


**Figure 5.5:** Boxplots showing the distribution of flagellar adhesion forces of the WT strain SAG11-32b, ChR- and PHOT-deletion mutants. A total of N single-cell force measurements is considered for each strain. A two-sample Kolmogorov-Smirnoff test (see Sec. 3.2.5) was performed to assess for significant differences in the distribution of adhesion forces. The comparison is always conducted with respect to the WT strain. The results show that there are non-significant (n.s) differences in the distribution of adhesion forces under blue light. All strains switch to effectively zero adhesion under red light. Courtesy of Dr. A. Girot.

As expected from the adsorption experiments, light-switchable adhesion is seen in all the tested strains. The force measurements performed in blue light show that the distribution of adhesion forces of all strains lie in a range between 0.24-4 nN, with median values around 1-2 nN for each strain. Under red light, the adhesion forces are reduced to almost 0 nN. Interestingly, the distribution of adhesion forces of ΔPHOT is more spread, which indicates higher cell-to-cell variability and the occurrence of higher adhesion forces. Overall, the force measurements reveal that there are no significant differences in the distribution of adhesion forces exhibited by any of the mutant strains addressed, relative to the ones exhibited by the WT strain.

## 5.3 Discussion

In this chapter, adsorption experiments and micropipette force measurements were conducted using ChR- and PHOT-deletion mutants. The results obtained from experiments probing the ChR-deletion mutants show that, overall, phototaxis does not play a major role in the kinetics of adsorption of *C. reinhardtii*. Nevertheless, there are several interesting features to discuss.

When the cells are exposed to blue light, all the strains but the blind mutant ΔChR1,2 exhibit phototactic responses. Phototactic responses are characterized by a transient swimming of cells towards the light source, which is followed by the reversion of the cells' orientation around 3-5 s seconds after exposure to blue light. ΔChR1 and ΔChR2 cells exhibit negative phototaxis as they mostly adsorb to the bottom of the chamber, in contrast with ΔChR1,2, see Fig. 5.2.

The change from upward swimming to downward swimming must be driven by phototactic responses triggered in the eyespot of the cells. It is known that calcium currents in the eyespot of *Chlamydomonas* regulate the beating of the *cis*-flagellum, which changes the orientation of the swimming cells [288]. This phenomenon is mediated by ChRs [176] and, thus, this might slightly (although not significantly) modify the kinetics of adsorption of ChR deletion mutants relative to the WT strain.

The values of the parameter $\tau_{\mathrm{a}}$ are not significantly different between ChR-deletion mutants and the WT strain. Since the parameter characterizes the time it takes for the cells to attach after they have switched their flagellar adhesiveness,$\tau_{\mathrm{a}}$ is partially controlled by the strength of the adhesion force. As I did not find significant differences in the full distribution of adhesion forces, it is reasonable that the $\tau_{\mathrm{a}}$ values are also similar among strains.

Regarding the results obtained from the parameter $\tau_{\mathrm{delay}}$ under blue light, the disruption of any of the ChRs results in longer switching times of the flagellar adhesion, as the average values of $\tau_{\mathrm{delay}}$ are above the corresponding average for the WT. This could suggest that ChR-mediated calcium signaling might be involved in light-switchable adhesion, though independently from the mechanism triggering the adhesion, as ΔChR1,2, cells still can still adhere to surfaces under blue light. In fact, ChRs are essential components of a signal-transduction pathway characterized by calcium currents occurring in the eyespot and the flagellar membrane [179]. Calcium currents are known to regulate the transport of adhesion-mediating glycoprotein FMG-1B from the cell body to the flagella and *vice versa* [134], and thus, the deletion of one or two ChRs might result in longer switching times of flagellar adhesion.

As for the desorption, the results show that the deletion of ChR2 could lead to longer times for flagella detachment, as ΔChR2 mutants show a higher average value of $\tau_{\mathrm{delay}}$ than the WT and the ΔChR1 strains. Furthermore, the deletion of ChR2 results in a delay time comparable to the one exhibited by the blind mutant ΔChR1,2. Flagellar detachment is mediated by elevations in intraflagellar calcium

[135], which is needed to disrupt the interaction between flagellar membrane glycoproteins (FMGs) and IFT trains. It might occur that ChRs are involved in a signaling response related to flagella detachment, for which ChR2 is a dominant regulator, as only when ChR2 is present in *C. reinhardtii* (i.e. ChR1 is deleted) the average value of the delay parameter is comparable to the WT's. Nevertheless, it is difficult to justify an implication between the deletion of ChRs and the time it takes the cells to detach their flagella, as ChRs are not proteins that are sensitive to red light [171]. However, below I discuss a relation between ChR1 and PHOT that could suggest the implication of ChR1 with flagellar detachment.

ΔPHOT cells exhibit systematically higher values for the time parameters in both adsorption and desorption. Up to date, there are no systematic studies that report the role of PHOT in the motility and the adhesion of *C. reinhardtii*. Interestingly, ΔPHOT cells exhibit an extended delay time during the desorption, which is around two times the delay exhibited by the WT cells. This result is important since PHOT is a photoreceptor known to be localized in the flagella of *C. reinhardtii* [259]. As a consequence of this, its deletion could have a higher impact on the dynamics of flagellar detachment from surfaces. Additionally, it has been reported that lower amounts of PHOT lead to an increase of ChR1 in *Chlamydomonas* [262]. It might occur that the systematically higher values for the time parameters obtained from adsorption and desorption experiments are caused not only by the loss of PHOT but also because of the increase of ChR1 in PHOT-deletion cells. Specifically, the upregulation of ChR1 after the deletion of PHOT may be the reason behind the larger values exhibited by $\tau_{\text{delay}}$ during desorption, see Fig. 5.3b. This might suggest a direct implication of ChR1 in the regulation of flagellar detachment from surfaces.

With respect to the plateau density ratio $\sigma_{\text{top}}/\sigma_{\text{bottom}}$, the higher values exhibited by the ΔPHOT mutant ($\sigma_{\text{top}}/\sigma_{\text{bottom}} = 0.22$), compared to the WT strain ($\sigma_{\text{top}}/\sigma_{\text{bottom}} = 0.08$), indicate that the extent of negative phototaxis is diminished after the deletion of PHOT in the WT strain. This is not intuitive in light of the upregulation of ChR1, as cells with more ChR1 should exhibit more negative phototaxis. Experiments reporting a change in the sign of phototaxis as a consequence of PHOT deletion and a subsequent increase in ChR1 have not been conducted.

Micropipette force measurements indicate that all the mutant strains studied do not regulate light-switchable adhesion in *C. reinhardtii* significantly. This is illustrated in the non-significant differences in the distribution of adhesion forces among the strains. The median of the force distributions exhibited by all strains, under blue light, lies around 1-2 nN. ΔPHOT exhibits higher cell-cell variability, as shown by a more spread force distribution than the rest of the strains.

## 5.4 Summary of results

In this chapter, adsorption experiments and micropipette force measurements were performed using the mutant strains ΔChR1, ΔChR2, ΔChR1,2, and ΔPHOT. The photoreceptors ChR1 and ChR2, are known to be involved in phototactic responses of *Chlamydomonas*, whereas PHOT is known to be localized in the cells' flagella and to regulate the sexual life cycle of the cells, see Sec. 2.4. The results obtained in this chapter reveal that:

- The deletion of either ChR1, ChR2 or PHOT does not disrupt phototactic responses of WT *C. reinhardtii*. In fact, these strains experience negative phototaxis under blue light, which forces them to adsorb mainly at the bottom boundary of the chamber.
- Phototaxis is completely inhibited by the deletion of ChR1 and ChR2, which causes the cells to preferentially attach to the top surface of the chamber.
- Although ΔPHOT cells adsorb predominantly at the bottom of the chamber, more cells adsorb to the top surface compared to the WT.
- The time parameters of the adsorption kinetics are, in general, similar between WT and ChR-deletion mutants.
- The deletion of ChR2 leads to longer times for flagella detachment, comparable to the blind strain lacking both ChR1 and ChR2.
- It might be that ChR1 and ChR2 control some aspects of light-switchable adhesion, although they are not essential to this phenotype, as the blind strain ΔChR1,2 still can adhere to surfaces under blue light.
- Compared to the WT, ΔPHOT exhibits longer switching times of flagellar adhesiveness (i.e. delay time) during adsorption and desorption, and also longer adsorption rates. Particularly remarkable is the fact that the deletion of PHOT leads to an extended delay for desorption, which is two times the delay time exhibited by WT cells.
- The force measurements in blue light show that the median of the distribution of adhesion forces exhibited by all the strains lies in a range between 1-2 nN.
- The distribution of adhesion forces exhibited by ΔPHOT features a higher cell-cell variability compared to the distribution of the WT and ChR-deletion mutants.
- Under red light, the distribution of adhesion forces is reduced to effectively zero adhesion in all strains.

- As shown by adsorption experiments and by micropipette force measurements, I conclude that ChR1, ChR2, and PHOT, are not the photoreceptors responsible for the light-switchable adhesion phenotype in *C. reinhardtii*.

# Chapter 6

# Adhesion of CRY-deletion mutants to surfaces

Along their evolutionary history, photoactive microorganisms have evolved sensitivity to certain ranges of light wavelengths, which control specific phenotypes and molecular processes within the cells [171, 289]. In the case of *Chlamydomonas*, previous experiments suggest that light-switchable adhesion is triggered by a blue-light photoreceptor, as shown by a rough color discrimination to assess the dependence of flagellar adhesion forces on light [40]. In this chapter, I present a more detailed action spectrum for light-switchable adhesion in *Chlamydomonas*. The elucidation of the action spectrum for this phenotype is highly relevant, as it motivates the deletion of specific photoreceptors from the cell's genome, namely plant- and animal cryptochromes, see Sec 2.4.2. Adsorption and force measurement results using CRY-deletion mutants are presented. Finally, I comment on preliminary results to assess that cryptochromes are involved in light-switchable adhesion of another widely-used *C. reinhardtii* WT strain.

## 6.1 Action spectrum of light-switchable adhesion

The action spectrum of the light-switchable adhesion has been determined by adsorption experiments[1] and micropipette force measurements[2]. During adsorption experiments, WT cells are exposed to different light wavelengths using a set of 12 bandpass filters, see Appendix A.1. In each independent experiment, the cells are exposed to a selection of 3-4 wavelengths for which 4-6 runs of adsorption are recorded. A total of 3-4 independent experiments were performed for each wavelength. To avoid adaptation effects, the order of the light conditions was randomly selected in every experiment. The light intensity in all experiments was set to $1{\cdot}10^{19}$ photons$\cdot$m$^{-2}\cdot$s$^{-1}$.

[1] Adsorption experiments to determine the action spectrum were conducted by Theresa Büttner.
[2] Force measurements for the action spectrum were conducted by Dr. Antoine Girot.

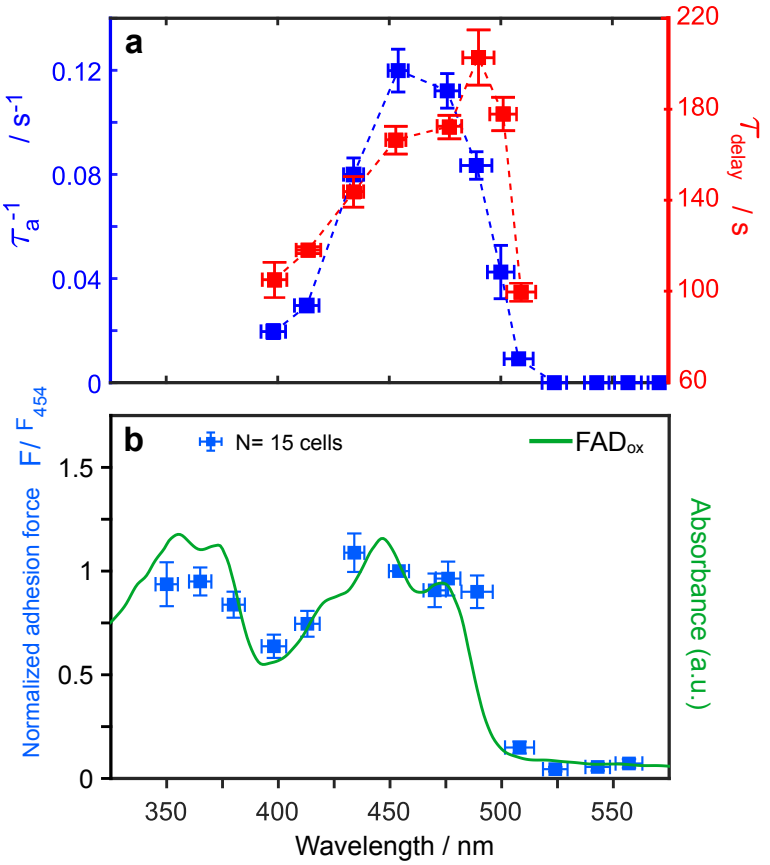


**Figure 6.1:** Action spectra of the light-switchable adhesion of *C. reinhardtii*. (a) The adsorption rate $\tau_a^{-1}$ (blue) exhibits a peak at 454 nm and the $\tau_{delay}$ parameter (red) for the desorption exhibit a peak at 489 nm. Filled marks represent the mean taken from 3-4 independent experiments. Vertical bars represent standard deviation and horizontal bars represent the half width of the bandpass filter. (b) Normalized adhesion forces, obtained from micropipette force measurements, exhibit higher values under blue and UV exposure. The maximum adhesion is obtained at $\lambda = 454$ nm. An absorption spectrum [220] is also presented to highlight the similarities of the adhesion response with the light sensitivity of CRY photoreceptors. Vertical bars denote the mean of 15 independent experiments and horizontal bars represent the half width of the bandpass filter. Courtesy of T. Büttner and Dr. A. Girot.

The results obtained from the adsorption experiments are explained based on the inverse of the $\tau_a$ parameter, i.e. the adsorption rate, which provides a more visually-appealing interpretation of the results compared to $\tau_a$. Indeed the results illustrated in Fig. 6.1a show that the adsorption rate reaches a maximum when the cells are exposed to a wavelength of 454 nm. An abrupt decrease in this parameter is observed for cells exposed to wavelengths above 476 nm and below 489 nm. Once the adsorbed cells are exposed to red light, the delay parameter $\tau_{delay}$ also exhibits similar features as $\tau_a^{-1}$, although the peak of $\tau_{delay}$ is at 489 nm. The interpretation of this result is discussed in Sec. 6.6.

For wavelengths below $\lambda = 454$ nm the parameters $\tau_a^{-1}$ and $\tau_{delay}$ do not fall rapidly to zero when the cells are exposed to near-UV light, as opposed to cells

exposed to wavelengths above 500 nm, which do not adsorb to the surface. This motivated further experiments below 390 nm, as it is known that there are photoreceptors that are sensitive to UV wavelengths, see Sec. 2.4.2. However, the experimental setup used in adsorption experiments did not allow to conduct proper studies in the UV range, as the cross-section of a focused UV light was smaller than the diameter of the experimental chamber. Therefore, complementary single-cell micropipette force measurements were also conducted. The setup employed for force measurements using UV light is described in Fig. 3.7.

During the force measurements, a single cell was exposed to a series of 13 randomly selected wavelengths during one entire experiment. The cells were incubated for 5 minutes under a specific wavelength before the start of the measurements. For each wavelength, a set of 10 force measurements was collected at a constant light intensity of $1{\cdot}10^{19}$ photons$\cdot$m$^{-2}\cdot$s$^{-1}$. The mean value of the adhesion forces, measured from a total of 15 cells, is then calculated. The results are shown in Fig. 6.1b.

The action spectrum of the adhesion forces exhibits similar features to the spectrum obtained from adsorption measurements under the studied range of wavelengths. The rapid decay of the adhesion force for wavelengths above 500 nm is consistent with the cells showing no adsorption under red-shifted wavelengths. Even more interesting is that the action spectrum for the adhesion forces strongly resembles the absorption spectrum of a flavin adenine dinucleotide (FAD) chromophore [220], see Fig. 2.10. Particularly, the spectrum is in good agreement with the oxidized state of the FAD chromophore, termed $\text{FAD}_{\text{ox}}$. As this chromophore is known to be the light-sensitive cofactor of cryptochromes (CRYs), we decided to conduct further adsorption measurements using CRY-deletion mutants.

## 6.2 Cryptochromes are involved in the flagellar adhesion of *C. reinhardtii*

### 6.2.1 Adsorption kinetics results

Adsorption experiments were performed using single CRY knock-out strains, namely aCRY and pCRY, see Sec. 2.4.2. The results are illustrated in Fig. 6.2 and the values for the fit parameters for the adsorption and desorption are given in Tab. 6.1 and Tab. 6.2, respectively.

The kinetics of adsorption and desorption kinetics of CRY mutants is comparable to the one exhibited by the WT strain. It seems that the $\Delta$aCRY strain exhibits slower desorption rates, as it shows a higher average value of $\tau_{\text{a}}$ than $\Delta$pCRY and the WT strain. Nevertheless, the kinetics of adsorption and desorption remain unaltered with the deletion of one of the CRYs as all the results are within standard errors. Considering that certain light-controlled phenotypes require two components to be

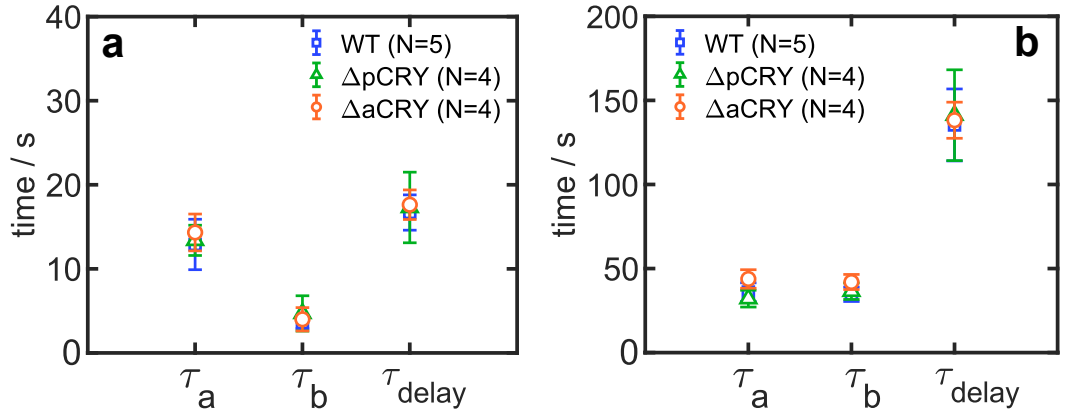


**Figure 6.2:** Fit parameters obtained from (a) adsorption and (b) desorption experiments using CRY-deletion mutants. The results for the WT strain SAG11-32b are shown for comparison. The parameters were obtained from adsorption and desorption curves using the extended Langmuir model, see Sec. 4.3. Markers assigned for each strain represent the mean of N independent experiments. For each experiment, 4-6 runs of measurements are collected. Error bars represent the standard deviation of the mean. The light intensity was set to $1{\cdot}10^{19}$ photons$\cdot$m$^{-2}\cdot$s$^{-1}$.

expressed, such as ChR1 and ChR2 controlling phototaxis in *Chlamydomonas* (see Sec. 2.4.1), I considered using a double-CRY mutant strain, labeled Δa,pCRY, which has a deletion of both aCRY and pCRY photoreceptors.

| Strain | $\tau_a$ (s) | $\tau_b$ (s) | $\tau_{delay}$ (s) |
|---|---|---|---|
| SAG11-32b | 12.9±3.0 | 3.6±0.7 | 16.7±2.1 |
| ΔpCRY | 17.6±0.6 | 4.7±2.1 | 17.3±4.2 |
| ΔaCRY | 14.3±2.2 | 2.2±1.4 | 17.6±1.8 |

**Table 6.1:** Comparison of the adsorption time parameters of single CRY mutants and the WT strain, obtained from the results of adsorption experiments shown in Fig. 6.2a.

| Strain | $\tau_a$ (s) | $\tau_b$ (s) | $\tau_{delay}$ (s) |
|---|---|---|---|
| SAG11-32b | 36.0±5.5 | 34.7±4.3 | 135.4±21.4 |
| ΔpCRY | 32.1±5.0 | 36.5±4.9 | 141.2±26.9 |
| ΔaCRY | 43.8±5.4 | 47.4±4.5 | 138.2±10.7 |

**Table 6.2:** Comparison of the time parameters for the desorption of single CRY mutants and the WT strain, obtained from the results of desorption experiments shown in Fig. 6.2b.

The adsorption results for the double-CRY deletion mutant are presented in Fig. 6.3. The obtained results illustrate a remarkable disruption of the adsorption of the cells to the surface of the chamber. The cells were exposed to blue light, and three different light intensities, namely 1, 3, and $5{\cdot}10^{19}$ photons$\cdot$m$^{-2}\cdot$s$^{-1}$, were imposed in order to identify any shifting of the intensity threshold for the flagellar adhesion switch. A total of four independent experiments were performed, for which 3 runs of adsorption were recorded under each light intensity.

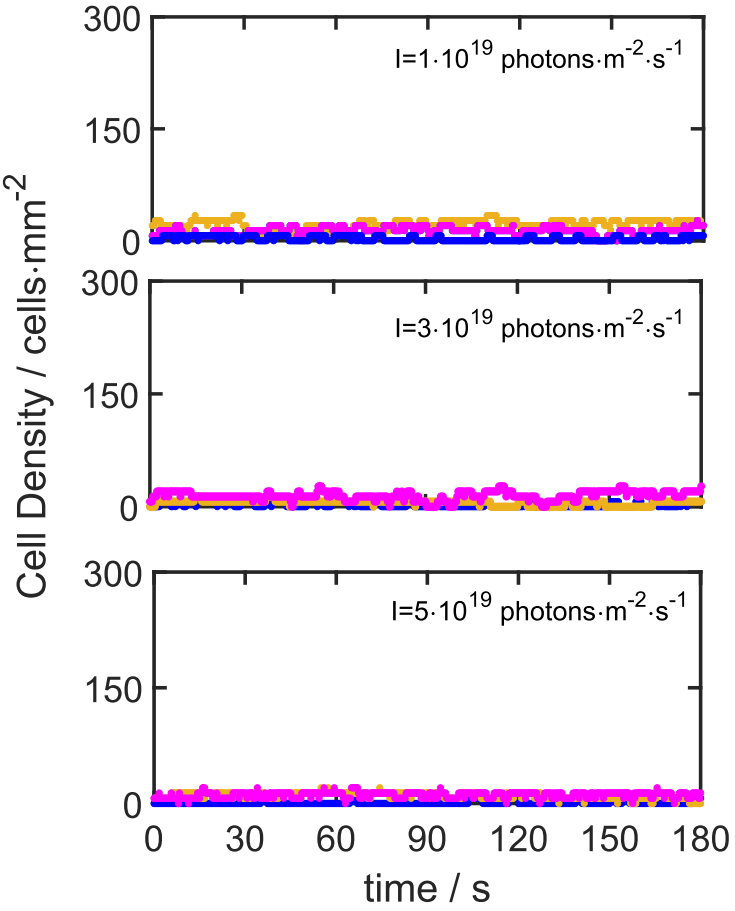


**Figure 6.3:** Adsorption experiments performed using the strain Δa,pCRY. Three light intensities, namely 1, 3, and $5{\cdot}10^{19}$ photons·m$^{-2}$·s$^{-1}$, were probed to assess a shifting of the intensity threshold for the adhesion switch. For each intensity, three adsorption runs are shown. A total of 4 independent experiments were performed. In all of them, the adsorption is completely inhibited.

In order to confirm a significant difference in the flagellar adhesion forces exhibited by the single- and double CRY-deletion mutants, force measurements were performed using these strains.

## 6.3 Force measurements results

Micropipette force measurements were performed with single- and double-CRY deletion mutants following the usual steps of light incubation and series of force-distance measurements per cell, see Sec. 3.2.4. However, the biggest challenge was to catch a Δa,pCRY cell with the nozzle of the micropipette in the right orientation, since cells with both CRYs deleted show no adsorption to surfaces. In order to immobilize a single cell to the tip of the micropipette, a negative pressure is generated at the opening of the nozzle so that a nearby swimming cell was dragged by the flow field towards the opening. Once a cell was successfully grabbed, the strength of the negative pressure was successively decreased and then increased again, which changed

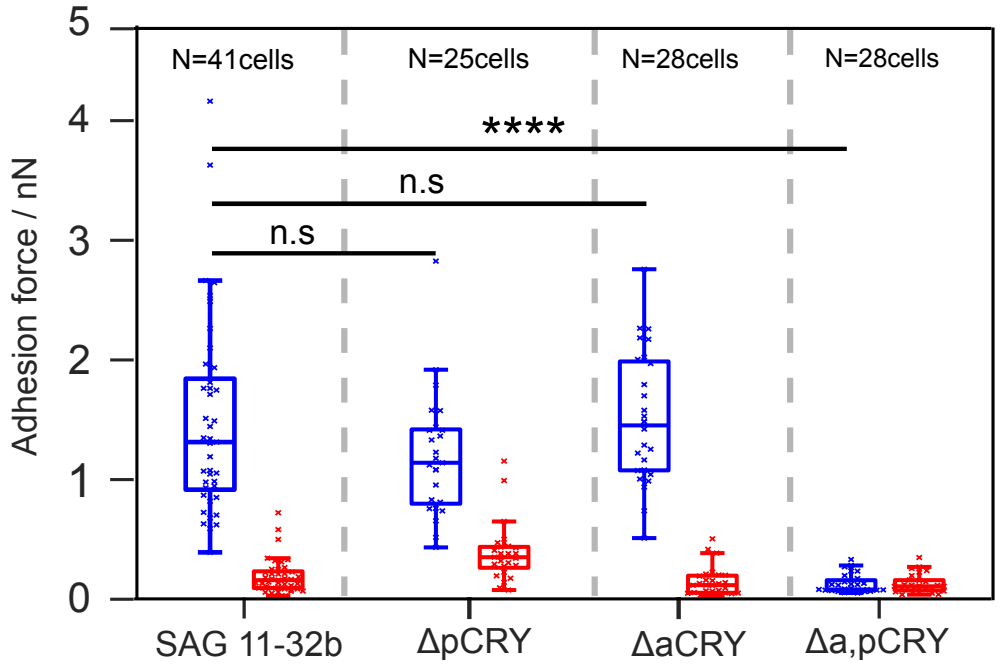


**Figure 6.4:** Distribution of flagellar adhesion forces of the WT strain SAG11-32b and CRY deletion mutants (experiments using ΔpCRY and Δa,pCRY were conducted by Dr. A. Girot). A total of N cells is considered for each strain. For each cell, a set of 10 measurements was performed for each wavelength. A significance test (see Sec. 3.2.5) was performed to identify differences in the distribution of adhesion forces, using the WT strain as a reference. The results show that there are non-significant (n.s) differences in the distribution of adhesion forces of the WT and the single mutant strains ΔpCRY and ΔaCRY under blue light. Remarkably, the significance test yields a very high significant difference between the distribution of forces exhibited by the WT and the double-CRY deletion mutant.

the orientation of the cell. This procedure was repeated until the cell was found to be in the right orientation, namely with the flagella outside of the pipette and the main axis of the cell body parallel to the nozzle. The results are shown in Fig. 6.4.

Force measurement results show non-significant differences in the distribution of adhesion forces of WT and single-CRY deletion mutants under blue light. Under red light, the distribution of adhesion forces of ΔaCRY and ΔpCRY is reduced to effectively zero values. Therefore, both ΔaCRY and ΔpCRY exhibit light-switchable adhesion. Under blue light, the median values of the adhesion forces of ΔpCRY (1.14 nN) and ΔaCRY (1.45 nN) are consistent with the one exhibited by the WT strain (1.31 nN). However, the comparison of the distribution of the adhesion forces between the WT and the double-CRY deletion mutant remarkably illustrates that the deletion of both aCRY and pCRY inhibits the flagellar adhesion of the WT cells in blue light.

Interestingly, the adhesion forces under red light, on average, seem to be significantly higher for the ΔpCRY strain, which exhibits a median force of 0.36 nN, whereas for the WT the median is 0.16 nN, see Fig. 6.5. Therefore, a significance

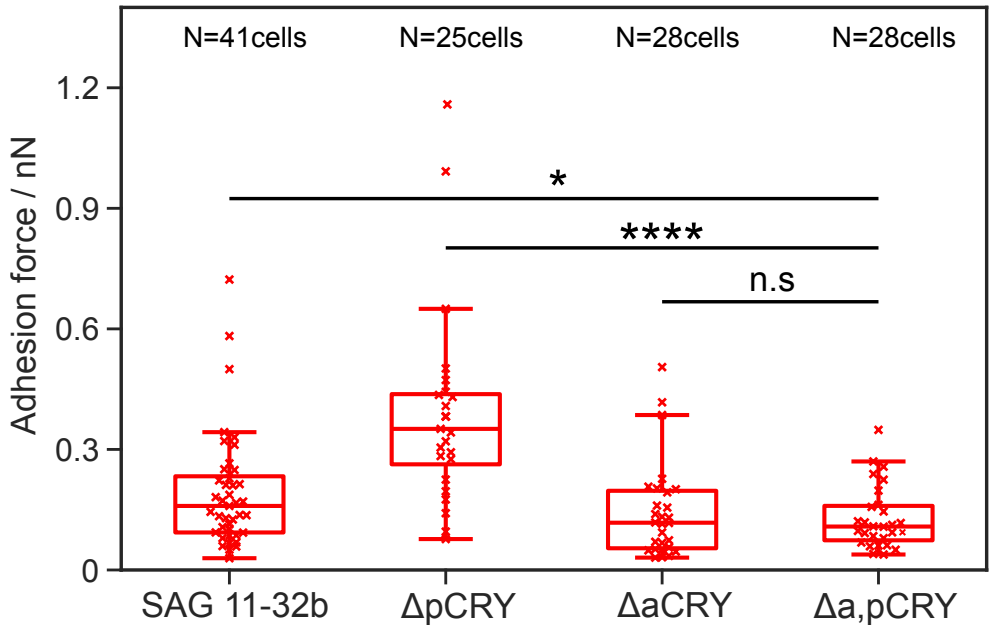


**Figure 6.5:** Distribution of adhesion forces of WT and CRY-deletion mutants under red light ($\lambda = 671/10$ nm). A significance test is obtained using the non-adhesive Δa,pCRY mutant strain as the reference. The distribution of adhesion forces exhibited by ΔpCRY shows highly significant differences with the reference strain. The force distribution associated with the WT shows a small but significant difference with the reference strain. The distribution of forces of ΔaCRY is consistent with the one of the reference strain.

test was applied, considering the non-adhesive Δa,pCRY as the reference strain that does not show adhesion under blue and red light. The results summarized in Fig. 6.5 indicate that the ΔpCRY strain displays significantly higher adhesion forces in red light with respect to the double-CRY mutant. In the case of the ΔaCRY strain, the distribution of adhesion forces is indistinguishable from the one of the reference strain.

This result is interesting since the FAD chromophore of the CRYs is known to develop a sensitivity to yellow and red wavelengths when it is in the neutral radical state ($FADH^{\bullet}$), see Fig. 2.10b. Consequently, I decided to explore the adhesion forces of the WT and single CRY-deletion mutants in yellow and red light. The yellow wavelength selected for these measurements ($\lambda = 584/13$ nm) coincides with the local absorption maximum of $FADH^{\bullet}$ in yellow light [226]. The corresponding red wavelength ($\lambda = 644/10$ nm) used in the experiments is close to the other local maximum of absorption ($\lambda = 633$ nm) in red light. The results of these force measurements are shown in the next section.

## 6.4 Force measurements in yellow and red light

Force experiments to measure adhesion forces in yellow and red light were performed using single CRY-deletion mutants and compared to the WT strain. Cells were

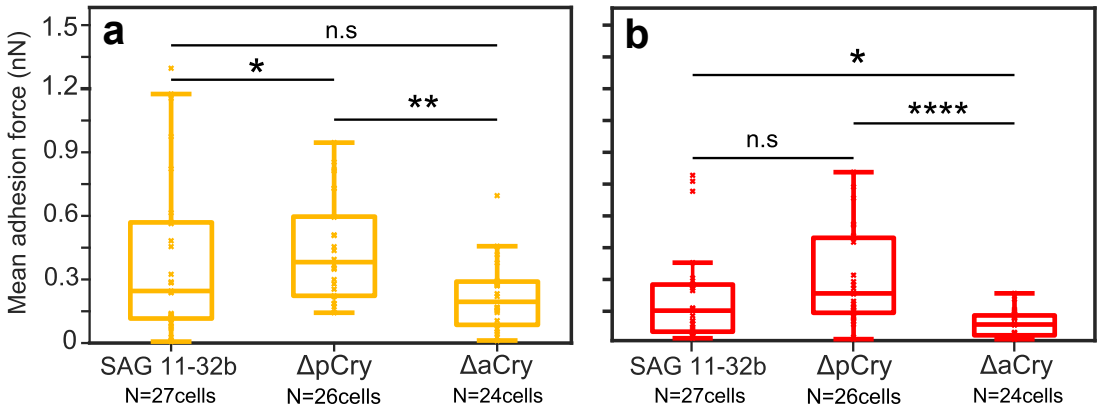


**Figure 6.6:** Distribution of adhesion forces of the WT strain SAG11-32b, ΔaCRY and ΔpCRY under yellow ($\lambda = 584/13$ nm) and red ($\lambda = 644/10$ nm) light. A total of N cells were measured for each strain. Ten force-distance measurements were performed for each cell and each wavelength.

exposed to blue light in order to grab them to the nozzle of the micropipette from their gliding configuration on the solid substrate. An incubation time of 5 minutes under each wavelength was imposed before the measurements. A set of 10 force measurements was collected for each cell under yellow and red light. The mean of those force measurements was used to compare the distribution of forces under the different light conditions. The results are presented in Fig. 6.6.

A comparison of the distribution of adhesion forces using the WT strain as a reference shows that ΔpCRY exhibits significantly higher adhesion to substrates in yellow light compared to the WT, see Fig. 6.6a. In yellow light, the median of the force distributions exhibited by the strains is 0.25 nN (WT), 0.39 nN (ΔpCRY), and 0.19 nN (ΔaCRY). The significance test yields non-significant differences in the distributions of the WT and the ΔaCRY strain. However, a statistical comparison between the mutant strains reveals that there is an even higher difference in their distributions of adhesion forces, where ΔpCRY cells exhibit significantly higher adhesion than ΔaCRY cells.

Under red light, ΔpCRY exhibits non-significant differences in the distribution of adhesion forces relative to the WT, whereas ΔaCRY has a slight, yet significantly lower distribution of forces relative to the WT, see Fig. 6.6b. The median of the forces exhibited by the strains under red light ($\lambda = 644/10$ nm) is: 0.15 nN (WT), 0.23 nN (ΔpCRY), and 0.06 nN (ΔaCRY). The most remarkable difference in the force distributions is seen between the CRY deletion mutants, where ΔpCRY exhibits significantly higher adhesion forces than ΔaCRY.

## 6.5 Preliminary results

### 6.5.1 pCRY degradation and early-morning experiments

According to the literature, pCRY is rapidly degraded in *C. reinhardtii* in the presence of blue and red light, after the start of the cell's subjective day [229]. Assuming this is correct, then the variable amount of pCRY in *C. reinhardtii* could alter the adsorption kinetics as pCRY is degraded. Motivated by these findings, I decided to perform early-morning adsorption experiments to assess whether there are differences in the response of cells to blue light when they are taken directly from their night cycle. Unfortunately, micropipette force measurements could not be performed, since catching a cell by the pipette requires the illumination of the experimental chamber.

For early-morning experiments, I followed the procedure described in Sec. 3.3.5 and performed experiments using vegetative WT strain (SAG11-32b) and ΔpCRY cells. Unfortunately, early-morning experiments are quite challenging to perform. In a total of three independent experiments I tried for each strain, I noticed that many cells were still in their hatch, indicating that they still were at the last phase of vegetative division, see Fig. 2.4. In some experiments, there were also non-motile cells at the surface of the chamber that did not appear to be in the gliding configuration. In order to remove these cells from the field of view, I rotated the chamber by 90° such that non-motile cells could fall by gravity and accumulate at one side of the chamber. However, the cells did not fall, suggesting that they are attached by the cell body to the surfaces of the chamber. As a consequence of this, I render the results of early-morning experiments as preliminary results.

Results for the WT strain are shown in Fig. 6.7, for which I managed to perform 2 independent experiments. The results show that the first run of adsorption does not exhibit the sigmoidal shape, typical of the adsorption of *C. reinhardtii* cells. After switching from darkness to blue light, the first run of adsorption shows a very slow increase in the cell surface density, after which the adsorption rate increases towards the end of the run. After 300 s in blue light, the cells were kept in the dark for 15 minutes before the start of the next run. Interestingly, in both experiments, all the adsorption runs but the first run, consistently show the characteristic sigmoidal shape of the adsorption of *C. reinhardtii*. As this result could be an effect of the degradation of pCRY, I decided to perform experiments with ΔpCRY cells in order to see if the same trend applies for the first run.

For experiments using ΔpCRY cells, I only managed to obtain one reliable result, which is shown in Fig. 6.8. When the ΔpCRY cells were exposed to blue light for the first time, many of them started to adsorb slowly, compared to the subsequent runs. The sigmoidal shape of the first adsorption run allowed to extract the time parameters using the time-delayed Langmuir model, which yielded $\tau_a = 23.8$ s,

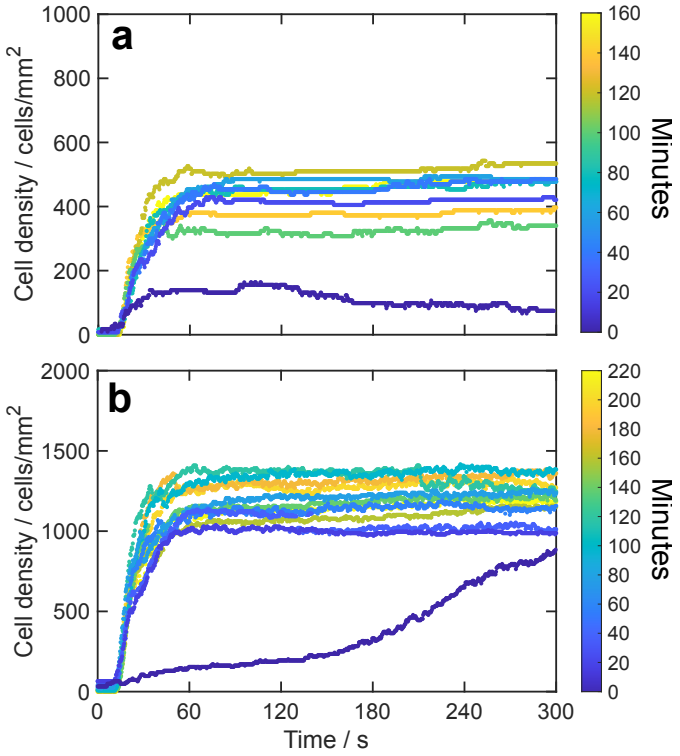


**Figure 6.7:** Adsorption curves obtained during early-morning experiments using the WT strain SAG11-32b. Timepoints represent minutes after the start of the cells' subjective day. Each run was performed under blue light for 300 s at an intensity of $1{\cdot}10^{19}$ photons$\cdot$m$^{-2}\cdot$s$^{-1}$. The cells were kept under zero light intensity for 15 minutes until the start of the next adsorption run. (a) The first run (red curve) shows an increasing number of the cell surface density, which decays after around 90 s. This is an indication that some cells did not stay long in the gliding configuration and the cells desorbed. All the subsequent runs show the typical sigmoidal shape of the adsorption of *C. reinhardtii*. (b) Results of a second independent experiment. The first run (red curve) also shows a slow increase in the cell surface density until it reaches a value that is similar for subsequent plateau densities. In all subsequent runs the cells exhibit the sigmoidal kinetics of adsorption.

$\tau_{\mathrm{b}} = 28.9$ s and $\tau_{\mathrm{delay}} = 54.9$ s. The subsequent runs exhibit similar kinetics as the ones seen for ΔpCRY in the adsorption experiments presented in Sec. 6.2.1.

It could be tempting to associate the very slow increase in the cell surface density, exhibited by the WT cells, to the light degradation of pCRY. Even the single experiment using ΔpCRY shows that the deletion of this photoreceptor does not disrupt the adsorption of cells in the first run. One could even think that pCRY act as a negative regulator of light-switchable adhesion, since its presence in the WT cells might lead to very few of them adsorbing under the first exposure to light. However, it is difficult to draw conclusions from a single experiment, which even conflicts with the experimental protocol that I have followed for all the rest of the experiments presented in this thesis. The problem is that the high values of the plateau density observed in the experiment using ΔpCRY means that the cell density of the culture used for the experiment was high. This conflicts with the established protocol for

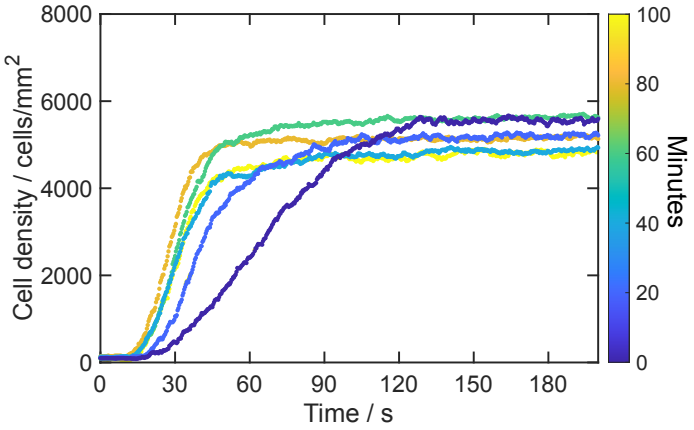


**Figure 6.8:** Early-morning experiment using the strain ΔpCRY. Time points represent minutes after the start of the cells' subjective day. Each run was performed under blue light for 300 s at an intensity of $1{\cdot}10^{19}$ photons·m$^{-2}$·s$^{-1}$. The cells were kept under zero light intensity for 15 minutes until the start of the next adsorption run. The first adsorption run (red curve) is characterized by a slow increase of the cell surface density and exhibits the characteristic sigmoidal shape of *C. reinhardtii* adsorption. Subsequent runs exhibit consistent sigmoidal kinetics of adsorption, which are comparable with the findings in Sec. 6.2.1.

adsorption and force measurements because high densities lead to shadowing effects in the suspension during incubation and also a faster depletion of nutrients in the culture medium. This might lead to cells that are not in logarithmic growth, which could potentially alter the results of the experiments. Nevertheless, the slow kinetics of adsorption seen in WT cells during their first exposure to blue light seems to be consistent and future experiments might be of interest.

Even though the slow adsorption during the first run could be consistent, the evidence of the degradation of pCRY conflicts with the results of this thesis. Actually, if pCRY is degraded during the day, then the strain ΔaCRY should not exhibit light-switchable adhesion, which is in contrast to the data seen in Fig. 6.4. This is because there should be neither pCRY nor aCRY in the afternoon, which should inhibit adhesion. The evidence of pCRY degradation, however, has been reported using another WT strain of *C. reinhardtii*, namely SAG 73.72. Therefore, I decided to test SAG 73.72 in order to assess the relation between CRYs and light-switchable adhesion.

### 6.5.2 Light-switchable adhesion of SAG 73.72

Most of the experimental results on the biological role of CRY photoreceptors in *C. reinhardtii* have been obtained using another WT strain labeled SAG 73.72 [228, 235]. For consistency check, adsorption experiments and force measurements using SAG 73.72 were performed in order to assess whether aCRY and pCRY are involved in the light-switchable adhesion in such strain.

First, the intensity threshold of light-switchable adhesion of SAG 73.72 cells was

obtained by means of single-cell micropipette force measurements[3]. Force measurements were performed at different light intensities under blue light ($\lambda = 476/10$ nm). The results shown in Fig. 6.9 illustrate a higher intensity threshold to trigger flagellar adhesion of SAG 73.72 compared to the one reported for our strain SAG11-32b [40]. Figure 6.9a shows that the adhesion forces exhibit a high variability between the cells measured. Most of the cells exhibit forces ranging between 7 nN and can go as high as 23 nN. The mean adhesion force measured in SAG 73.72 is noticeably higher than those exhibited by the WT strain SAG11-32b, which usually range between 1-2 nN, see Fig. 6.4. Figure 6.9b indicates that the minimum light intensity that results in flagellar adhesion of SAG73.72 is around $1{\cdot}10^{19}$ photons$\cdot$m$^{-2}\cdot$s$^{-1}$. The magnitude of the flagellar adhesion reaches a plateau at $3{\cdot}10^{19}$ photons$\cdot$m$^{-2}\cdot$s$^{-1}$.

Based on this light intensity threshold, I performed adsorption experiments using SAG 73.72, as well as CRY mutants that were generated from this strain. The mutants used for adsorption experiments were ΔaCRY, ΔpCRY, and the double mutant Δa,pCRY. Adsorption experiments were performed at an intensity of $3{\cdot}10^{19}$ photons$\cdot$m$^{-2}\cdot$s$^{-1}$, under which the cells exhibit light-switchable adhesion. The results of the adsorption experiments for the WT and the mutants are illustrated in Figure 6.10.

Adsorption experiments using SAG 73.72 yielded interesting experiments that highlight a phenotypical difference relative to the WT strain SAG11-32b. Figure 6.10a shows that SAG73.72 exhibits light-switchable adsorption under blue light. After switching to blue light, it takes around 15-16 s for the first cells of the suspension to attach to the surface of the chamber. However, SAG 73.72 seems to present very high cell-cell variability, as continuous adsorption is seen at times much longer

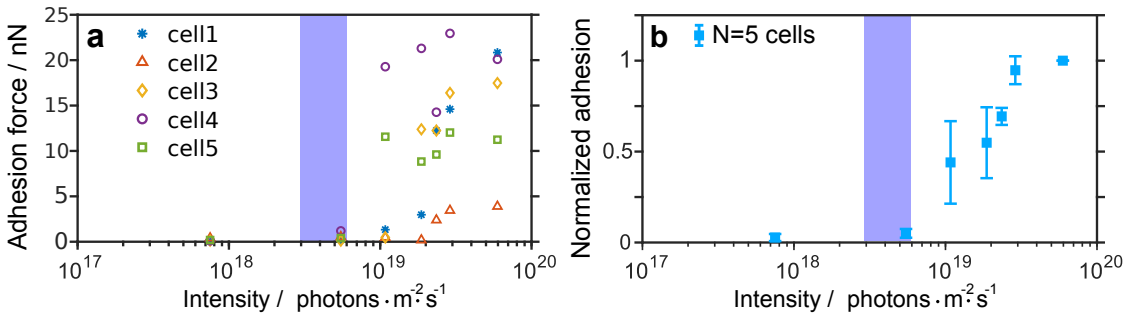


**Figure 6.9:** Characterization of the intensity threshold of light-switchable adhesion of SAG 73.72 in blue light ($\lambda = 476/11$ nm). For each cell, 5 force-distance measurements were performed and the order of the intensities was randomly chosen. The blue regions indicate the intensity threshold of SAG11-32b. (a) Mean flagellar adhesion forces exhibited by a total of 5 different cells. (b) Normalized mean flagellar adhesion forces exhibited by the cells in (a). The minimum light intensity that results in flagellar adhesion is around $1{\cdot}10^{19}$ photons$\cdot$m$^{-2}\cdot$s$^{-1}$. Adhesion forces over $3{\cdot}10^{19}$ photons$\cdot$m$^{-2}\cdot$s$^{-1}$ do not seem to vary significantly.

[3]These measurements were performed by Dr. Antoine Girot.

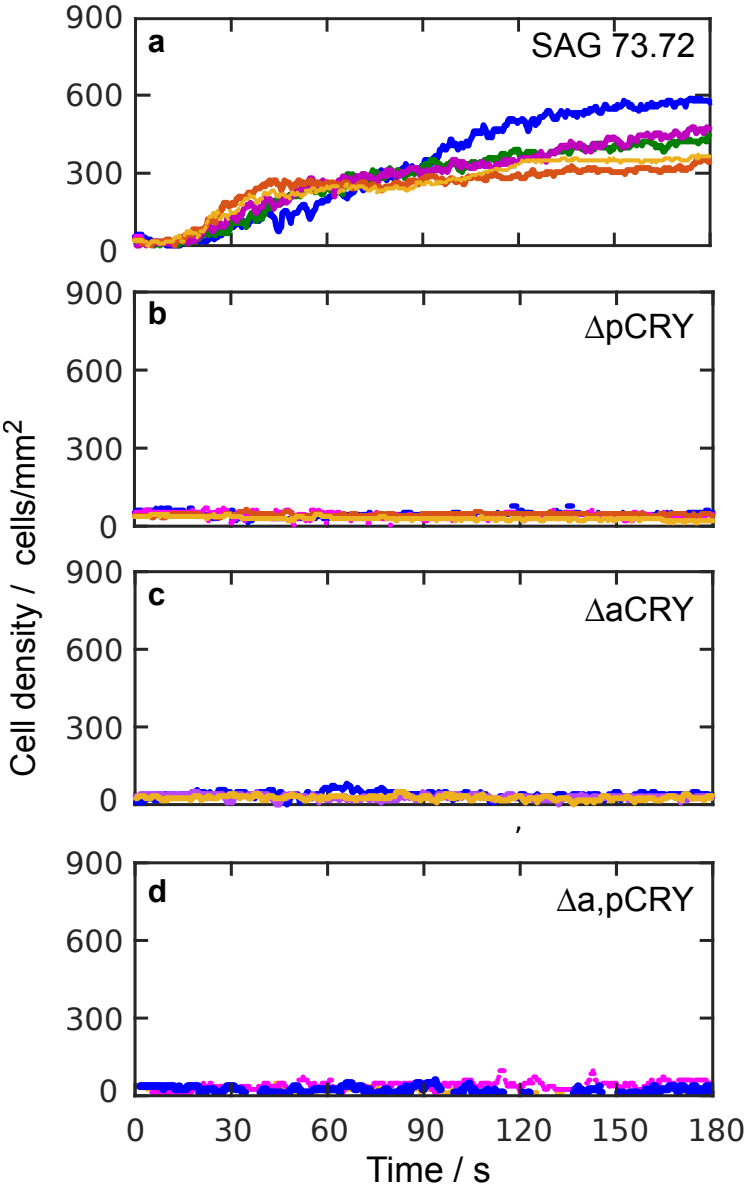


**Figure 6.10:** Adsorption experiments using the WT strain SAG 73.72 and CRY mutants generated from it. Adsorption runs were recorded under blue light at an intensity of $3{\cdot}10^{19}$ photons$\cdot$m$^{-2}\cdot$s$^{-1}a$. (a) Adsorption runs obtained using the strain SAG 73.72. Further desorption runs were obtained using (b) ΔpCRY, (c) ΔaCRY, and (d) the double mutant Δa,pCRY. It is seen that the deletion of only one CRY photoreceptor is sufficient to disrupt light-switchable adhesion in the strain SAG 73.72.

than 60 s, which is the typical timescale for plateau attainment in SAG11-32b. This was commonly seen in SAG 73.72 for which it was not possible to do a proper analysis of the kinetics so far.

Figures 6.10b and Figure 6.10c remarkably show that the deletion of either pCRY or aCRY is sufficient to inhibit the adhesion of SAG 73.72 cells to the surface. This result presents a noticeable difference in the light-switchable adhesion phenotype with respect to the WT strain SAG11-32b. This illustrates another piece of evidence (in addition to the results shown in Sec. 6.2) that CRYs are involved in the light-

switchable adhesion phenotype. Finally, the expected null adsorption observed for the double mutant Δa,pCRY is presented in Fig. 6.10d for completion.

## 6.6 Discussion

In this chapter, the role of the cryptochrome photoreceptors aCRY and pCRY in the light-switchable adhesion phenotype of *C. reinhardtii* has been elucidated. The first indication came from the action spectrum of light-switchable adhesion, obtained using the WT strain SAG11-32b by means of adsorption experiments and micropipette force measurements, see Fig. 6.1. The action spectra obtained by adsorption measurements show a peak in the adsorption rate $\tau_{\mathrm{a}}^{-1}$ of cells to surfaces at 450 nm, see Fig. 6.1a. For wavelengths above and below this value, there is an abrupt decrease in the values of $\tau_{\mathrm{a}}^{-1}$. Although different wavelengths and intensities trigger different phototactic responses in *C. reinhardtii*, it has been shown in Sec. 5.1.1 that phototaxis does not affect the values of $\tau_{\mathrm{a}}$ significantly. Therefore, one could still trust the results given by $\tau_{\mathrm{a}}^{-1}$, since it is not biased by the phototactic behavior of the cells exposed to different wavelength conditions.

Regarding the results of $\tau_{\mathrm{delay}}$ for the desorption under different wavelengths, it is interesting that it shows similar features as the values of $\tau_{\mathrm{a}}^{-1}$ since they are not related to each other. A possible explanation is that the cells exposed to wavelengths triggering faster adsorption rates spend more time attached to the surface during an adsorption run. This, in turn, could generate more adhesive contact points between the cell's flagella and the surface, which then result in a longer time for the cells to overcome the flagellar adhesion to surfaces, after they are exposed to red light. Even though $\tau_{\mathrm{a}}^{-1}$ and $\tau_{\mathrm{delay}}$ exhibit similar features over the measured wavelengths, the action spectrum of $\tau_{\mathrm{delay}}$ is red-shifted with respect to the maximum of the action spectrum of $\tau_{\mathrm{a}}^{-1}$. The detachment of the surfaces is a more intricate process, involving compartmentalized calcium elevations within the flagella, which can be caused by mechanical stresses along the flagella [134], which could cause a shift in the peak of $\tau_{\mathrm{delay}}$. Unfortunately, a measurement involving calcium elevation is not possible since blue fluorescence is necessary for visualization [135].

The action spectrum obtained by means of micropipette force spectroscopy illustrates that light-switchable adhesion can be triggered, not only when the cells are exposed to blue light in the range 420-480 nm, but also in UV, especially in the band 350-380 nm. For cells exposed to wavelengths above 500 nm, the flagellar adhesion is significantly reduced down to near-zero values. In addition to this, the action spectrum shows a high similarity to the absorption spectra reported for aCRY and pCRY photoreceptors [220, 226, 236]. More specifically, the shape of the action spectrum agrees well with the oxidized state of the FAD chromophore that is known to bind CRYs [225]. This result motivated adsorption and micropipette force

measurements using CRY-deletion mutants in two WT strains, namely SAG11-32b and SAG 73.72.

The results obtained from adsorption and force measurements using CRY deletion mutants suggest a link between CRYs and light-switchable adhesion in both WT strains. However, it was shown that the deletion of only one CRY was sufficient to disrupt the adhesion of SAG 73.72 cells to surfaces, whereas it required the deletion of both aCRY and pCRY to completely disrupt the adhesion in SAG11-32b. This is clearly a manifestation of a difference in the light-switchable adhesion phenotype between both strains.

Another noticeable difference between the WT strains is the higher threshold intensity for the activation of flagellar adhesion of SAG 73.72 compared to SAG11-32b, as shown in Fig. 6.9. Furthermore, the distribution of adhesion forces for SAG11-32b, seen in Fig. 6.4, shows that the values of adhesion can be as low as 0.24 nN and as high as 2.66 nN. Regarding the strain SAG 73.72 the forces measured to obtain the intensity threshold can be as low as 7 nN and as high as 23 nN. From the results presented in this chapter, it could be tempting to conclude that CRYs are involved in controlling light-switchable adhesion of *C. reinhardtii* to surfaces. However, there are several aspects that need to be clarified.

First, CRYs have been localized in the nucleus of vegetative *C. reinhardtii* cells [234, 235] but never in their flagella. In the nucleus, CRYs are reported to function as transcription factors rather than as photoreceptors and are known to regulate components of the circadian rhythm of *C. reinhardtii* [236, 290]. The rate at which transcription occurs in eukaryotes is of the order of a few minutes to several tens of minutes [291]. This is completely incompatible with the time scales of light-switchable adhesion, which usually occurs within 16-20 s, as shown by the values of $\tau_{\text{delay}}$ obtained from adsorption experiments in this thesis. Furthermore, using single-cell micropipette measurements, the manifestation of flagellar adhesiveness has been reported even at around 10 s or less for *C. reinhardtii* cells exposed to white light at high intensities [40]. Therefore, the incompatibility of time scales could mean that aCRY and pCRY are somehow involved in light-switchable adhesion, but do not mediate directly the phenotype.

Second, the hypothesis of light-degradation of pCRY [228, 229] seems incompatible with the obtained results of this thesis. The degradation of pCRY should imply that this photoreceptor is not present in the cell during the day phase, when adsorption and force-measurement experiments are conducted. If pCRY is not present, a deletion of aCRY should be then sufficient to disrupt the adhesion of *C. reinhardtii* cells of the strain SAG11-32b. This is not what is seen in this thesis. For some reason, both genes encoding aCRY and pCRy must be deleted to disrupt the adhesion phenotype, see Fig. 6.4. Even in the case of the WT strain SAG 73.72, the degradation of pCRY should render the cells non-adhesive, as in this strain only one

photoreceptor needs to be removed to disrupt the adhesion. This is not seen either, according to the results shown in Sec. 6.5.2.

Third, force measurements under yellow and red light show that the deletion of pCRY yielded significantly higher adhesion forces of cells exposed to 584 nm and 644 nm, see Fig. 6.6. One could speculate that the dominant photoreceptor of light-switchable adhesion is aCRY, which is indeed in line with the fact that aCRY is the only CRY reported to absorb light in that range, according to *in vitro* measurements [226]. However, according to crystallography studies on aCRY made *in vitro*, it has been shown that aCRY can also boost its sensitivity to blue light by the binding of a second chromophore name 8-HDF [220], see Sec. 2.4.2. If this is the case *in vivo*, then one might expect a huge peak of sensitivity and thus, adhesion forces, around 454 nm. As mentioned above, this is not what I see in the results, as the shape of the action spectrum resembles the one of $FAD_{ox}$. Taken all of this together, the evidence from the literature is not exactly in line with our findings. However, I might propose a way to resolve this conundrum.

The major issue with CRYs being direct mediators of light-switchable adhesion is that they are not located in the flagella of *C. reinhardtii*, but only in the nucleus [235]. It is hard to conclude that a photoreceptor in the nucleus regulates the dynamics of flagellar adhesion in a time scale of 15 s. However, what one really can conclude from the experiments shown in this thesis is that CRYs are a required part of the signaling system underlying light-induced flagellar adhesion in *C. reinhardtii*. In fact, it might be possible that aCRY, for instance, is not at all functioning as a photoreceptor, as it is the case in humans, where it is part of the circadian clock but not a light-sensitive protein [292]. In case it works as a clock component and not as a photoreceptor, CRYs would not need an additional light-harvesting pigment, such as 8-HDF. This is compatible with the action spectrum of the flagellar adhesion obtained in this thesis.

Having all these considerations in mind, I propose that there should exist another so-far-undiscovered photoreceptor that directly mediates light-switchable adhesion of *C. reinhardtii* to surfaces. The expression of this photoreceptor could potentially be regulated by CRY molecules in a circadian-dependent manner. In order to be compatible with the features of the action spectrum and the time scales associated with flagellar adhesion, the photoreceptor must be localized in the cells' flagella and its functionality should be given by a flavin chromophore. Potential candidates involve AGG2 and AGG3, since these are flavoproteins that are localized in the flagella and are known to mediate the orientation of the cells to light [293].

## 6.7 Summary

In this chapter, I presented the results of adsorption and micropipette force measurements using CRY-deletion mutants. Several results have been obtained and strongly contribute to elucidating the main goal of this thesis on identifying the photoreceptor mediating light-switchable adhesion in *C. reinhardtii*. The main results are the following:

- The action spectrum obtained from absorption experiments shows that the adsorption rate, $\tau_a^{-1}$, reaches a maximum at 454 nm when the WT cells are exposed to wavelengths. The values of the adsorption rate rapidly decrease for wavelengths larger than 500 nm, and cells do not show adsorption.

- The action spectrum for $\tau_{delay}$ during desorption has a peak at 480 nm. For wavelengths larger than 480 nm, $\tau_{delay}$ rapidly decays to zero. and presents similar features as the one for $\tau_a^{-1}$.

- The action spectrum of $\tau_a^{-1}$ and $\tau_{delay}$ exhibit similar features. However, the peak of $\tau_{delay}$ is red-shifted around 30 nm relative to the maximum of $\tau_a^{-1}$ at 454 nm.

- The action spectrum of the flagellar adhesion of the WT strain SAG11-32b shows that the highest adhesion forces are observed when the cells are exposed to blue (around 454 nm) or UV light (around 365 nm). Furthermore, the action spectrum resembles the absorption spectrum for flavin adenine dinucleotide (FAD), the chromophore that binds to cryptochromes.

- Adsorption experiments using ΔaCRY and ΔpCRY show that the time parameters for these strains agree well with the ones of the WT. Thus, aCRY and pCRY, individually, do not play a significant role in the kinetics of adsorption and desorption of *C. reinhardtii* to surfaces.

- A deletion of both aCRY and pCRY completely inhibits the adsorption of *C. reinhardtii* to surfaces in the WT strain SAG11-32b, whereas only the deletion of one of the CRYs disrupts the adhesiveness of SAG 73.72 cells.

- Micropipette force measurements show that flagellar adhesion forces in the strain Δa,pCRY are reduced to zero under blue and red light, and thus the tandem of both aCRY and pCRY controls in the flagellar adhesion of *C. reinhardtii* to surfaces.

- Several of the findings presented in this thesis challenge earlier results reported in the literature. The most critical aspect is the localization of CRYs in the nucleus, and not in the flagella of *C. reinhardtii*. In the nucleus CRYs function

as gene transcription factors. This suggests that CRYs do not mediate light-switchable adhesion directly, since the timescales governing the onset of the light stimulus and the onset of the adhesion response (around 15 s) are not compatible with transcription (of the order of several minutes).

- In order to reconcile the results presented in this thesis and the reported studies, I propose that the light-switchable adhesion phenotype of *C. reinhardtii* is directly mediated by a so-far-overlooked flavin-based photoreceptor that is localized in the flagella of the cells.

# Chapter 7

# Conclusion and Outlook

## 7.1 Conclusion

In this thesis, I studied the light-switchable flagellar adhesion of the green unicellular microalga *Chlamydomonas reinhardtii*. The main goal of this thesis was to identify the blue-light photoreceptor mediating the adhesion phenotype, and also to characterize the role of the different photoreceptors in the light-regulated flagellar adhesiveness of *Chlamydomonas*. I investigated the effects of different light conditions on the kinetics of adsorption and desorption of wild-type (WT) and genetically-modified photoreceptor deletion mutants. Additionally, I also provided a quantification of the flagellar adhesion forces by means of micropipette force spectroscopy.

In Chapter 4, adsorption experiments were established as a way to quantify the time scales underlying the light-regulated adsorption and desorption of *C. reinhardtii*. The quantification of the time scales was obtained using a Langmuir-type model, which was modified to consider the natural time lag between stimulus, i.e. the change of light conditions from red to blue and *vice versa*, and the flagellar adhesion response of the cells. A key element in the model was the introduction of a time-dependent function that generates a time delay in the kinetics of adsorption and desorption described by the classical Langmuir model. The modified model reveals that the adsorption rate of cells to surfaces does not depend on the light intensity, whereas the onset of the flagellar adhesiveness response after a light stimulus decreases monotonically with the light intensity. For a fixed light intensity, the adhesion response exhibited by the wild-type strain illustrates that the time scale associated with the switch-off of the flagellar adhesiveness is around an order of magnitude larger than for the switch-on. The model also reveals that the rate at which cells leave the surface from their gliding configuration is about 3 times the rate at which the cells transition from the planktonic to the gliding state. Regarding phototactic effects, I showed that phototaxis does not have a significant impact on the adsorption rate of *C. reinhardtii*. However, non-phototactic blind cells do exhibit longer flagellar adhesion response times after the onset of the blue light

stimulus. Finally, it was shown that the ratio of the number of cells adsorbed at the top and bottom surfaces of the experimental chamber (i.e. the plateau density ratio) is governed by the strain's phototactic response. This last result illustrates that adsorption experiments can be used to quantify the interplay between phototaxis and gravitaxis. More generally, this approach can be of interest to characterize the kinetics of surface colonization of photoactive microorganisms under controlled light conditions. The application of the technique could provide a broader intuition of the role of light in the dynamics of the first steps of biofilm formation for such organisms.

Chapter 5 is divided into three main parts. The first part deals with the role of channelrhodopsins (ChR) regarding the onset of the flagellar adhesiveness. By means of adsorption experiments, it was found that only the simultaneous deletion of both ChR1 and ChR2 yields a phototactically-impaired strain, as shown by the ratio of the plateau densities exhibited by the ChR-deletion mutants. This is in line with earlier reports [42]. Furthermore, it was found that the loss of neither ChR1 nor ChR2 significantly affects the kinetics of adsorption. Adsorption experiments also show that a deletion of any of the ChRs results in slightly longer times in the onset of the adhesiveness response compared to the WT. This might suggest that calcium signaling is involved in light-switchable adhesion, but in a non-critical way, as the blind strain that does not contain ChR1 and ChR2 still exhibits the adhesion response in blue light. The signaling pathway, for which ChRs are an essential component, could influence the transport of adhesive glycoproteins along the cells' flagella and thus change the light-switchable response [134, 179].

The second part of Chapter 5 deals with the role of phototropin (PHOT) in the kinetics of adsorption and desorption. The most remarkable result is that the deletion of PHOT significantly extends the time for the switch-off of flagellar adhesiveness. On average, it takes almost 5 minutes for half of the population of PHOT-deletion mutants to detach from the surface, compared to the approximately 2 minutes exhibited by the WT cells. The fact that PHOT is in the flagella of *C. reinhardtii* [259] and that it regulates the abundance of ChR1 [262], might suggest an interplay between these two photoreceptors in the detachment of flagellar glycoproteins from IFT trains during desorption.

In the last part of Chapter 5, micropipette force measurements illustrated that the strains ΔChR1, ΔChR2, and ΔPHOT exhibit light-switchable adhesion. The distribution of forces exhibited by all studied strains in this chapter have a median in the order of 1-2 nN. From the results obtained in this chapter, it is concluded that ChR1, ChR2 and PHOT do not control flagellar adhesion in *C. reinhardtii*, though they might only play a role in the motility of the cells.

Chapter 6 deals with experiments performed using cryptochrome (CRY) deletion mutants: namely animal (aCRY) and plant cryptochromes (pCRY). The use

of these mutant strains was motivated by the action spectra obtained from adsorption experiments and micropipette force measurements. It was found that WT cells adsorb more rapidly when they are exposed to a wavelength of 450 nm. Additionally, the switch-off of the flagellar adhesiveness in red light also is enhanced in this regime. Most notably, the action spectrum of flagellar adhesion agrees well with the absorption spectrum of a flavin chromophore, which is known to bind CRY photoreceptors. Strains with single-disruptions of aCRY or pCRY were studied by means of adsorption experiments, which did not yield differences of interest in the kinetics relative to the WT. The most interesting result came with the deletion of both aCRY and pCRY, which completely impaired the adhesion in the WT strain SAG11-32b in blue and red light. Interestingly, the adhesion in another widely-used WT strain, termed SAG 73.72, was also impaired. However, the deletion of only one of the CRYs was sufficient to inhibit the adhesion. This illustrates an interesting difference in the phenotype of light-switchable adhesion between both WT strains. Despite of the obtained results with CRY-deletion mutants, several considerations suggest that they do not mediate light-switchable adhesion; at least not in a direct way. Several reasons support this hypothesis, but the most crucial one is the fact that CRYs are known to be transcription factors in the nucleus of *C. reinhardtii* [290]. Additionally, they have not been found to be localized in the cells' flagella. This suggests an incompatibility of time scales between transcription (of the order of several minutes) and the switching of the flagellar adhesion under blue light (of the order of 15 s). Taking this into account, I propose that CRYs function as light-sensitive transcription regulators of another photoreceptor that directly mediates the light-induced adhesion phenotype in *Chlamydomonas*. In order to reconcile the characteristic time scales of light-switchable adhesion with the features of the action spectrum of flagellar adhesion, the undiscovered photoreceptor should be localized in the flagella of *C. reinhardtii*, and it likely binds to a flavin chromophore.

## 7.2 Outlook

Identifying the photoreceptor that directly mediates the unspecific light-switchable adhesion of *C. reinhardtii* to surfaces is just the tip of the iceberg. There are multiple aspects that need to be considered to establish a more complete picture of the underlying molecular mechanisms of the adhesion phenotype. The description of complex phenomena, such as light-switchable adhesion or the interaction of microorganisms with surfaces at the molecular level requires the cooperation of different scientific disciplines.

For instance, the application of proteomics to compare the protein composition of the flagella of CRY-deleted mutants could give insights on which proteins are downregulated in the mutant Δa,pCRY relative to the WT strain SAG11-32b.

This information could reveal a list of potential photoreceptors that could meet the constraints of composition, localization, and timescales that are compatible with light-switchable adhesion. Subsequently, in order to confirm whether the photoreceptor mediates flagellar adhesion, further adsorption assays and micropipette force measurements should be conducted using targeted strains for which the gene encoding the candidate photoreceptor is removed from the WT genome, e.g. using again modern gene editing tools such as CRISPR-Cas9.

In order to unravel the interplay between the cryptochromes and the photoreceptor responsible for light-switchable adhesion, it could be of interest to obtain gene expression profiles that could relate what role aCRY and pCRY play in the regulation of the photoreceptor to be found. Why does not the deletion of a single CRY in SAG11-32b disrupt the flagellar adhesion, whereas in the strain SAG 73.72 does? Perhaps, this approach might also help to clarify whether there is light-induced degradation of pCRY or not in the WT strain SAG11-32b.

Another interesting aspect to be considered is the dynamics of the flagellar membrane under different light conditions. The flagella of *C. reinhardtii* are surrounded by a fuzzy sheath of glycoproteins, known as glycocalyx. Electron microscopy techniques such as transmission electron microscopy or cryo-electron microscopy could help to visualize, with sub-nanometric resolution, structural changes of the glycocalyx that might occur when the cells are exposed to blue and red light. In fact, light-switchable adhesion is thought to be the result of an active protein relocalization in the flagellar membrane [40]. Therefore, a visualization of the ultrastructural changes in the cells' flagella could help to elucidate how the flagellar adhesiveness is switched on and off by light.

Light has a relevant impact on the adhesion of microalgae to surfaces. Yet, there are still very few studies that highlight its importance at the fundamental level. In this context, an attractive application of the adsorption experiments could be to determine the extent of light-switchable adhesion in the evolutionary tree of life. For this, adsorption experiments on close and distant relatives of *C. reinhardtii* could be performed. In that way, one could have an idea of how diversified the phenotype is across different species. For instance, preliminary experiments to assess light-switchable adhesion have been performed using *Chlamydomonas noctigama*, a closely related strain to *C. reinhardtii*; and the distant relative *Oogamochlamys gigantea* [278]. Both strains exhibit light-switchable adhesion, however, such experiments have been performed under white light only, which does not provide information on the wavelength triggering the adhesion. Moreover, adsorption experiments could be also extended to flagellated multicellular photoactive organisms in order to assess whether light-switchable adhesion is a generic trait of flagellated microalgae. In that case, further studies could be performed in order to assess the evolutionary advantage of such a highly conserved phenotype.

As for technological settings, the elucidation of the mechanisms underlying light-switchable adhesion could provide interesting applications focused on optimizing the efficiency of photobioreactors or biofilm-mediated wastewater treatment systems. Moreover, an understanding of the molecular mechanism underlying the interaction of microalgae to surfaces could help to design functional light-activated surfaces that could promote or diminish the adhesion of microorganisms to surfaces. Finally, the importance of understanding the chain of events that links the activation of a light-sensitive molecule with the emergence of a specific phenotype may inspire the development of techniques as revolutionary as optogenetics, in which light could be employed to activate photoreceptors that enhance the efficiency of drug delivery within organisms.

# Appendix A

# Supplementary information: Bandpass filter used in this thesis

## A.1 List of bandpass filters used in this thesis

| Wavelength (nm) | FWHM (nm) | Transmission coefficient | Use in experiment |
|---|---|---|---|
| 365 | 10 | 85 | MFS |
| 398 | 11 | 25 | MFS; A |
| 413 | 11 | 32 | MFS; A |
| 424 | 9 | 31 | A |
| 434 | 9 | 28 | MFS |
| 454 | 9 | 39 | MFS |
| 470 | 9.7 | 60 | MFS |
| 476 | 11 | 39 | MFS, ADS |
| 489 | 14 | 43 | MFS, ADS |
| 500 | 12 | 34 | A |
| 508 | 13 | 33 | MFS |
| 515 | 10 | 85 | ADS |
| 524 | 11 | 45 | MFS, ADS |
| 543 | 11 | 46 | MFS, ADS |
| 557 | 12 | 46 | MFS, ADS |
| 584 | 13 | 40 | MFS |
| 644 | 10 | 41 | MFS |
| 670 | 10 | 55 | MFS |

**Table A.1:** List of the bandpass interference filters used in micropipette force measurements (MFS) and in adsorption experiments (A).

# Bibliography


1. Rothschild, L. J. & Mancinelli, R. L. Life in extreme environments. *Nature* **409,** 1092–1101 (2001).
2. Antoine, D., André, J.-M. & Morel, A. Oceanic primary production: 2. Estimation at global scale from satellite (coastal zone color scanner) chlorophyll. *Global Biogeochemical Cycles* **10,** 57–69 (1996).
3. Field, C. B., Behrenfeld, M. J., Randerson, J. T. & Falkowski, P. Primary production of the biosphere: integrating terrestrial and oceanic components. *Science* **281,** 237–240 (1998).
4. Hopes, A. & Mock, T. Evolution of microalgae and their adaptations in different marine ecosystems. *Encyclopedia of Life Sciences,* 1–9 (2015).
5. Wijffels, R. H. & Barbosa, M. J. An outlook on microalgal biofuels. *Science* **329,** 796–799 (2010).
6. Zhong, D. *et al.* Orally deliverable strategy based on microalgal biomass for intestinal disease treatment. *Science Advances* **7,** eabi9265 (2021).
7. Spinola, M. V. & Díaz-Santos, E. Microalgae nutraceuticals: the role of lutein in human health. *Microalgae Biotechnology for Food, Health and High Value Products,* 243–263 (2020).
8. Paerl, H. W., Otten, T. G. & Kudela, R. Mitigating the expansion of harmful algal blooms across the freshwater-to-marine continuum. *Environmental Science & Technology* **52,** 5519–5529 (2018).
9. Boyd, P. W. *et al.* A mesoscale phytoplankton bloom in the polar Southern Ocean stimulated by iron fertilization. *Nature* **407,** 695–702 (2000).
10. Capuzzo, E., Stephens, D., Silva, T., Barry, J. & Forster, R. M. Decrease in water clarity of the southern and central North Sea during the 20th century. *Global Change Biology* **21,** 2206–2214 (2015).
11. Sun, R., Sun, P., Zhang, J., Esquivel-Elizondo, S. & Wu, Y. Microorganisms-based methods for harmful algal blooms control: a review. *Bioresource Technology* **248,** 12–20 (2018).

12. Nasri, H., El Herry, S. & Bouaıcha, N. First reported case of turtle deaths during a toxic Microcystis spp. bloom in Lake Oubeira, Algeria. *Ecotoxicology and Environmental Safety* **71,** 535–544 (2008).

13. NASA Goddard Space Flight Center. Image by Norman Kuring (last access: 15.06.2023). *Patagonian Bloom* `https://www.nasa.gov/multimedia/imagegallery/image_feature_1838.html`.

14. Hou, D. *et al.* Metal contamination and bioremediation of agricultural soils for food safety and sustainability. *Nature Reviews Earth & Environment* **1,** 366–381 (2020).

15. Mishra, S. *et al.* Biofilm-mediated bioremediation is a powerful tool for the removal of environmental pollutants. *Chemosphere* **294,** 133609 (2022).

16. McGenity, T. J., Folwell, B. D., McKew, B. A. & Sanni, G. O. Marine crude-oil biodegradation: a central role for interspecies interactions. *Aquatic Biosystems* **8,** 1–19 (2012).

17. Pacheco, D., Rocha, A. C., Pereira, L. & Verdelhos, T. Microalgae water bioremediation: trends and hot topics. *Applied Sciences* **10,** 1886 (2020).

18. Abinandan, S., Subashchandrabose, S. R., Venkateswarlu, K. & Megharaj, M. Soil microalgae and cyanobacteria: the biotechnological potential in the maintenance of soil fertility and health. *Critical Reviews in Biotechnology* **39,** 981–998 (2019).

19. Al-Abri, M. *et al.* Chlorination disadvantages and alternative routes for biofouling control in reverse osmosis desalination. *NPJ Clean Water* **2,** 2 (2019).

20. Hall-Stoodley, L., Costerton, J. W. & Stoodley, P. Bacterial biofilms: from the natural environment to infectious diseases. *Nature Reviews Microbiology* **2,** 95–108 (2004).

21. Flemming, H.-C. *et al.* Biofilms: an emergent form of bacterial life. *Nature Reviews Microbiology* **14,** 563–575 (2016).

22. Dufrêne, Y. F. & Persat, A. Mechanomicrobiology: how bacteria sense and respond to forces. *Nature Reviews Microbiology* **18,** 227–240 (2020).

23. Loskill, P. *et al.* Influence of the subsurface composition of a material on the adhesion of staphylococci. *Langmuir* **28,** 7242–7248 (2012).

24. Rzhepishevska, O. *et al.* The surface charge of anti-bacterial coatings alters motility and biofilm architecture. *Biomaterials Science* **1,** 589–602 (2013).

25. Epstein, A., Hochbaum, A., Kim, P. & Aizenberg, J. Control of bacterial biofilm growth on surfaces by nanostructural mechanics and geometry. *Nanotechnology* **22,** 494007 (2011).

26. Sauer, K., Camper, A. K., Ehrlich, G. D., Costerton, J. W. & Davies, D. G. Pseudomonas aeruginosa displays multiple phenotypes during development as a biofilm. *Journal of Bacteriology* **184,** 1140–1154 (2002).

27. Sauer, K. *et al.* The biofilm life cycle: expanding the conceptual model of biofilm formation. *Nature Reviews Microbiology* **20,** 608–620 (2022).

28. Rupel, K. *et al.* Blue laser light inhibits biofilm formation in vitro and in vivo by inducing oxidative stress. *NPJ Biofilms and Microbiomes* **5,** 29 (2019).

29. Chen, F. & Wegner, S. V. Blue-light-switchable bacterial cell–cell adhesions enable the control of multicellular bacterial communities. *ACS Synthetic Biology* **9,** 1169–1180 (2020).

30. Gómez-Ramírez, A. L. *et al.* Biofilm-forming capacity of two benthic microalgae, Navicula incerta and Navicula sp., on three substrates (Naviculales: Naviculaceae). *Revista de Biología Tropical* **67,** 599–607 (2019).

31. Sekar, R., Venugopalan, V., Satpathy, K., Nair, K. & Rao, V. *Laboratory studies on adhesion of microalgae to hard substrates,* 109–116 (Springer, 2004).

32. Cheah, Y. T. & Chan, D. J. C. Physiology of microalgal biofilm: a review on prediction of adhesion on substrates. *Bioengineered* **12,** 7577–7599 (2021).

33. Jeon, Y.-C., Cho, C.-W. & Yun, Y.-S. Measurement of microalgal photosynthetic activity depending on light intensity and quality. *Biochemical Engineering Journal* **27,** 127–131 (2005).

34. Mittag, M. Circadian rhythms in microalgae. *International Review of Cytology* **206,** 213–247 (2001).

35. Yuan, H. *et al.* Effect of light spectra on microalgal biofilm: Cell growth, photosynthetic property, and main organic composition. *Renewable Energy* **157,** 83–89 (2020).

36. Yuan, H. *et al.* Analyzing microalgal biofilm structures formed under different light conditions by evaluating cell–cell interactions. *Journal of Colloid and Interface Science* **583,** 563–570 (2021).

37. Wang, Y. *et al.* The self-adaption capability of microalgal biofilm under different light intensities: Photosynthetic parameters and biofilm microstructures. *Algal Research* **58,** 102383 (2021).

38. Nagata, Y. Light-induced adhesion of Spirogyra cells to glass. *Plant Physiology* **59,** 680–683 (1977).

39. Kreis, C. T., Grangier, A. & Bäumchen, O. In vivo adhesion force measurements of Chlamydomonas on model substrates. *Soft Matter* **15,** 3027–3035 (2019).

40. Kreis, C. T., Le Blay, M., Linne, C., Makowski, M. M. & Bäumchen, O. Adhesion of Chlamydomonas microalgae to surfaces is switchable by light. *Nature Physics* **14,** 45–49 (2018).

41. Merchant, S. S. *et al.* The Chlamydomonas genome reveals the evolution of key animal and plant functions. *Science* **318,** 245–250 (2007).

42. Greiner, A. *et al.* Targeting of photoreceptor genes in *Chlamydomonas reinhardtii* via zinc-finger nucleases and CRISPR/Cas9. *The Plant Cell* **29,** 2498–2518 (2017).

43. Ehrenberg, C. G. Die Infusionsthierchen als vollkommene Organismen. Ein Blick in das tiefere organische Leben der Natur. (1838).

44. Pröschold, T., Marin, B., Schlösser, U. G. & Melkonian, M. Molecular phylogeny and taxonomic revision of Chlamydomonas (Chlorophyta). I. Emendation of Chlamydomonas Ehrenberg and Chloromonas Gobi, and description of Oogamochlamys gen. nov. and Lobochlamys gen. nov. *Protist* **152,** 265–300 (2001).

45. Harris, E. H. *The Chlamydomonas Sourcebook: Introduction to Chlamydomonas and Its Laboratory Use: Volume 1.* (Academic Press, 2009).

46. Harris, E. H. Chlamydomonas as a model organism. *Annual Review of Plant Biology* **52,** 363–406 (2001).

47. Noordally, Z. B. & Millar, A. J. Clocks in algae. *Biochemistry* **54,** 171–183 (2015).

48. Sasso, S., Stibor, H., Mittag, M. & Grossman, A. R. The Natural History of Model Organisms: From molecular manipulation of domesticated Chlamydomonas reinhardtii to survival in nature. *eLife* **7,** e39233 (2018).

49. Witman, G. *The Chlamydomonas Sourcebook: Cell Motility and Behavior: Volume 3.* (Academic Press, 2009).

50. Witman, G. B. in *Ciliary and Flagellar Membranes* 1–30 (Springer, 1990).

51. Roberts, K., Gurney-Smith, M. & Hills, G. Structure, composition and morphogenesis of the cell wall of Chlamydomonas reinhardi: I. Ultrastructure and preliminary chemical analysis. *Journal of Ultrastructure Research* **40,** 599–613 (1972).

52. Meyer, M. T. *et al.* Rubisco small-subunit $\alpha$-helices control pyrenoid formation in Chlamydomonas. *Proceedings of the National Academy of Sciences* **109,** 19474–19479 (2012).

53. Mast, S. O. The structure and function of the eyespot in unicellular and colonial organisms. *Archiv für Protistenkunde* **60,** 197–220 (1927).

54. Gruber, H. E. & Rosario, B. Variation in eyespot ultrastructure in Chlamydomonas reinhardi (ac-31). *Journal of Cell Science* **15,** 481–494 (1974).

55. Melkonian, M. & Robenek, H. Eyespot membranes of Chlamydomonas reinhardii: a freeze-fracture study. *Journal of Ultrastructure Research* **72,** 90–102 (1980).

56. Foster, K. & Smyth, R. Light antennas in phototactic algae. *Microbiological Reviews* **44,** 572–630 (1980).

57. Gilpin, W., Bull, M. S. & Prakash, M. The multiscale physics of cilia and flagella. *Nature Reviews Physics* **2,** 74–88 (2020).

58. Bishop, D. W. Motility of the sperm flagellum. *Nature* **182,** 1638–1640 (1958).

59. Omori, T., Ito, H. & Ishikawa, T. Swimming microorganisms acquire optimal efficiency with multiple cilia. *Proceedings of the National Academy of Sciences* **117,** 30201–30207 (2020).

60. Reese, T. Olfactory cilia in the frog. *The Journal of Cell Biology* **25,** 209–230 (1965).

61. Bustamante-Marin, X. M. & Ostrowski, L. E. Cilia and mucociliary clearance. *Cold Spring Harbor Perspectives in Biology* **9,** a028241 (2017).

62. Faubel, R., Westendorf, C., Bodenschatz, E. & Eichele, G. Cilia-based flow network in the brain ventricles. *Science* **353,** 176–178 (2016).

63. Grimes, D. T. & Burdine, R. D. Left–right patterning: breaking symmetry to asymmetric morphogenesis. *Trends in Genetics* **33,** 616–628 (2017).

64. Fliegauf, M., Benzing, T. & Omran, H. When cilia go bad: cilia defects and ciliopathies. *Nature Reviews Molecular Cell Biology* **8,** 880–893 (2007).

65. Pazour, G. J. & Rosenbaum, J. L. Intraflagellar transport and cilia-dependent diseases. *Trends in Cell Biology* **12,** 551–555 (2002).

66. Brown, J. M. & Witman, G. B. Cilia and diseases. *Bioscience* **64,** 1126–1137 (2014).

67. Ringo, D. L. Flagellar motion and fine structure of the flagellar apparatus in Chlamydomonas. *The Journal of Cell Biology* **33,** 543–571 (1967).

68. Wilson, N. F., Iyer, J. K., Buchheim, J. A. & Meek, W. Regulation of flagellar length in Chlamydomonas. **19,** 494–501 (2008).

69. Bloodgood, R. A. Motility occurring in association with the surface of the Chlamydomonas flagellum. *The Journal of Cell Biology* **75,** 983–989 (1977).

70. Bloodgood, R. Flagella-dependent gliding motility in Chlamydomonas. *Protoplasma* **106,** 183–192 (1981).

71. Bloodgood, R. A. *Flagellar surface motility: gliding and microsphere movements,* 273–279 (Elsevier, 1995).

72. Gibbons, I. R. & Rowe, A. J. Dynein: a protein with adenosine triphosphatase activity from cilia. *Science* **149,** 424–426 (1965).

73. Burgess, S. A., Walker, M. L., Sakakibara, H., Knight, P. J. & Oiwa, K. Dynein structure and power stroke. *Nature* **421,** 715–718 (2003).

74. Vale, R. D., Reese, T. S. & Sheetz, M. P. Identification of a novel force-generating protein, kinesin, involved in microtubule-based motility. *Cell* **42,** 39–50 (1985).

75. Kozminski, K. G., Johnson, K. A., Forscher, P. & Rosenbaum, J. L. A motility in the eukaryotic flagellum unrelated to flagellar beating. *Proceedings of the National Academy of Sciences* **90,** 5519–5523 (1993).

76. Bloodgood, R. A. & May, G. S. Functional modification of the Chlamydomonas flagellar surface. *The Journal of Cell Biology* **93,** 88–96 (1982).

77. Bloodgood, R. A. Glycoprotein dynamics in the Chlamydomonas flagellar membrane. *Advances in Molecular and Cell Biology* **1,** 97–130 (1987).

78. Schwarz, F. & Aebi, M. Mechanisms and principles of N-linked protein glycosylation. *Current Opinion in Structural Biology* **21,** 576–582 (2011).

79. Mathieu-Rivet, E., Lerouge, P. & Bardor, M. Chlamydomonas reinhardtii: protein glycosylation and production of biopharmaceuticals. *Chlamydomonas: Biotechnology and Biomedicine,* 45–72 (2017).

80. Lucas, P.-L. *et al.* Multiple xylosyltransferases heterogeneously xylosylate protein N-linked glycans in Chlamydomonas reinhardtii. *The Plant Journal* **102,** 230–245 (2020).

81. Shih, S. M. *et al.* Intraflagellar transport drives flagellar surface motility. *eLife* **2,** e00744 (2013).

82. Xu, N. *et al.* Altered N-glycan composition impacts flagella-mediated adhesion in Chlamydomonas reinhardtii. *eLife* **9,** e58805 (2020).

83. Witman, G. B., Carlson, K., Berliner, J. & Rosenbaum, J. L. Chlamydomonas flagella: I. Isolation and electrophoretic analysis of microtubules, matrix, membranes, and mastigonemes. *The Journal of Cell Biology* **54,** 507–539 (1972).

84. Nakamura, S. *et al.* Assembly and function of Chlamydomonas flagellar mastigonemes as probed with a monoclonal antibody. *Journal of Cell Science* **109,** 57–62 (1996).

85. Bouck, G. Architecture and assembly of mastigonemes. *Advances in Cell and Molecular Biology* **2,** 237–271 (1972).

86. Amador, G. J., Wei, D., Tam, D. & Aubin-Tam, M.-E. Fibrous flagellar hairs of Chlamydomonas reinhardtii do not enhance swimming. *Biophysical Journal* **118,** 2914–2925 (2020).

87. McLean, R. J., Laurendi, C. J. & Brown Jr, R. M. The relationship of gamone to the mating reaction in Chlamydomonas moewusii. *Proceedings of the National Academy of Sciences* **71,** 2610–2613 (1974).

88. Snell, W. Mating in Chlamydomonas: a system for the study of specific cell adhesion. I. Ultrastructural and electrophoretic analyses of flagellar surface components involved in adhesion. *The Journal of Cell Biology* **68,** 48–69 (1976).

89. Adair, W. Characterization of Chlamydomonas sexual agglutinins. *Journal of Cell Science* **1985,** 233–260 (1985).

90. Goodenough, U. W., Adair, W. S., Collin-Osdoby, P. & Heuser, J. E. Structure of the Chlamydomonas agglutinin and related flagellar surface proteins in vitro and in situ. *The Journal of Cell Biology* **101,** 924–941 (1985).

91. Merchant, S. S. *et al.* Between a rock and a hard place: trace element nutrition in Chlamydomonas. *Biochimica et Biophysica Acta (BBA)-Molecular Cell Research* **1763,** 578–594 (2006).

92. Fragkopoulos, A. A. *et al.* Self-generated oxygen gradients control collective aggregation of photosynthetic microbes. *Journal of the Royal Society Interface* **18,** 20210553 (2021).

93. Mus, F., Dubini, A., Seibert, M., Posewitz, M. C. & Grossman, A. R. Anaerobic acclimation in Chlamydomonas reinhardtii: anoxic gene expression, hydrogenase induction, and metabolic pathways. *Journal of Biological Chemistry* **282,** 25475–25486 (2007).

94. Torzillo, G., Scoma, A., Faraloni, C. & Giannelli, L. Advances in the biotechnology of hydrogen production with the microalga Chlamydomonas reinhardtii. *Critical Reviews in Biotechnology* **35,** 485–496 (2015).

95. Hunnicutt, G. R., Kosfiszer, M. G. & Snell, W. J. Cell body and flagellar agglutinins in Chlamydomonas reinhardtii: the cell body plasma membrane is a reservoir for agglutinins whose migration to the flagella is regulated by a functional barrier. *The Journal of Cell Biology* **111,** 1605–1616 (1990).

96. Bernstein, E. Synchronous division in Chlamydomonas moewusii. *Science* **131,** 1528–1529 (1960).

97. Craigie, R. & Cavalier-Smith, T. Cell volume and the control of the Chlamydomonas cell cycle. *Journal of Cell Science* **54,** 173–191 (1982).

98. Donnan, L. & John, P. C. Cell cycle control by timer and sizer in Chlamydomonas. *Nature* **304,** 630–633 (1983).

99. McAteer, M., Donnan, L. & John, P. C. The timing of division in Chlamydomonas. *New Phytologist* **99,** 41–56 (1985).

100. Vítová, M. & Zachleder, V. Points of commitment to reproductive events as a tool for analysis of the cell cycle in synchronous cultures of algae. *Folia Microbiologica* **50** (2005).

101. Cross, F. R. & Umen, J. G. The Chlamydomonas cell cycle. *The Plant Journal* **82,** 370–392 (2015).

102. Umen, J. G. & Goodenough, U. W. Control of cell division by a retinoblastoma protein homolog in Chlamydomonas. *Genes & Development* **15,** 1652–1661 (2001).

103. Jones, R. F. Physiological and biochemical aspects of growth and gametogenesis in Chlamydomonas reinhardtii. *Annals of the New York Academy of Sciences* **175,** 648–659 (1970).

104. Cavalier-Smith, T. Basal body and flagellar development during the vegetative cell cycle and the sexual cycle of Chlamydomonas reinhardii. *Journal of Cell Science* **16,** 529–556 (1974).

105. Treier, U., Fuchs, S., Weber, M., Wakarchuk, W. W. & Beck, C. F. Gametic differentiation in Chlamydomonas reinhardtii: light dependence and gene expression patterns. *Archives of Microbiology* **152,** 572–577 (1989).

106. Friedmann, I., Colwin, A. & Colwin, L. H. Fine-structural aspects of fertilization in Chlamydomonas reinhardi. *Journal of Cell Science* **3,** 115–128 (1968).

107. Suzuki, L. & Johnson, C. Photoperiodic control of germination in the unicell Chlamydomonas. *Naturwissenschaften* **89,** 214–220 (2002).

108. Colegrave, N. Sex releases the speed limit on evolution. *Nature* **420,** 664–666 (2002).

109. Bloodgood, R. A. & Workman, L. J. A flagellar surface glycoprotein mediating cell-substrate interaction in Chlamydomonas. *Cell Motility* **4,** 77–87 (1984).

110. Kozminski, K. G. in *Methods in Cell Biology* 263–271 (Elsevier, 1995).

111. Cole, D. G. *et al.* Chlamydomonas kinesin-II–dependent intraflagellar transport (IFT): IFT particles contain proteins required for ciliary assembly in Caenorhabditis elegans sensory neurons. *The Journal of Cell Biology* **141,** 993–1008 (1998).

112. Pazour, G. J., Wilkerson, C. G. & Witman, G. B. A dynein light chain is essential for the retrograde particle movement of intraflagellar transport (IFT). *The Journal of Cell Biology* **141,** 979–992 (1998).

113. Piperno, G. & Mead, K. Transport of a novel complex in the cytoplasmic matrix of Chlamydomonas flagella. *Proceedings of the National Academy of Sciences* **94,** 4457–4462 (1997).

114. Cole, D. G. The intraflagellar transport machinery of Chlamydomonas reinhardtii. *Traffic* **4,** 435–442 (2003).

115. Jordan, M. A. & Pigino, G. The structural basis of intraflagellar transport at a glance. *Journal of Cell Science* **134,** jcs247163 (2021).

116. Pazour, G. J. & Witman, G. B. *The Chlamydomonas Sourcebook: The Chlamydomonas flagellum as a model for human ciliary disease: Volume 3.* 445–478 (Academic Press, 2009).

117. Stepanek, L. & Pigino, G. Microtubule doublets are double-track railways for intraflagellar transport trains. *Science* **352,** 721–724 (2016).

118. Lechtreck, K. F. in *Methods in Enzymology* 265–284 (Elsevier, 2013).

119. Herzik Jr, M. A. Cryo-electron microscopy reaches atomic resolution. *Nature* **587,** 39–40 (2020).

120. Van den Hoek, H. *et al.* In situ architecture of the ciliary base reveals the stepwise assembly of intraflagellar transport trains. *Science* **377,** 543–548 (2022).

121. Silverman, M. & Simon, M. Flagellar rotation and the mechanism of bacterial motility. *Nature* **249,** 73–74 (1974).

122. Sleigh, M. A. Flagellar beat patterns and their possible evolution. *BioSystems* **14,** 423–431 (1981).

123. Hoops, H. J. & Witman, G. B. Outer doublet heterogeneity reveals structural polarity related to beat direction in Chlamydomonas flagella. *The Journal of Cell Biology* **97,** 902–908 (1983).

124. Ishibashi, K., Sakakibara, H. & Oiwa, K. Force-Generating Mechanism of Axonemal Dynein in Solo and Ensemble. *International Journal of Molecular Sciences* **21,** 2843 (2020).

125. Purcell, E. M. Life at low Reynolds number. *American Journal of Physics* **45,** 3–11 (1977).

126. Rüffer, U. & Nultsch, W. High-speed cinematographic analysis of the movement of Chlamydomonas. *Cell Motility* **5,** 251–263 (1985).

127. Cortese, D. & Wan, K. Y. Control of helical navigation by three-dimensional flagellar beating. *Physical Review Letters* **126,** 088003 (2021).

128. Polin, M., Tuval, I., Drescher, K., Gollub, J. P. & Goldstein, R. E. Chlamydomonas swims with two "gears" in a eukaryotic version of run-and-tumble locomotion. *Science* **325,** 487–490 (2009).

129. Berg, H. C. *E. Coli in Motion.* (Springer, 2004).

130. Bloodgood, R. A. Gliding motility and flagellar glycoprotein dynamics in Chlamydomonas. *Ciliary and Flagellar Membranes,* 91–128 (1990).

131. Bloodgood, R. A., Tetreault, J. & Sloboda, R. D. The Chlamydomonas flagellar membrane glycoprotein FMG-1B is necessary for expression of force at the flagellar surface. *Journal of Cell Science* **132,** jcs233429 (2019).

132. Gennerich, A., Carter, A. P., Reck-Peterson, S. L. & Vale, R. D. Force-induced bidirectional stepping of cytoplasmic dynein. *Cell* **131,** 952–965 (2007).

133. Bloodgood, R. A. & Salomonsky, N. L. Calcium influx regulates antibody-induced glycoprotein movements within the Chlamydomonas flagellar membrane. *Journal of Cell Science* **96,** 27–33 (1990).

134. Collingridge, P., Brownlee, C. & Wheeler, G. L. Compartmentalized calcium signaling in cilia regulates intraflagellar transport. *Current Biology* **23,** 2311–2318 (2013).

135. Fort, C., Collingridge, P., Brownlee, C. & Wheeler, G. Ca2+ elevations disrupt interactions between intraflagellar transport and the flagella membrane in Chlamydomonas. *Journal of Cell Science* **134,** jcs253492 (2021).

136. Schmidt, J. A. & Eckert, R. Calcium couples flagellar reversal to photostimulation in Chlamydomonas reinhardtii. *Nature* **262,** 713–715 (1976).

137. Erickson, E., Wakao, S. & Niyogi, K. K. Light stress and photoprotection in Chlamydomonas reinhardtii. *The Plant Journal* **82,** 449–465 (2015).

138. Jékely, G. Evolution of phototaxis. *Philosophical Transactions of the Royal Society B: Biological Sciences* **364,** 2795–2808 (2009).

139. Hegemann, P. & Bruck, B. Light-induced stop response in Chlamydomonas reinhardtii: Occurrence and adaptation phenomena. *Cell Motility and the Cytoskeleton* **14,** 501–515 (1989).

140. Ermilova, E. V., Zalutskaya, Z. M. & Gromov, B. V. Chemotaxis towards sugars in Chlamydomonas reinhardtii. *Current Microbiology* **27,** 47–50 (1993).

141. Sjoblad, R. & Frederikse, P. H. Chemotactic responses of Chlamydomonas reinhardtii. *Molecular and Cellular Biology* **1,** 1057–1060 (1981).

142. Nelson, G. *et al.* Cells collectively migrate during ammonium chemotaxis in Chlamydomonas reinhardtii. *Scientific Reports* **13,** 10781 (2023).

143. Ermilova, E. V., Zalutskaya, Z. M. & Lapina, T. V. Chemotaxis of Chlamydomonas reinhardtii to nitrate is changed during gametogenesis. *Protistology* **6,** 79–84 (2009).

144. Ermilova, E. & Zalutskaya, Z. Regulation by light of chemotaxis to nitrite during the sexual life cycle in Chlamydomonas reinhardtii. *Plants* **3,** 113–127 (2014).

145. Ermilova, E. V., Zalutskaya, Z. M., Lapina, T. V. & Nikitin, M. M. Chemotactic behavior of Chlamydomonas reinhardtii is altered during gametogenesis. *Current Microbiology* **46,** 0261–0264 (2003).

146. Choi, H. I., Kim, J. Y. H., Kwak, H. S., Sung, Y. J. & Sim, S. J. Quantitative analysis of the chemotaxis of a green alga, Chlamydomonas reinhardtii, to bicarbonate using diffusion-based microfluidic device. *Biomicrofluidics* **10,** 014121 (2016).

147. Byrne, T. E., Wells, M. R. & Johnson, C. H. Circadian rhythms of chemotaxis to ammonium and of methylammonium uptake in Chlamydomonas. *Plant Physiology* **98,** 879–886 (1992).

148. Roberts, A. Mechanisms of gravitaxis in Chlamydomonas. *The Biological Bulletin* **210,** 78–80 (2006).

149. Bean, B. Geotactic behavior of Chlamydomonas. *The Journal of Protozoology* **24,** 394–401 (1977).

150. Kam, V., Moseyko, N., Nemson, J. & Feldman, L. J. Gravitaxis in Chlamydomonas reinhardtii: characterization using video microscopy and computer analysis. *International Journal of Plant Sciences* **160,** 1093–1098 (1999).

151. Kage, A., Omori, T., Kikuchi, K. & Ishikawa, T. The shape effect of flagella is more important than bottom-heaviness on passive gravitactic orientation in Chlamydomonas reinhardtii. *Journal of Experimental Biology* **223,** jeb205989 (2020).

152. Goldstein, R. E. Batchelor prize lecture fluid dynamics at the scale of the cell. *Journal of Fluid Mechanics* **807,** 1–39 (2016).

153. Brumley, D. R., Wan, K. Y., Polin, M. & Goldstein, R. E. Flagellar synchronization through direct hydrodynamic interactions. *eLife* **3,** e02750 (2014).

154. Williams, C. R. & Bees, M. A. A tale of three taxes: photo-gyro-gravitactic bioconvection. *Journal of Experimental Biology* **214,** 2398–2408 (2011).

155. Panda, S., Hogenesch, J. B. & Kay, S. A. *Molecular Clocks and Light Signalling: Novartis Foundation Symposium 253,* 73–88 (Wiley Online Library, 2003).

156. Björn, L. O. *Photobiology: The science of light and life* (Springer, 2015).

157. Sánchez-Baracaldo, P., Raven, J. A., Pisani, D. & Knoll, A. H. Early photosynthetic eukaryotes inhabited low-salinity habitats. *Proceedings of the National Academy of Sciences* **114,** E7737–E7745 (2017).

158. Rockwell, N. C. *et al.* Eukaryotic algal phytochromes span the visible spectrum. *Proceedings of the National Academy of Sciences* **111,** 3871–3876 (2014).

159. Boll, F. On the anatomy and physiology of the retina. *Vision Research* **17,** 1249–1265 (1977).

160. Kühne, W. Chemical processes in the retina. *Vision Research* **17,** 1269–1316 (1977).

161. Famintzin, A. Die Wirkung der Lichtes auf die Bewegung der Chlamidomonas pulvisculus Ehr., Euglena viridis Ehr. und Orcillatoria insignis Tw. *Mélanges Biologiques tirés du Bulletin de l'Académie Imperial des Sciences de St-Petersbourg* **6,** 73–93 (1866).

162. Engelmann, T. W. Ueber Licht-und Farbenperception niederster Organismen. *Archiv für die gesamte Physiologie des Menschen und der Tiere* **29,** 387–400 (1882).

163. Davenport, C. B. & Cannon, W. B. On the determination of the direction and rate of movement of organisms by light. *The Journal of Physiology* **21,** 22 (1897).

164. Wald, G. & Brown, P. K. The synthesis of rhodopsin from retinene1. *Proceedings of the National Academy of Sciences* **36,** 84–92 (1950).

165. Wald, G. & Hubbard, R. The synthesis of rhodopsin from vitamin A1. *Proceedings of the National Academy of Sciences* **36,** 92–102 (1950).

166. Hubbard, R. & Wald, G. The mechanism of rhodopsin synthesis. *Proceedings of the National Academy of Sciences* **37,** 69–79 (1951).

167. Hubbard, R. & Wald, G. Cis-trans isomers of vitamin A and retinene in vision. *Science* **115,** 60–63 (1952).

168. Bownds, D. Site of attachment of retinal in rhodopsin. *Nature* **216,** 1178–1181 (1967).

169. Walne, P. L. & Arnott, H. J. The comparative ultrastructure and possible function of eyespots: Euglena granulata and Chlamydomonas eugametos. *Planta* **77,** 325–353 (1967).

170. Hegemann, P. & Berthold, P. in *The Chlamydomonas Sourcebook* 395–429 (Elsevier, 2009).

171. Hegemann, P. & Nagel, G. From channelrhodopsins to optogenetics. *EMBO Molecular Medicine* **5,** 173–176 (2013).

172. Kateriya, S., Nagel, G., Bamberg, E. & Hegemann, P. "Vision" in single-celled algae. *Physiology* **19,** 133–137 (2004).

173. Foster, K. W. *et al.* A rhodopsin is the functional photoreceptor for phototaxis in the unicellular eukaryote Chlamydomonas. *Nature* **311,** 756–759 (1984).

174. Hegemann, P., Gärtner, W. & Uhl, R. All-trans retinal constitutes the functional chromophore in Chlamydomonas rhodopsin. *Biophysical Journal* **60,** 1477–1489 (1991).

175. Hegemann, P., Fuhrmann, M. & Kateriya, S. Algal sensory photoreceptors. *Journal of Phycology* **37,** 668–676 (2001).

176. Harz, H. & Hegemann, P. Rhodopsin-regulated calcium currents in Chlamydomonas. *Nature* **351,** 489–491 (1991).

177. Ehlenbeck, S., Gradmann, D., Braun, F.-J. & Hegemann, P. Evidence for a light-induced H+ conductance in the eye of the green alga Chlamydomonas reinhardtii. *Biophysical Journal* **82,** 740–751 (2002).

178. Nonnengässer, C., Holland, E.-M., Harz, H. & Hegemann, P. The nature of rhodopsin-triggered photocurrents in Chlamydomonas. II. Influence of monovalent ions. *Biophysical Journal* **70,** 932–938 (1996).

179. Holland, E. M., Harz, H., Uhl, R. & Hegemann, P. Control of phobic behavioral responses by rhodopsin-induced photocurrents in Chlamydomonas. *Biophysical Journal* **73,** 1395–1401 (1997).

180. Hegemann, P. Vision in microalgae. *Planta* **203,** 265–274 (1997).

181. Oesterhelt, D. & Stoeckenius, W. Rhodopsin-like protein from the purple membrane of Halobacterium halobium. *Nature New Biology* **233,** 149–152 (1971).

182. Oesterhelt, D. & Stoeckenius, W. Functions of a new photoreceptor membrane. *Proceedings of the National Academy of Sciences* **70,** 2853–2857 (1973).

183. Lanyi, J. K. Halorhodopsin—A second retinal pigment in Halobacterium halobium. *Trends in Biochemical Sciences* **6,** 60–62 (1981).

184. Deininger, W., Kröger, P., Hegemann, U., Lottspeich, F. & Hegemann, P. Chlamyrhodopsin represents a new type of sensory photoreceptor. *The EMBO Journal* **14,** 5849–5858 (1995).

185. Fuhrmann, M., Stahlberg, A., Govorunova, E., Rank, S. & Hegemann, P. The abundant retinal protein of the Chlamydomonas eye is not the photoreceptor for phototaxis and photophobic responses. *Journal of Cell Science* **114,** 3857–3863 (2001).

186. Fuhrmann, M., Deininger, W., Kateriya, S. & Hegemann, P. *Photoreceptors and Light Signalling: Rhodopsin-related proteins, cop1, cop2 and chop1, in Chlamydomonas reinhardtii,* 125–133 (Royal Society of Chemistry Cambridge, 2003).

187. Tian, Y., Gao, S., von der Heyde, E. L., Hallmann, A. & Nagel, G. Two-component cyclase opsins of green algae are ATP-dependent and light-inhibited guanylyl cyclases. *BMC Biology* **16,** 1–18 (2018).

188. Sineshchekov, O. A., Jung, K.-H. & Spudich, J. L. Two rhodopsins mediate phototaxis to low-and high-intensity light in Chlamydomonas reinhardtii. *Proceedings of the National Academy of Sciences* **99,** 8689–8694 (2002).

189. Suzuki, T. *et al.* Archaeal-type rhodopsins in Chlamydomonas: model structure and intracellular localization. *Biochemical and Biophysical Research Communications* **301,** 711–717 (2003).

190. Sineshchekov, O., Govorunova, E., Der, A., Keszthelyi, L. & Nultsch, W. Photoelectric responses in phototactic flagellated algae measured in cell suspension. *Journal of Photochemistry and Photobiology B: Biology* **13,** 119–134 (1992).

191. Jiang, F. & Doudna, J. A. CRISPR–Cas9 structures and mechanisms. *Annual Review of Biophysics* **46,** 505–529 (2017).

192. Nagel, G. *et al.* Channelrhodopsin-1: a light-gated proton channel in green algae. *Science* **296,** 2395–2398 (2002).

193. Nagel, G. *et al.* Channelrhodopsin-2, a directly light-gated cation-selective membrane channel. *Proceedings of the National Academy of Sciences* **100,** 13940–13945 (2003).

194. Berthold, P. *et al.* Channelrhodopsin-1 initiates phototaxis and photophobic responses in Chlamydomonas by immediate light-induced depolarization. *The Plant Cell* **20,** 1665–1677 (2008).

195. Awasthi, M., Ranjan, P., Sharma, K., Veetil, S. K. & Kateriya, S. The trafficking of bacterial type rhodopsins into the Chlamydomonas eyespot and flagella is IFT mediated. *Scientific Reports* **6,** 1–16 (2016).

196. Baidukova, O. *et al.* Gating and ion selectivity of Channelrhodopsins are critical for photo-activated orientation of Chlamydomonas as shown by in vivo point mutation. *Nature Communications* **13,** 7253 (2022).

197. Deisseroth, K. Optogenetics: 10 years of microbial opsins in neuroscience. *Nature Neuroscience* **18,** 1213–1225 (2015).

198. Deisseroth, K. Optogenetics. *Nature Methods* **8,** 26–29 (2011).

199. Mukherjee, S., Hegemann, P. & Broser, M. Enzymerhodopsins: novel photoregulated catalysts for optogenetics. *Current Opinion in Structural Biology* **57,** 118–126 (2019).

200. Dutta, R., Qin, L. & Inouye, M. Histidine kinases: diversity of domain organization. *Molecular Microbiology* **34,** 633–640 (1999).

201. West, A. H. & Stock, A. M. Histidine kinases and response regulator proteins in two-component signaling systems. *Trends in Biochemical Sciences* **26,** 369–376 (2001).

202. Potter, L. R. Guanylyl cyclase structure, function and regulation. *Cellular Signalling* **23,** 1921–1926 (2011).

203. Beavo, J. A. & Brunton, L. L. Cyclic nucleotide research—still expanding after half a century. *Nature Reviews Molecular Cell Biology* **3,** 710–717 (2002).

204. Goodenough, U. W. Cyclic AMP enhances the sexual agglutinability of Chlamydomonas flagella. *The Journal of Cell Biology* **109,** 247–252 (1989).

205. Boonyareth, M., Saranak, J., Pinthong, D., Sanvarinda, Y. & Foster, K. W. Roles of cyclic AMP in regulation of phototaxis in Chlamydomonas reinhardtii. *Biologia* **64,** 1058–1065 (2009).

206. Luck, M. *et al.* A photochromic histidine kinase rhodopsin (HKR1) that is bimodally switched by ultraviolet and blue light. *Journal of Biological Chemistry* **287,** 40083–40090 (2012).

207. Penzkofer, A., Luck, M., Mathes, T. & Hegemann, P. Bistable Retinal Schiff Base Photodynamics of Histidine Kinase Rhodopsin HKR 1 from Chlamydomonas reinhardtii. *Photochemistry and Photobiology* **90,** 773–785 (2014).

208. Luck, M. & Hegemann, P. The two parallel photocycles of the Chlamydomonas sensory photoreceptor histidine kinase rhodopsin 1. *Journal of Plant Physiology* **217,** 77–84 (2017).

209. Darwin, C. & Darwin, F. *The Power of Movement in Plants* (John Murray, 1880).

210. Sachs, J. *Vorlesungen über Pflanzen-physiologie* (W. Engelmann, 1882).

211. Jagger, J. Photoreactivation. *Bacteriological Reviews* **22,** 99–142 (1958).

212. Gressel, J. Blue light photoreception. *Photochemistry and Photobiology* **30,** 749–754 (1979).

213. Ahmad, M. & Cashmore, A. R. HY4 gene of A. thaliana encodes a protein with characteristics of a blue-light photoreceptor. *Nature* **366,** 162–166 (1993).

214. Sancar, A. Structure and function of DNA photolyase and cryptochrome blue-light photoreceptors. *Chemical Reviews* **103,** 2203–2238 (2003).

215. Kelner, A. Photoreactivation of ultraviolet-irradiated Escherichia coli, with special reference to the dose-reduction principle and to ultraviolet-induced mutation. *Journal of Bacteriology* **58,** 511–522 (1949).

216. Sancar, A. & Sancar, G. B. Escherichia coli DNA photolyase is a flavoprotein. *Journal of Molecular Biology* **172,** 223–227 (1984).

217. Johnson, J. L. *et al.* Identification of the second chromophore of Escherichia coli and yeast DNA photolyases as 5, 10-methenyltetrahydrofolate. *Proceedings of the National Academy of Sciences* **85,** 2046–2050 (1988).

218. Eker, A., Dekker, R. & Berends, W. Photoreactivating enzyme from Streptomyces griseus—IV. On the nature of the chromophoric cofactor in Streptomyces griseus photoreactivating enzyme. *Photochemistry and Photobiology* **33,** 65–72 (1981).

219. Chaves, I. *et al.* The cryptochromes: blue light photoreceptors in plants and animals. *Annual Review of Plant Biology* **62,** 335–364 (2011).

220. Franz, S. *et al.* Structure of the bifunctional cryptochrome aCRY from Chlamydomonas reinhardtii. *Nucleic Acids Research* **46,** 8010–8022 (2018).

221. Rredhi, A. *et al.* DASH cryptochrome 1, a UV-A receptor, balances the photosynthetic machinery of Chlamydomonas reinhardtii. *New Phytologist* **232,** 610–624 (2021).

222. Miyamoto, Y. & Sancar, A. Vitamin B2-based blue-light photoreceptors in the retinohypothalamic tract as the photoactive pigments for setting the circadian clock in mammals. *Proceedings of the National Academy of Sciences* **95,** 6097–6102 (1998).

223. Rodgers, C. T. & Hore, P. J. Chemical magnetoreception in birds: the radical pair mechanism. *Proceedings of the National Academy of Sciences* **106,** 353–360 (2009).

224. Xu, J. *et al.* Magnetic sensitivity of cryptochrome 4 from a migratory songbird. *Nature* **594,** 535–540 (2021).

225. Oldemeyer, S., Haddad, A. Z. & Fleming, G. R. Interconnection of the antenna pigment 8-HDF and flavin facilitates red-light reception in a bifunctional animal-like cryptochrome. *Biochemistry* **59,** 594–604 (2019).

226. Beel, B. *et al.* A flavin binding cryptochrome photoreceptor responds to both blue and red light in Chlamydomonas reinhardtii. *The Plant Cell* **24,** 2992–3008 (2012).

227. Small, G. D., Min, B. & Lefebvre, P. A. Characterization of a Chlamydomonas reinhardtii gene encoding a protein of the DNA photolyase/blue light photoreceptor family. *Plant Molecular Biology* **28,** 443–454 (1995).

228. Müller, N. *et al.* A plant cryptochrome controls key features of the Chlamydomonas circadian clock and its life cycle. *Plant Physiology* **174,** 185–201 (2017).

229. Reisdorph, N. A. & Small, G. D. The CPH1 gene of Chlamydomonas reinhardtii encodes two forms of cryptochrome whose levels are controlled by light-induced proteolysis. *Plant Physiology* **134,** 1546–1554 (2004).

230. Immeln, D., Schlesinger, R., Heberle, J. & Kottke, T. Blue light induces radical formation and autophosphorylation in the light-sensitive domain of Chlamydomonas cryptochrome. *Journal of Biological Chemistry* **282,** 21720–21728 (2007).

231. Bruce, V. G. The biological clock in Chlamydomonas reinhardi. *The Journal of Protozoology* **17,** 328–334 (1970).

232. Kondo, T., Johnson, C. H. & Hastings, J. W. Action spectrum for resetting the circadian phototaxis rhythm in the CW15 strain of Chlamydomonas: I. Cells in darkness. *Plant Physiology* **95,** 197–205 (1991).

233. Johnson, C. H., Kondo, T. & Hastings, J. W. Action spectrum for resetting the circadian phototaxis rhythm in the CW15 strain of Chlamydomonas: II. Illuminated cells. *Plant Physiology* **97,** 1122–1129 (1991).

234. Kottke, T., Oldemeyer, S., Wenzel, S., Zou, Y. & Mittag, M. Cryptochrome photoreceptors in green algae: unexpected versatility of mechanisms and functions. *Journal of Plant Physiology* **217,** 4–14 (2017).

235. Zou, Y. *et al.* An animal-like cryptochrome controls the Chlamydomonas sexual cycle. *Plant Physiology* **174,** 1334–1347 (2017).

236. Petersen, J. *et al.* The world of algae reveals a broad variety of cryptochrome properties and functions. *Frontiers in Plant Science* **12,** 766509 (2021).

237. Spexard, M., Thöing, C., Beel, B., Mittag, M. & Kottke, T. Response of the sensory animal-like cryptochrome aCRY to blue and red light as revealed by infrared difference spectroscopy. *Biochemistry* **53,** 1041–1050 (2014).

238. Franz-Badur, S. *et al.* Structural changes within the bifunctional cryptochrome photolyase CraCRY upon blue light excitation. *Scientific Reports* **9,** 9896 (2019).

239. Brudler, R. *et al.* Identification of a new cryptochrome class: structure, function, and evolution. *Molecular Cell* **11,** 59–67 (2003).

240. Liscum, E. & Briggs, W. R. Mutations in the NPH1 locus of Arabidopsis disrupt the perception of phototropic stimuli. *The Plant Cell* **7,** 473–485 (1995).

241. Christie, J. M. *et al.* Arabidopsis NPH1: a flavoprotein with the properties of a photoreceptor for phototropism. *Science* **282,** 1698–1701 (1998).

242. Christie, J. M., Salomon, M., Nozue, K., Wada, M. & Briggs, W. R. LOV (light, oxygen, or voltage) domains of the blue-light photoreceptor phototropin (nph1): binding sites for the chromophore flavin mononucleotide. *Proceedings of the National Academy of Sciences* **96,** 8779–8783 (1999).

243. Christie, J. M. Phototropin blue-light receptors. *Annual Review of Plant Biology* **58,** 21–45 (2007).

244. Christie, J. M., Swartz, T. E., Bogomolni, R. A. & Briggs, W. R. Phototropin LOV domains exhibit distinct roles in regulating photoreceptor function. *The Plant Journal* **32,** 205–219 (2002).

245. Huala, E. *et al.* Arabidopsis NPH1: a protein kinase with a putative redox-sensing domain. *Science* **278,** 2120–2123 (1997).

246. Kasahara, M. *et al.* Photochemical properties of the flavin mononucleotide-binding domains of the phototropins from Arabidopsis, rice, and Chlamydomonas reinhardtii. *Plant Physiology* **129,** 762–773 (2002).

247. Salomon, M., Christie, J. M., Knieb, E., Lempert, U. & Briggs, W. R. Photochemical and mutational analysis of the FMN-binding domains of the plant blue light receptor, phototropin. *Biochemistry* **39,** 9401–9410 (2000).

248. Swartz, T. E. *et al.* The photocycle of a flavin-binding domain of the blue light photoreceptor phototropin. *Journal of Biological Chemistry* **276,** 36493–36500 (2001).

249. Crosson, S. & Moffat, K. Structure of a flavin-binding plant photoreceptor domain: insights into light-mediated signal transduction. *Proceedings of the National Academy of Sciences* **98,** 2995–3000 (2001).

250. Fedorov, R. *et al.* Crystal structures and molecular mechanism of a light-induced signaling switch: the Phot-LOV1 domain from Chlamydomonas reinhardtii. *Biophysical Journal* **84,** 2474–2482 (2003).

251. Matsuoka, D. & Tokutomi, S. Blue light-regulated molecular switch of Ser/Thr kinase in phototropin. *Proceedings of the National Academy of Sciences* **102,** 13337–13342 (2005).

252. Pfeifer, A., Mathes, T., Lu, Y., Hegemann, P. & Kottke, T. Blue light induces global and localized conformational changes in the kinase domain of full-length phototropin. *Biochemistry* **49,** 1024–1032 (2010).

253. Onodera, A. *et al.* Phototropin from Chlamydomonas reinhardtii is functional in Arabidopsis thaliana. *Plant and Cell Physiology* **46,** 367–374 (2005).

254. Huang, K., Merkle, T. & Beck, C. F. Isolation and characterization of a Chlamydomonas gene that encodes a putative blue-light photoreceptor of the phototropin family. *Physiologia Plantarum* **115,** 613–622 (2002).

255. Im, C.-S., Eberhard, S., Huang, K., Beck, C. F. & Grossman, A. R. Phototropin involvement in the expression of genes encoding chlorophyll and carotenoid biosynthesis enzymes and LHC apoproteins in Chlamydomonas reinhardtii. *The Plant Journal* **48,** 1–16 (2006).

256. Petroutsos, D. *et al.* A blue-light photoreceptor mediates the feedback regulation of photosynthesis. *Nature* **537,** 563–566 (2016).

257. Tokutsu, R., Fujimura-Kamada, K., Yamasaki, T., Matsuo, T. & Minagawa, J. Isolation of photoprotective signal transduction mutants by systematic bioluminescence screening in Chlamydomonas reinhardtii. *Scientific Reports* **9,** 2820 (2019).

258. Huang, K. & Beck, C. F. Phototropin is the blue-light receptor that controls multiple steps in the sexual life cycle of the green alga Chlamydomonas reinhardtii. *Proceedings of the National Academy of Sciences* **100,** 6269–6274 (2003).

259. Huang, K., Kunkel, T. & Beck, C. F. Localization of the blue-light receptor phototropin to the flagella of the green alga Chlamydomonas reinhardtii. *Molecular Biology of the Cell* **15,** 3605–3614 (2004).

260. Pan, J.-M., Haring, M. A. & Beck, C. F. Characterization of blue light signal transduction chains that control development and maintenance of sexual competence in Chlamydomonas reinhardtii. *Plant Physiology* **115,** 1241–1249 (1997).

261. Ermilova, E. V., Zalutskaya, Z. M., Huang, K. & Beck, C. F. Phototropin plays a crucial role in controlling changes in chemotaxis during the initial phase of the sexual life cycle in Chlamydomonas. *Planta* **219,** 420–427 (2004).

262. Trippens, J. *et al.* Phototropin influence on eyespot development and regulation of phototactic behavior in Chlamydomonas reinhardtii. *The Plant Cell* **24,** 4687–4702 (2012).

263. Magdaong, N. C. M. & Blankenship, R. E. Photoprotective, excited-state quenching mechanisms in diverse photosynthetic organisms. *Journal of Biological Chemistry* **293,** 5018–5025 (2018).

264. Rizzini, L. *et al.* Perception of UV-B by the Arabidopsis UVR8 protein. *Science* **332,** 103–106 (2011).

265. Tilbrook, K. *et al.* UV-B perception and acclimation in Chlamydomonas reinhardtii. *The Plant Cell* **28,** 966–983 (2016).

266. Fernández, M. B., Tossi, V., Lamattina, L. & Cassia, R. A comprehensive phylogeny reveals functional conservation of the UV-B photoreceptor UVR8 from green algae to higher plants. *Frontiers in Plant Science* **7,** 1698 (2016).

267. Christie, J. M. *et al.* Plant UVR8 photoreceptor senses UV-B by tryptophan-mediated disruption of cross-dimer salt bridges. *Science* **335,** 1492–1496 (2012).

268. Wu, D. *et al.* Structural basis of ultraviolet-B perception by UVR8. *Nature* **484,** 214–219 (2012).

269. Allorent, G. *et al.* UV-B photoreceptor-mediated protection of the photosynthetic machinery in Chlamydomonas reinhardtii. *Proceedings of the National Academy of Sciences* **113,** 14864–14869 (2016).

270. Lambert, G., Bergman, A., Zhang, Q., Bortz, D. & Austin, R. Physics of biofilms: the initial stages of biofilm formation and dynamics. *New Journal of Physics* **16,** 045005 (2014).

271. Mazza, M. G. The physics of biofilms—an introduction. *Journal of Physics D: Applied Physics* **49,** 203001 (2016).

272. Arnaouteli, S., Bamford, N. C., Stanley-Wall, N. R. & Kovács, Á. T. Bacillus subtilis biofilm formation and social interactions. *Nature Reviews Microbiology* **19,** 600–614 (2021).

273. Gordon, J. W., Scangos, G. A., Plotkin, D. J., Barbosa, J. A. & Ruddle, F. H. Genetic transformation of mouse embryos by microinjection of purified DNA. *Proceedings of the National Academy of Sciences* **77,** 7380–7384 (1980).

274. Shalom, S., Lieberman, K., Lewis, A. & Cohen, S. R. A micropipette force probe suitable for near-field scanning optical microscopy. *Review of Scientific Instruments* **63,** 4061–4065 (1992).

275. Backholm, M., Ryu, W. S. & Dalnoki-Veress, K. Viscoelastic properties of the nematode Caenorhabditis elegans, a self-similar, shear-thinning worm. *Proceedings of the National Academy of Sciences* **110,** 4528–4533 (2013).

276. Böddeker, T. J., Karpitschka, S., Kreis, C. T., Magdelaine, Q. & Bäumchen, O. Dynamic force measurements on swimming Chlamydomonas cells using micropipette force sensors. *Journal of the Royal Society Interface* **17,** 20190580 (2020).

277. Backholm, M. & Bäumchen, O. Micropipette force sensors for in vivo force measurements on single cells and multicellular microorganisms. *Nature Protocols* **14,** 594–615 (2019).

278. Kreis, C. T. *Microalgal Adhesion to Model Substrates: A Quantitative in vivo Study on the Biological Mechanisms and Surface Forces.* PhD thesis (Georg-August-Universität Göttingen, 2017).

279. Batchelor, G. K. *An introduction to fluid dynamics* (Cambridge University Press, 2000).

280. Cho, M. & Martinez, W. L. *Statistics in MATLAB: A primer* (CRC Press, 2014).

281. Nelson, P. C., Bromberg, S., Hermundstad, A. & Prentice, J. *Physical models of living systems* (WH Freeman New York, 2015).

282. Raj M, K. & Chakraborty, S. PDMS microfluidics: A mini review. *Journal of Applied Polymer Science* **137,** 48958 (2020).

283. Daniel, B. & Dufresne, E. *Matlab particle-tracking algorithm* `https://site.physics.georgetown.edu/matlab/index.html`.

284. Catalan, R. E. *et al.* Light-regulated adsorption and desorption of Chlamydomonas cells at surfaces. *Soft Matter* **19,** 306–314 (2023).

285. Langmuir, I. The adsorption of gases on plane surfaces of glass, mica and platinum. *Journal of the American Chemical Society* **40,** 1361–1403 (1918).

286. Liu, Y. & Shen, L. From Langmuir kinetics to first-and second-order rate equations for adsorption. *Langmuir* **24,** 11625–11630 (2008).

287. Till, S., Ebmeier, F., Fragkopoulos, A. A., Mazza, M. G. & Bäumchen, O. Motility and self-organization of gliding Chlamydomonas populations. *Physical Review Research* **4,** L042046 (2022).

288. Witman, G. B. Chlamydomonas phototaxis. *Trends in Cell Biology* **3,** 403–408 (1993).

289. Mast, S. The Relative Stimulating Efficiency of Spectral Colors for the Lower Organisms. *Proceedings of the National Academy of Sciences* **1,** 622–625 (1915).

290. Mittag, M., Kiaulehn, S. & Johnson, C. H. The circadian clock in Chlamydomonas reinhardtii. What is it for? What is it similar to? *Plant Physiology* **137,** 399–409 (2005).

291. Baier, T., Jacobebbinghaus, N., Einhaus, A., Lauersen, K. J. & Kruse, O. Introns mediate post-transcriptional enhancement of nuclear gene expression in the green microalga Chlamydomonas reinhardtii. *PLoS Genetics* **16,** e1008944 (2020).

292. Sancar, A. Cryptochrome: the second photoactive pigment in the eye and its role in circadian photoreception. *Annual Review of Biochemistry* **69,** 31–67 (2000).

293. Iomini, C., Li, L., Mo, W., Dutcher, S. K. & Piperno, G. Two flagellar genes, AGG2 and AGG3, mediate orientation to light in Chlamydomonas. *Current Biology* **16,** 1147–1153 (2006).

# Acknowledgements

I would like to express sincere gratitude to everyone who supported and guided me throughout this time. First, I thank my supervisor, Prof. Dr. Oliver Bäumchen, for giving me the opportunity to pursue my doctoral studies in his research group and for his full support and guidance throughout this tough but beautiful journey. I am really grateful for all I have learnt these four years and I will cherish all the little lessons that will be of use in the future.

I would also love to thank the members of my Thesis Advisory Committee: Prof. Dr. Jörg Enderlein and Prof. Dr. Marcus Müller. I truly appreciate your feedback during our meetings and the valuable constructive criticism that helped me to stay on track.

I extend my gratitude to my collaborators: Prof. Dr. Peter Hegemann for all the exciting and stimulating discussions about chlamys and photoreceptors. It was really crucial to have such a renowned experienced mind on board of this project. Many thanks also to members of his lab: Olga, Simon, Darius, and Heide, for their support in discussions and for providing all the mutant chlamys that I could study during my research. I would also like to express my regards to Dr. Maike Lorenz for her support to my project, kindness and tremendous knowledge about the algal microcosmos.

The work of secretaries and technical assistants must not go unmentioned. Therefore, many thanks to Monika and Guido for their administrative work; Kris Hantke and Thomas Eggers for their valuable help with the setups and outstanding IT service.

I would also like to thank the people who put their hearts to provide an excellent environment for doctoral students: Antje Erdmann and Frauke Bergmann from the PBCS Office. I am really grateful for their outstanding support through these years and for encouraging me to join the organization team of the Third Infinity Conference 2022.

My work could have not been advanced and completed without the unconditional support of my colleagues/friends Alex and Antoine. Alex, I can't thank you enough for all your support and guidance, I truly value your experience and emotional intelligence. You deserve all the baklava of the world! Antoine, I extend my eternal gratitude for all your help, support, and profound kindness (and car rides back

home!). I'll miss that combined display of complain-about-everything and laugh-about-everything. I was really lucky to have both of you guys around.

Kind regards to past members of the Bäumchen Lab: Nicolas, Marzieh, Theresa, Linne, the two Sebastians, Nicole; as well as to the current members of EP-V in Bayreuth: Tom, Florian, Reinhardt, Klaus, Wolfgang, Andreas, and Christine. I extend my regards to the nice people I met over the past 4 years: Hansol (friend/snack-provider), Olinka, Sayedeh, Aina, Venecia, Raul, and Antaran.

Now, I cross the Atlantic and fly over the Andes to thank all the people in Chile who supported me and helped me to be here at this very moment. My former advisor Prof. Dr. Ulrich Volkmann and Dr. Tomás Corrales for all the effort and support offered to me in my application for the scholarship. This should not go unmentioned. A big thank to my older colleagues in the lab: Coti Retamal, Diego Díaz, and Nicolás Moraga.

Y mil gracias a mis amigos en Chile (Carlos, Joaquin, Roberto y Rodrigo); Nico en Alemania; y Cote y Danjel en los Países Bajos. Mi familia 1: Mis padres, Juan y Teresa; mi hermana, Natalia; mis sobrinas, Javi e Isi; y mi Familia 2, Andrea, Gastón y Caco. Los amo y extraño mucho! También no puedo dejar de agradecer a los que ya no están, pero que siempre merodean en mis recuerdos: mi Oma, mi abuela Ondina, el Nano, la Lela y el tata 'Willy'.

Finally, I thank Cote, whom I love with all my heart, for being my strongest emotional support throughout this journey.